Relationship between the electronic structure and the functional properties of new quantum materials

Relation entre la structure électronique et les propriétés fonctionnelles des nouveaux matériaux quantiques

Thèse de doctorat de l'université Paris-Saclay et de l'université du Pays Basque

École doctorale n°564: physique en Île-de-France (PIF)
Spécialité de doctorat: Physique
Graduate School : Physique. Référent : Faculté des sciences d'Orsay

Thèse préparée à l'**Institut des Sciences Moléculaires d'Orsay** (Université Paris-Saclay, CNRS), sous la direction de **Andrés Felipe SANTANDER-SYRO**, professeur à l'Université Paris-Saclay, la codirection de **José Enrique ORTEGA**, professeur à l'Université du Pays Basque, et le coencadrement de **Eugene KRASOVSKII**, professeur à l'Université du Pays Basque

Thèse soutenue à Paris-Saclay, le 18 Octobre 2024, par

Amitayush JHA THAKUR

Composition du jury

Membres du jury avec voix délibérative

Fabrice BERT Professeur, Université Paris-Saclay	Président
Yannick FAGOT-REVURAT Professeur, Université de Lorraine	Rapporteur & Examinateur
Jorge LOBO-CHECA Chercheur CSIC, Université de Zaragoza	Rapporteur & Examinateur
Vyacheslav Silkin Professeur, Université du Pays Basque	Examinateur
Marie d'Angelo MCF, HDR, Sorbonne Université	Examinatrice
Eugene KRASOVSKII Professeur, Université du Pays Basque	Co-encadrer de thèse
José Enrique ORTEGA Professeur, Université du Pays Basque	Codirecteur de thèse
Andrés F. SANTANDER-SYRO Professeur, Université Paris-Saclay	Codirecteur de thèse

THESE DE DOCTORAT

NNT :

université
PARIS-SACLAY

ÉCOLE DOCTORALE
Physique en
Île-de-France (PIF)

Titre : Relation entre la structure électronique et les propriétés fonctionnelles des nouveaux matériaux quantiques

Mots clés : Spectroscopie de Photoémission Résolue en Angle, Transition métal-isolant, Matériaux 2D, Structure électronique, Physique de la matière condensée

Résumé : Cette thèse explore des matériaux novateurs dont les propriétés sont intrinsèquement liées à leur structure électronique. Nous nous concentrons sur l'étude expérimentale de trois matériaux. Premièrement, le CuRhO$_2$ dopé au Mg, qui présente une valeur élevée du coefficient thermoélectrique en raison de sa structure électronique unique. Deuxièmement, des films minces du métal corrélé CaVO$_3$, qui subissent une transition métal-isolant (MIT) en dessous d'une épaisseur critique. Enfin, une hétérostructure de dihalogénure de métal de transition magnétique 2D, FeCl$_2$, déposée sur une surface Au(111), avec des états électroniques uniques près du niveau de Fermi.

Le CuRhO$_2$ est un matériau isolant avec une valeur élevée du coefficient de thermopouvoir. Le dopage en trous du matériau avec du Mg le rend conducteur tout en conservant un thermopouvoir relativement élevé. L'origine de ce thermopouvoir élevé a été théoriquement attribuée à la structure de bande en « moule à pudding » du matériau. Grâce à l'ARPES, nous avons vérifié expérimentalement que les bandes observées dans le CuRhO$_2$ dopé à 10% de Mg correspondent aux bandes calculées par DFT et sont de type « moule à pudding ». Nous avons ensuite calculé le coefficient de Seebeck à partir des bandes DFT du matériau dopé (S $\sim$ 260 $\mu V/K$), qui s'avère en accord avec les valeurs expérimentales.

Les films minces de CaVO$_3$ ont été observés comme subissant une MIT en fonction de l'épaisseur du film. Des films minces de CaVO$_3$ avec des épaisseurs de 90 u.c., 45 u.c., 30 u.c., 20 u.c. et 15 u.c. sur un substrat de SrTiO$_3$ ont été mesurés par ARPES, et les changements dans la structure électronique ont été suivis. Les changements observés dans la surface de Fermi indiquent une augmentation de la contrainte de traction sur le film à mesure que l'épaisseur diminue. Une réduction de la largeur de bande de conduction et une augmentation des états V^{3+} dans les films plus minces ont été observées, indiquant la localisation des électrons près du niveau de Fermi. Une MIT a été observée lors de la transition d'un film métallique de 20 u.c. à un film isolant de 15 u.c., avec la disparition de la bande de conduction et l'apparition d'une bande plate isolante à $\sim$ -0,9 eV. Nous concluons que la contrainte épitaxiale accrue, et non la dimensionnalité, est à l'origine de la MIT, en accord avec les études précédentes.

Le dihalogénure de métal de transition magnétique 2D FeCl$_2$ sur Au(111) est observé comme hébergeant des états nouveaux au niveau de Fermi. Une monocouche (ML) de FeCl$_2$ déposée sur une surface Au(111) a été caractérisée par STM. La ML de FeCl$_2$ présente une modulation pseudo-périodique sur sa surface, avec une périodicité moyenne de $\sim$ 2,3 nm, ce qui donne lieu à des points lumineux et sombres dans la densité locale d'états (LDOS) observés à un biais d'échantillon de 1,5 eV. La LDOS a été mesurée à ces sites par spectroscopie tunnel à balayage (STS) et s'est révélée différente aux emplacements lumineux et sombres. Le STS aux points lumineux a révélé la présence de plusieurs états près du niveau de Fermi. Des mesures d'interférence quasi-particulaire (QPI) ont révélé la présence de deux bandes dispersantes avec une masse effective m^* similaire à celle des états de surface (SS) d'Au(111). Les deux bandes sont observées comme étant séparées par $\Delta k \sim 0,36nm^{-1}$ et $\Delta E \sim 0,3eV$. L'origine de ces bandes est hypothétiquement attribuée soit à un dédoublement Zeeman des bandes Rashba de l'Au(111) en raison de la proximité magnétique avec FeCl$_2$, soit à des états quantifiés dans le puits à l'interface FeCl$_2$-Au(111).

Title : The relationship between the electronic structure and the functional properties of novel quantum materials

Keywords : Angle resolved Photoemission spectroscopy, Metal-insulator transition, 2-D materials, Electronic structure, Condensed matter physics

Abstract : This thesis explores novel materials whose properties are inherently tied to their electronic structure. We focus on the experimental study of three materials. First, Mg-doped $\mathrm{CuRhO_2}$, which displays a high value of the thermoelectric coefficient owing to its unique electronic structure. Second, thin films of the correlated metal $\mathrm{CaVO_3}$, which undergo a metal-to-insulator transition (MIT) below a critical film thickness. Lastly, a heterostructure of 2D magnetic transition metal dihalide $\mathrm{FeCl_2}$ on top of an Au(111) surface, with unique electronic states near the Fermi level.

$\mathrm{CuRhO_2}$ is an insulating material with a high value of the thermopower coefficient. Hole doping the material with Mg makes it conductive while still retaining a relatively high thermopower. The origin of the high thermopower has been theoretically proposed as originating from the "pudding-mold" band structure of the material. Through ARPES, we experimentally verify that the observed bands in the 10% Mg-doped $\mathrm{CuRhO_2}$ match the DFT-calculated bands and are of the "pudding-mold" type. We then calculate the Seebeck coefficient from the DFT bands of the doped material (S $\sim$ 260 $\mu V/K$), which is found to be in agreement with the experimental values.

Thin films of $\mathrm{CaVO_3}$ are observed to undergo an MIT as a function of film thickness. Thin films of $\mathrm{CaVO_3}$ with thicknesses of 90 u.c., 45 u.c., 30 u.c., 20 u.c., and 15 u.c. on an $\mathrm{SrTiO_3}$ substrate were measured by ARPES, and changes in the electronic structure were tracked. The observed changes in the Fermi surface point towards increased tensile strain on the film as the thickness is decreased. A decrease in conduction band bandwidth and an increase in $\mathrm{V^{3+}}$ states in thinner films were observed, indicating the localization of electrons near the Fermi level. An MIT was observed when transitioning from a metallic 20 u.c. film to an insulating 15 u.c. film, with the disappearance of the conduction band and the appearance of an insulating flat band at $\sim$ -0.9 eV. We conclude that the increased epitaxial strain, rather than dimensionality, is the driver of the MIT, in agreement with previous studies.

A 2D magnetic transition metal halide $\mathrm{FeCl_2}$ on Au(111) is observed to host novel states at the Fermi level. A monolayer (ML) of $\mathrm{FeCl_2}$ deposited on an Au(111) surface was characterized by STM. The $\mathrm{FeCl_2}$ ML hosts pseudo-periodic modulation on its surface, with an average periodicity of $\sim$ 2.3 nm, which gives rise to bright and dark spots in the local density of states (LDOS) observed at 1.5 eV sample bias. The LDOS was measured at these sites through scanning tunneling spectroscopy (STS) and was found to differ at the bright and dark locations. STS at bright spots revealed the presence of multiple states near the Fermi level. Quasi-particle interference (QPI) measurements revealed the presence of two dispersing bands with effective mass m^* similar to Au(111) surface states (SS). The two bands are observed to be split by $\Delta k \sim 0.36 nm^{-1}$ and $\Delta E \sim 0.3 eV$. The origin of these bands is hypothesized to be either Zeeman splitting of Rashba bands of Au(111) due to magnetic proximity with $\mathrm{FeCl_2}$ or from quantized well states at the $\mathrm{FeCl_2}$-Au(111) interface.

Acknowledgments

This work would not have been possible without the efforts of a village's worth of people. First, I would like to thank my thesis advisor, Andres, for guiding me, giving me the opportunity to fall in love with physics all over again, and for your amazing cakes.

A big thanks also to the entire SCES team at Université Paris-Saclay : Emmanouil, Franck, Pedro, Emma, and Max (Thees), for all the late-night shifts and fun discussions over coffee. Especially Max, for putting up with my incessant questions and guiding me through the initial stages of my PhD.

The journey has had its fair share of bumps, especially during my stay at UPV, given Enrique's serious health problems. My heartfelt thanks to Max (Ilyn) for working with me and guiding me through the latter half of my time in San Sebastián. Thanks to the team at CFM, including Samuel, Sebastian, Celia, Ilya, and Andrea, for all the amazing work we did together. I also want to thank Enrique and Eugene for their valuable input during the final stages of my thesis.

And finally, to my wonderful friends : Ajay, Kush, Alexei, Paula, Minh, and Danielle, for the fun times and beautiful moments we shared. My parents for always being there for support. Last but not least, Ashwin, thank you for the late-night discussions about life, the universe, and everything, for the shared laughs and tears, and for just being there.

Contents

1 Introduction 1

2 Theoretical background 3
  2.1 Bands in a solid 3
  2.2 Electron Correlations through the Hubbard Model 6
  2.3 Rashba Spin-Orbit Coupling in Solids 8
  2.4 Density Functional Theory 10
    2.4.1 DFT+U 13

3 Experimental Techniques 17
  3.1 Angle resolved photoemission spectroscopy 17
    3.1.1 Photoelectric effect 17
    3.1.2 The 3-step model of photoemission 18
    3.1.3 Experimental considerations 24
    3.1.4 Analyses of ARPES data 27
  3.2 Scanning Tunneling Microscopy 27
    3.2.1 Experimental considerations 29
    3.2.2 Operating modes 30
    3.2.3 Scanning tunneling spectroscopy (STS) 30
    3.2.4 Quasi Particle Interference 31
  3.3 QPI vs ARPES as electronic structure probes 32

4 Thermoelectricity in CuRhO$_2$ doped with Mg 35
  4.1 Introduction 35
  4.2 The pudding mold band 36
  4.3 Enhanced thermoelectricity from correlations 37
  4.4 Measurements and Observations 39
  4.5 Conclusion and future outlook 44
  4.6 Appendix 44
    4.6.1 DFT calculations 44
    4.6.2 Thermopower calculation with BoltzTrap 44

5 Metal-Insulator Transition in CaVO$_3$ 47
  5.1 Introduction 47
  5.2 Crystal structure 48
  5.3 Electronic structure 48
    5.3.1 DFT calculations 48
  5.4 ARPES measurements 50
    5.4.1 90 u.c. 50

5.4.2 45 u.c. 51
5.4.3 30 u.c. 51
5.4.4 20 u.c. 52
5.4.5 Bandwidth changes across metallic samples 52
5.4.6 15 u.c. 53
5.4.7 Core level XPS 53
5.5 Discussion 54
5.6 Conclusions and future outlook 55
5.7 Appendix 55
5.7.1 Band unfolding 55
5.7.2 XPS background subtraction 56

6 Quantum states of 2-D metal dihalide $FeCl_2$ on Au(111) 65
6.1 Introduction 65
6.2 Crystal structure 66
6.3 Monolayer growth 67
6.4 Bulk band spectra 69
6.5 STS measurements 71
6.6 Surface state dispersion 71
6.7 Discussion 75
6.8 Conclusion and Future outlook 79
6.9 Appendix 81
6.9.1 Magnetism in two dimensional transition metal dihalides 81
6.9.2 DFT calculations 82

Bibliography 83

List of Tables 97

List of figures 99

7 Summary 111
7.1 Introduction 111
7.2 Theoretical and experimental background 111
7.3 Thermoelectricity in Mg doped $CuRhO_2$ 112
7.4 Metal-Insulator Transition in thin films of $CaVO_3$ 114
7.5 Quantum states of 2-D metal dihalide $FeCl_2$ on Au(111) 115

8 Synthèse en Français 119
8.1 Introduction 119
8.2 Contexte théorique et expérimental 119
8.3 Thermoélectricité dans $CuRhO_2$ dopé au Mg 120
8.4 Transition métal-isolant dans les films minces de $CaVO_3$ 121
8.5 États quantiques du dihalogénure métallique 2D $FeCl_2$ sur Au(111) 122

9 Resumen en español **127**
9.1 Introducción 127
9.2 Fundamentos teóricos y experimentales 127
9.3 Termoelectricidad en $CuRhO_2$ dopado con Mg 128
9.4 Transición metal-aislante en películas delgadas de $CaVO_3$ 130
9.5 Estados cuánticos del dihaluro metálico 2D $FeCl_2$ en Au(111) 131

1 - Introduction

Understanding the relationship between the atomic structure, functional properties, and electronic structure of materials is a fundamental challenge in condensed matter physics. Many of the most intriguing phenomena in materials science, such as superconductivity, magnetism, and thermoelectric effects, arise from subtle interactions between these three domains. Despite significant progress, the intricate ways in which atomic arrangements and electronic correlations give rise to unique functional behaviors remain open questions.

This thesis is driven by the need to deepen our understanding of how the atomic and electronic structures of materials govern their physical properties. Mg-doped metallic thermoelectric $\mathrm{CuRhO_2}$, thin films of the correlated metal $\mathrm{CaVO_3}$, and the magnetic 2D van der Waals insulator $\mathrm{FeCl_2}$ on Au(111) have been selected as case studies for their rich electronic behavior and potential applications in thermoelectrics, quantum devices, and spintronics. Each of these materials exhibits complex interactions between their atomic configurations and electronic structures, providing ideal platforms to explore how subtle modifications—such as doping, dimensionality reduction, or external stimuli—can drastically alter their functional properties.

We start with an introduction to the basic concepts of bands in a solid in Chapter 2, an integral part of understanding the electronic structure of our materials. We also provide an overview of the foundations of density functional theory (DFT), a tool that we use throughout this work to calculate the electronic structure of our materials and compare with experimental data.

In Chapter 3, we provide an overview of the basics of angle-resolved photoemission spectroscopy (ARPES) and scanning tunneling microscopy/ spectroscopy (STM/STS), our main experimental tools to probe the electronic structure of materials. ARPES allows us to map the energy and momentum of electrons in a solid, providing direct insight into the band structure and the effects of electron correlations, while STM/STS provides atomically resolved images and spectroscopic data to probe the local density of states at the surface. These experimental techniques are crucial for studying the materials presented in this thesis, enabling us to bridge the gap between theoretical predictions and experimental observations.

In Chapter 4, we dive into the thermoelectric properties of Mg-doped $\mathrm{CuRhO_2}$. This material has garnered attention due to its high Seebeck coefficient and potential for thermoelectric applications. Using ARPES, we experimentally verify the existence of a "pudding-mold" band, a unique feature in the band structure that leads to enhanced thermopower. We compare these experimental results with DFT calculations to understand the underlying mechanisms driving the high thermoelectric performance of this material.

Chapter 5 explores the metal-insulator transition (MIT) in thin films of $\mathrm{CaVO_3}$, a strongly correlated metal. By systematically reducing the thickness of the $\mathrm{CaVO_3}$ films, we observe a transition from a metallic to an insulating state, driven not by quantum confinement, but by epitaxial strain from the substrate. Through ARPES measurements, we track changes in the Fermi surface, band structure, and electron correlation effects as the film thickness varies.

Finally, in Chapter 6, we investigate the electronic and magnetic properties of $\mathrm{FeCl_2}$, a 2D van der Waals magnetic insulator, when deposited on an Au(111) surface. This heterostructure presents a novel platform for studying spintronics and quantum materials due to the interplay between the magnetic order in $\mathrm{FeCl_2}$ and the metallic states of Au(111). Using STM/STS, we reveal the emergence of dispersing states near the Fermi level on the supposedly insulating $\mathrm{FeCl_2}$ monolayer, which we study in detail using quasi-particle interference (QPI).

2 - Theoretical background

This chapter gives an introductory exposition on the theoretical concepts repeatedly used throughout this work.

2.1 . Bands in a solid

Isolated atoms and molecules, by definition, have a set of localized electronic states. The electrons in these sets are immobile (having no place to move to), and in momentum space, i.e., the Fourier transform (FT) of position space, the energy bands appear flat (FT of a delta function is a constant).

Now, as we move towards a larger collection of atoms and molecules, the electrons obtain the freedom to move around more freely and become delocalized, giving rise to more non-trivial profiles in momentum space, forming bands that are conventionally represented by the occupied energy states $E(k)$ as a function of electron momentum k.

The tight-binding model in one dimension provides us with a good framework for understanding the simplest bands. Consider the linear configuration of N atoms with one electron per site. The atoms are spaced apart by the lattice constant a. The energy of occupation of a site by an electron is given by ϵ_0 and the energy t for an electron to hop from one site to the nearest neighbor atom. Then the Hamiltonian associated with this system in second quantization formalism can be written as

$$\hat{\mathcal{H}} = -\sum_i \epsilon_0 \hat{c}_i^\dagger \hat{c}_i - \sum_i t\left(\hat{c}_i^\dagger c_{i+1} + \hat{c}_{i+1}^\dagger c_i\right) \tag{2.1}$$

where $\hat{c}_i^\dagger$ and $\hat{c}_i$ are electron creation and annihilation operators at site i. These operators can be written in momentum space as

$$\hat{c}_i = \frac{1}{\sqrt{N}}\sum_{\mathbf{k}} e^{i\mathbf{k}\cdot\mathbf{r}_i}\hat{c}_{\mathbf{k}}, \quad \hat{c}_i^\dagger = \frac{1}{\sqrt{N}}\sum_{\mathbf{k}} e^{-i\mathbf{k}\cdot\mathbf{r}_i}\hat{c}_{\mathbf{k}}^\dagger \tag{2.2}$$

where $\mathbf{k} = \frac{2\pi n}{L}$ and $L = Na$ is the length of the system. Replacing 2.2 in 2.1 we get

$$\begin{aligned} \hat{\mathcal{H}} &= -\sum_{\mathbf{k}} \hat{c}_{\mathbf{k}}^\dagger \frac{1}{N}\left(N\epsilon_0 + Nt(e^{i\mathbf{k}\cdot r_i} + e^{-i\mathbf{k}\cdot r_i})\right)\hat{c}_{\mathbf{k}} \\ &= -\sum_{\mathbf{k}} (\epsilon_0 + 2t\cos(ka))\hat{c}_{\mathbf{k}}^\dagger \hat{c}_{\mathbf{k}} \end{aligned} \tag{2.3}$$

where we used $\sum_i \hat{c}_i^\dagger \hat{c}_i = N$ as the total number of electrons and $r_i = na$ where n is an integer.

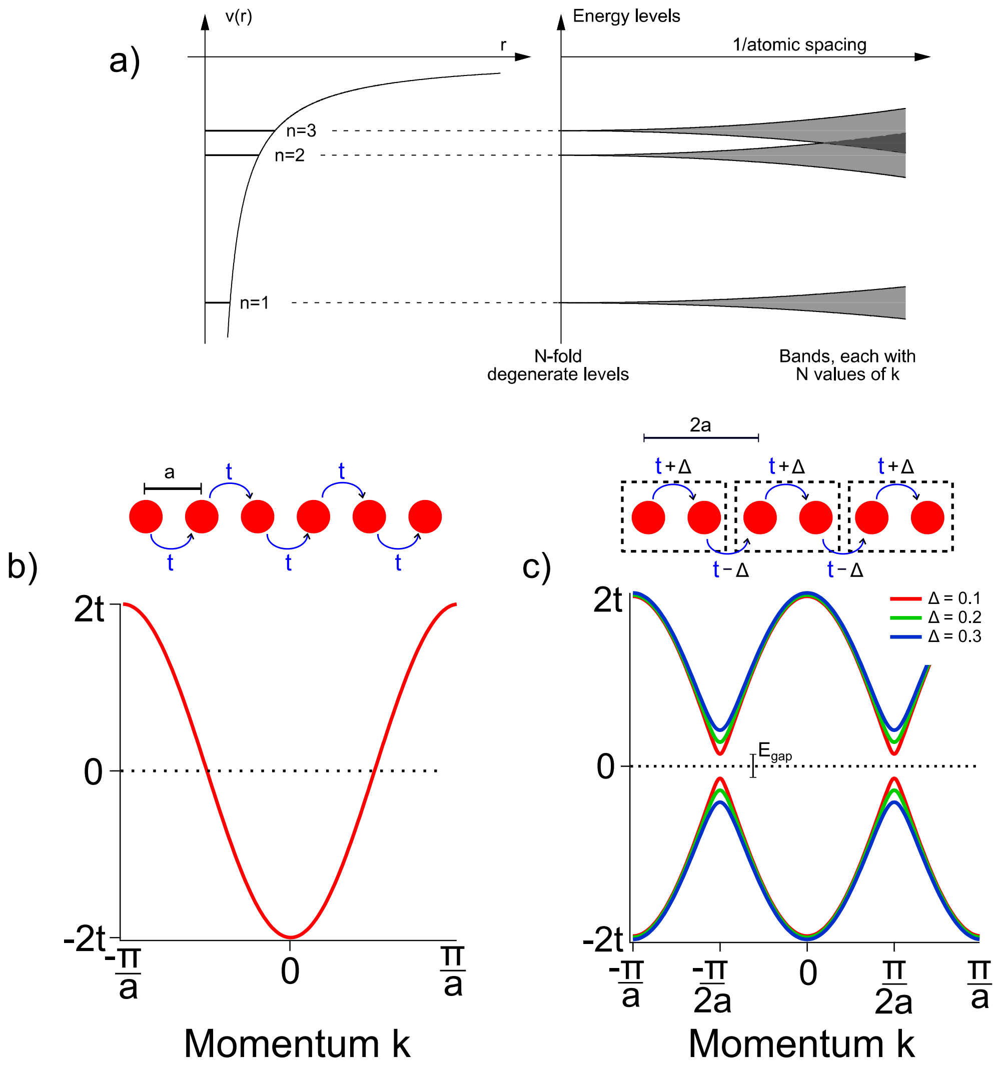

Figure 2.1 – a) Schematic of band formation going from an isolated atom to a solid. Left : electronic energy levels for an isolated atom, while right shows formations of bands with broad energy states as atoms come close together. Adapted from [7]. b) Band structure of a 1-D atomic chain in the tight-binding model. c) Band structure of a 1-D atomic chain modified by a staggered potential.

Therefore, the energy-momentum dispersion relation, or the band diagram for this 1-D chain as shown in fig. 2.1 b, is given by

$$E(\mathbf{k}) = -\epsilon_0 - 2t\cos(ka). \tag{2.4}$$

Now, in the real world, a crystal can have a complicated structure with multiple orbitals and electrons per site hopping to different sites with differing energy weights, resulting in a very different-looking band, but the essential information obtained is the same, i.e., how electrons are moving around in a crystal.

Electrons in solids can no longer be described by the free electron dispersion $E(k) = k^2/2m_e$. However, when electron-electron interactions are not strong, electrons can still be described as particle-like excitations, but now with an effective mass (m^*) which is modified based on the interactions of the electron within the solid, such as with electronic nuclei, lattice vibrations (phonons), and other electrons. As a simplification, we use the idea of a quasiparticle, which behaves like a "renormalized" or "dressed" electron that accounts for these interactions.

One important point is that the highest energy occupied by an electron in this system is ϵ_0, and this is known as the Fermi energy. As this energy lies in the middle of the energy band, there are continuous empty states slightly above this energy that the electron can occupy and hop around different sites if excited by the thermal energy $k_B T$, where k_B is the Boltzmann constant, and T is the temperature. Therefore, it's an example of a metallic system. If there were no empty states present above the Fermi energy, i.e., an energy gap, this hopping would be prohibited, and the system would be insulating.

One way we can see how a system may become insulating is by introducing a site-dependent staggered potential $V_{i,i+1} = \Delta(-1)^i$ in our original Hamiltonian, eq. 2.1. This potential introduces a differential tunneling between sites i and $i+1$ depending on the site index i (see fig. 2.1 c). Note that due to this differential tunneling, translational symmetry by a is broken and a new unit cell with $2a$ spacing is established, as now only sites i and $i+2$ are equivalent.

The new Hamiltonian can be written as

$$\hat{\mathcal{H}} = -\sum_i \epsilon_0 \hat{c}_i^\dagger \hat{c}_i - \sum_i t \left(\hat{c}_i^\dagger c_{i+1} + \hat{c}_{i+1}^\dagger c_i\right) - \Delta \sum_{i,i+1} (-1)^i \left(\hat{c}_i^\dagger c_{i+1} + \hat{c}_{i+1}^\dagger c_i\right) \tag{2.5}$$

Setting $\epsilon_0 = 0$, and referring to creation operators at odd and even sites as $A^\dagger$ and $B^\dagger$, respectively, we can rewrite $\hat{\mathcal{H}}$ as

$$\hat{\mathcal{H}} = -t(1-\Delta)\sum_i \left(A_i^\dagger B + B_i^\dagger A_i\right) - t(1+\Delta)\sum_i \left(A_{i+1}^\dagger B_i + B_i^\dagger A_{i+1}\right) \tag{2.6}$$

Using eq. 2.2 to transform to the k-space basis and using the new unit cell spacing $2a$ and total unit cells $N/2$, $\hat{\mathcal{H}}$ can be written as

$$\hat{\mathcal{H}} = \sum_k \left(A_k^\dagger B_k^\dagger\right) \begin{pmatrix} 0 & -t' - \tilde{t}e^{i2ka} \\ -t' - \tilde{t}e^{-i2ka} & 0 \end{pmatrix} \begin{pmatrix} A_k \\ B_k \end{pmatrix} \tag{2.7}$$

where $t' = t(1-\Delta)$ and $\tilde{t} = t(1+\Delta)$.

This is then diagonalized to get the two-band dispersion relation

$$E_k = \pm\sqrt{(-2t\cos k)^2 + \Delta^2}. \tag{2.8}$$

The value of Δ dictates the value of the gap thus formed between the two bands (fig. 2.1 c). Thus, we see how a modulation of the tunneling strength t by a periodic potential V can result in the formation of a band gap and transition to an insulating state. These periodic modulations can be implicit in the structure of the lattice or can be caused by external parameters, such as those observed in the emergence of charge density waves (CDW) [43] and Pierls transitions [72].

2.2 . Electron Correlations through the Hubbard Model

Our simplified tight-binding Hamiltonian doesn't include any electron-electron interactions, which we will now consider by the inclusion of the simplest interaction term, U, which is the energy cost on an atom if occupied by two electrons instead of one. We will now also consider the spin state, σ, of an electron, and an atomic site can only be occupied by electrons of opposite spin (Pauli's exclusion principle [120]).

The Hubbard Hamiltonian can thus be written as

$$\hat{\mathcal{H}} = -t\sum_{\langle i,i'\rangle\sigma}\left(\hat{c}^{\dagger}_{i\sigma}\hat{c}_{i'\sigma} + \hat{c}^{\dagger}_{i'\sigma}\hat{c}_{i\sigma}\right) - \epsilon\sum_{i}\left(\hat{n}_{i\uparrow} + \hat{n}_{i\downarrow}\right) + U\sum_{i}\hat{n}_{i\uparrow}\hat{n}_{i\downarrow} \tag{2.9}$$

where $\sigma =\uparrow,\downarrow$ are the spin states of the electron, $\hat{n}_{i\sigma} = \hat{c}^{\dagger}_{i\sigma}\hat{c}_{i\sigma}$ is the electron number operator at site i with spin σ, and $\langle i, i'\rangle$ represents nearest neighbor sites between which hopping is allowed. U is the energy cost of an atomic site being occupied by two electrons.

As simple as this equation looks, it still cannot be solved exactly. However, considering the limit of $t = 0$ and setting $\epsilon = 0$, the Hamiltonian becomes

$$\hat{\mathcal{H}} = U\sum_{i}\hat{n}_{i\uparrow}\hat{n}_{i\downarrow}. \tag{2.10}$$

At half-filling, i.e., a total of one electron per atomic site, the ground state is $E = 0$, where each atomic site is occupied by one electron. The lowest excited states in the system, that is, one site with two electrons, have the energy U. Therefore, our system has an insulating gap of energy U, which is caused by electron-electron interactions instead of the band structure. Such a system is called a "Mott Insulator" [108].

We can also use mean-field theory (MFT) to study magnetism arising from the Hubbard model. Using the mean-field approximation, $\hat{n}_{\mathbf{i}\sigma}$ can be expressed as its average plus the deviation from the average value,

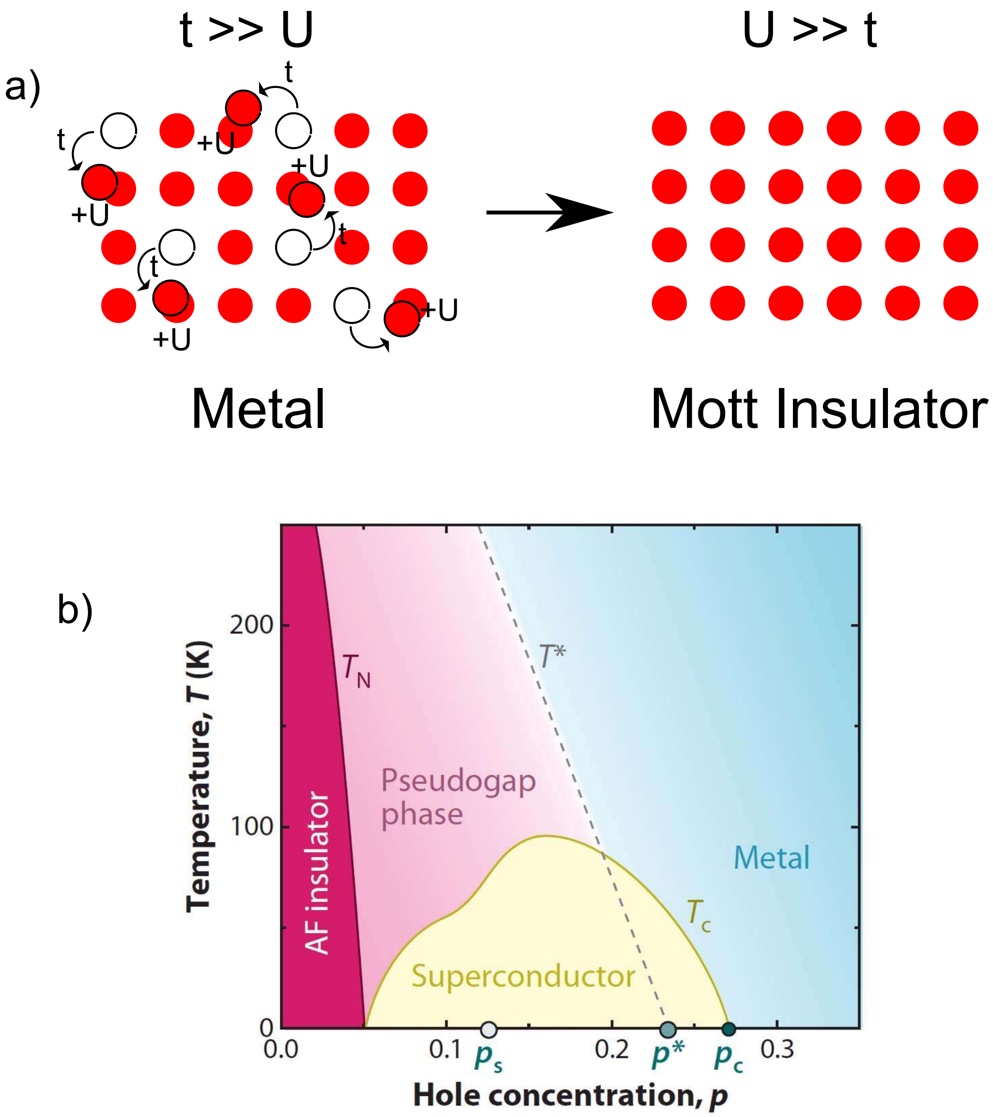
a)
t >> U
U >> t
t
+U
Metal
Mott Insulator
b)
Temperature, T (K)
200
100
0
0.0
0.1
0.2
0.3
T_N
T^*
AF insulator
Pseudogap phase
Metal
Superconductor
T_c
p_s
p^*
p_c
Hole concentration, p

Figure 2.2 – a) Cartoon representation of a half-filled Hubbard model. Left depicts the case of weak Hubbard interaction term U compared to hopping t, and right depicts the case of strong correlations. Electrons are indicated by the red balls. b) Schematic phase diagram of a cuprate superconductor as a function of hole doping p and temperature T. From [124].

$$\begin{aligned} n_{i\uparrow} &= \langle n_{i\uparrow} \rangle + (n_{i\uparrow} - \langle n_{i\uparrow} \rangle) \\ n_{i\downarrow} &= \langle n_{i\downarrow} \rangle + (n_{i\downarrow} - \langle n_{i\downarrow} \rangle) \, . \end{aligned} \tag{2.11}$$

Using this, we can write

$$\begin{aligned} n_{\mathbf{i}\uparrow} n_{\mathbf{i}\downarrow} &= \left[\langle n_{\mathbf{i}\uparrow}\rangle + (n_{\mathbf{i}\uparrow} - \langle n_{\mathbf{i}\uparrow}\rangle)\right]\left[\langle n_{\mathbf{i}\downarrow}\rangle + (n_{\mathbf{i}\downarrow} - \langle n_{\mathbf{i}\downarrow}\rangle)\right] \\ &\approx \langle n_{\mathbf{i}\uparrow}\rangle \langle n_{\mathbf{i}\downarrow}\rangle + \langle n_{\mathbf{i}\downarrow}\rangle (n_{\mathbf{i}\uparrow} - \langle n_{\mathbf{i}\uparrow}\rangle) + \langle n_{\mathbf{i}\uparrow}\rangle (n_{\mathbf{i}\downarrow} - \langle n_{\mathbf{i}\downarrow}\rangle) \\ &= n_{\mathbf{i}\uparrow} \langle n_{\mathbf{i}\downarrow}\rangle + n_{\mathbf{i}\downarrow} \langle n_{\mathbf{i}\uparrow}\rangle - \langle n_{\mathbf{i}\uparrow}\rangle \langle n_{\mathbf{i}\downarrow}\rangle . \end{aligned} \tag{2.12}$$

The Hubbard interaction term within the MFT can be written as

$$U \sum_{\mathbf{i}} \left(\hat{n}_{\mathbf{i}\uparrow} \langle \hat{n}_{\mathbf{i}\downarrow}\rangle + \hat{n}_{\mathbf{i}\downarrow} \langle \hat{n}_{\mathbf{i}\uparrow}\rangle - \langle \hat{n}_{\mathbf{i}\uparrow}\rangle \langle \hat{n}_{\mathbf{i}\downarrow}\rangle\right). \tag{2.13}$$

Consider an antiferromagnetic pattern with mean fermionic occupation : $\langle n_{\mathbf{i}\sigma}\rangle$

$$\begin{aligned} \langle \hat{n}_{\mathbf{i}\uparrow}\rangle &= \rho + (-1)^{\mathbf{i}} m \\ \langle \hat{n}_{\mathbf{i}\downarrow}\rangle &= \rho - (-1)^{\mathbf{i}} m \end{aligned} \tag{2.14}$$

where ρ is a constant between 0 and 1 and m is the order parameter that defines the strength of the antiferromagnetic field. The interaction term now becomes

$$U \sum_{\mathbf{i}} \Big((\rho - (-1)^{\mathbf{i}} m)\hat{n}_{\mathbf{i}\uparrow} + (\rho - (-1)^{\mathbf{i}} m)\hat{n}_{\mathbf{i}\downarrow} - \langle \hat{n}_{\mathbf{i}\uparrow}\rangle \langle \hat{n}_{\mathbf{i}\downarrow}\rangle\Big). \tag{2.15}$$

which can be reduced back to our case of the staggered potential (eq. 2.5), thus opening a band gap. The staggered potential in our case is referred to as the "spin density wave" (SDW), and this kind of antiferromagnetic insulator is called a "Slater Insulator". Note that MFT is only valid for small values of U. If the correlations are strong, MFT cannot be used as the average occupancy of a spin state cannot be meaningfully defined.

Strong correlations are usually encountered in systems with poorly screened d and f orbitals, which have narrow bandwidths (small hopping t). Depending on external parameters like temperature, doping, strain, or electric field, the relative strength of correlations U with respect to the bandwidth ($\propto t$) can be modified and can give rise to phase transitions such as a metal-to-insulator transition (MIT). Fig. 2.2 b shows the rich phase diagram of a typical high-T$_c$ superconductor, a hallmark example of a correlated material.

2.3 . Rashba Spin-Orbit Coupling in Solids

The Rashba spin-orbit coupling (SOC) is a fundamental phenomenon observed in materials where inversion symmetry is broken, such as at surfaces, interfaces, or in certain bulk crystals lacking a center of symmetry. This interaction leads to a momentum-dependent splitting of spin bands, causing the electron's spin orientation to depend on its momentum—a feature known

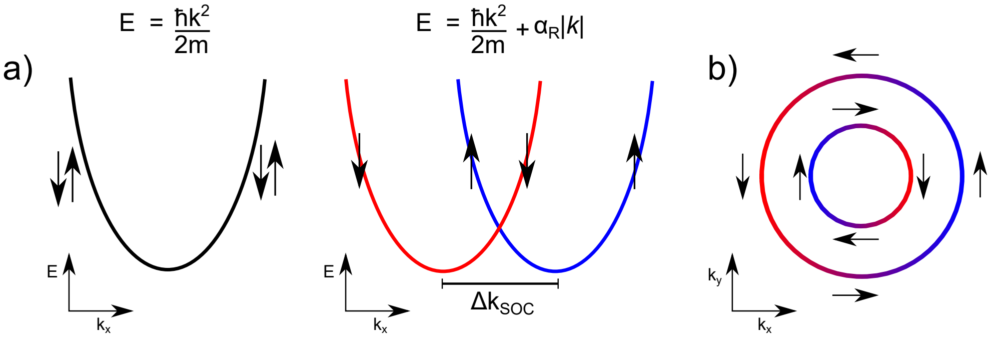

Figure 2.3 – Schematic of band dispersion : a) for a free electron and with Rashba SOC ; b) in-plane spin-momentum texture in a Rashba-split band. Arrows indicate electron spin direction.

as spin-momentum locking. Phenomenologically, the Rashba effect arises because the absence of inversion symmetry in a crystal creates an internal electric field, which, through relativistic effects, couples the electron's spin to its motion.

An electron with velocity $\mathbf{v}$ in an electric field $\mathbf{E}$ feels an effective magnetic field $\mathbf{B}_{\text{eff}}$ in its rest frame, given by [42]

$$\mathbf{B}_{\text{eff}} = \frac{\mathbf{v} \times \mathbf{E}}{c^2} \tag{2.16}$$

In crystals, this electric field $\mathbf{E}$ can arise from the breaking of inversion symmetry in the material, for example, by an applied electric field or at the surface. On the surface of a crystal, the potential felt by an electron out of the plane is asymmetric due to the presence of a vacuum discontinuity. This asymmetric potential gives rise to an electric field $\mathbf{E}$, which is equal to the negative gradient of the potential : $\mathbf{E} = -\nabla V$. In a crystal lattice, electrons move through the electric fields generated by ions. Heavier ions mean higher nuclear charge Z and stronger electric fields generated.

The electron spin magnetic moment $\boldsymbol{\mu}_s$ interacts with $\mathbf{B}_{\text{eff}}$, which gives rise to an additional term in the electronic Hamiltonian H given by

$$H_{\text{SOC}} = -\boldsymbol{\mu}_s \cdot \mathbf{B}_{\text{eff}} \tag{2.17}$$

This can also be expressed as

$$H_{\text{SOC}} = \frac{g_s \mu_B}{\hbar c^2} (\mathbf{S} \cdot (\mathbf{v} \times \mathbf{E})) \tag{2.18}$$

where we have expanded $\boldsymbol{\mu}_s = -\frac{g_s \mu_B}{\hbar}\mathbf{S}$, with g_s as the electron g-factor, μ_B the Bohr magneton, and $\mathbf{S}$ the electron spin.

By using the fact that $\mathbf{v} = \mathbf{p}/m$ and $\mathbf{p} = \hbar\mathbf{k}$, where $\mathbf{p}$ is the electron momentum and $\mathbf{k}$ is the electron's wavevector, we can finally write

$$H_{\mathrm{SOC}} = \alpha_{\mathrm{R}}(\mathbf{S} \times \mathbf{k}) \cdot \hat{\mathbf{E}} \tag{2.19}$$

where $\alpha_{\mathrm{R}} = \left(\frac{g_s \mu_B}{mc^2}\right) E$ is the Rashba coupling constant, and $\hat{\mathbf{E}}$ is the direction of the electric field $\mathbf{E}$.

The inclusion of H_{SOC} in a free electron-like Hamiltonian results in a modification of the dispersion relation as given by [18]

$$E_{\pm}(\mathbf{k}) = \frac{\hbar^2 k^2}{2m} \pm \alpha_{\mathrm{R}} |\mathbf{k}| \tag{2.20}$$

where $\pm$ denotes the spin orientation. The linear term $\alpha_{\mathrm{R}}|\mathbf{k}|$ causes a splitting of the energy bands and shifts the energy minima away from $k = 0$, resulting in momentum-shifted dispersions.

The bottoms of the bands for the two branches lie at momentum k_0

$$k_0 = \mp \frac{m\alpha_{\mathrm{R}}}{\hbar^2} \tag{2.21}$$

and the total momentum shift between the dispersions of the two spin orientations is $\Delta k_{\text{SOC}} = \frac{2m\alpha_{\mathrm{R}}}{\hbar^2}$.

The spin expectation value of the eigenstates of this Hamiltonian is given by

$$\langle \boldsymbol{\sigma} \rangle_{\pm} = \pm \frac{\hat{\mathbf{z}} \times \mathbf{k}}{k} \tag{2.22}$$

which means that the spins are oriented perpendicular to both the electric field direction $\hat{\mathbf{z}}$ and the momentum $\mathbf{k}$, giving rise to a helical spin texture.

2.4 . Density Functional Theory

Density Functional Theory (DFT) is a powerful method for performing ab initio calculations to understand the electronic structure in many-body systems. The theoretical basis of DFT rests on two important theorems, known as the Hohenberg-Kohn (H-K) theorems, established by Walter Kohn and Pierre Hohenberg [48]. These two key theorems are summarized as follows :

- **Theorem 1** : For a system of interacting particles in an external potential $V(r)$: the potential is uniquely determined, up to a constant, by the ground-state particle density $n(r)$.
- **Theorem 2** : There exists a universal functional for the total energy, $E[n]$, which is expressed in terms of the electron density $n(r)$: This functional applies to any external potential $V(r)$. For a given $V(r)$, the true ground-state energy is the global minimum of this functional, and the corresponding density is the exact ground-state electron density.

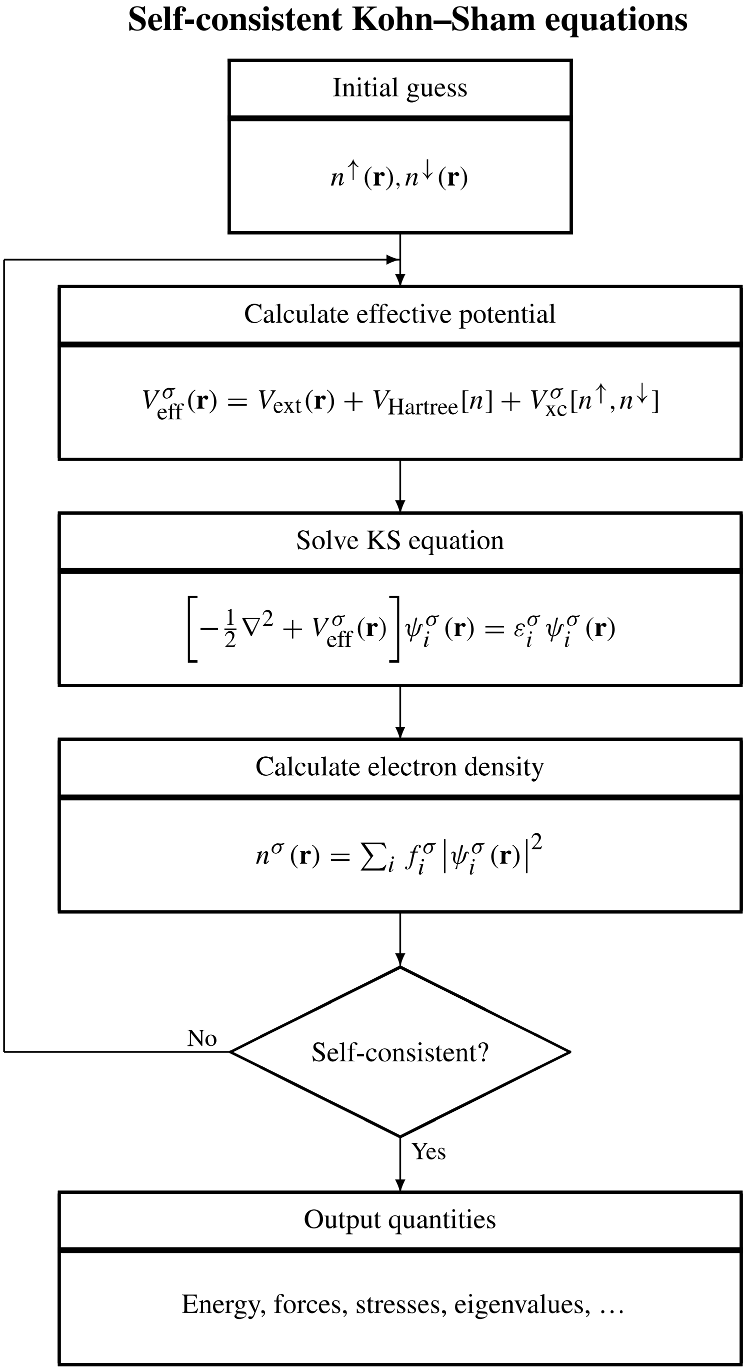
Self-consistent Kohn–Sham equations
Initial guess
$n^{\uparrow}(\mathbf{r}), n^{\downarrow}(\mathbf{r})$
Calculate effective potential
$V_{\text{eff}}^{\sigma}(\mathbf{r}) = V_{\text{ext}}(\mathbf{r}) + V_{\text{Hartree}}[n] + V_{\text{xc}}^{\sigma}[n^{\uparrow}, n^{\downarrow}]$
Solve KS equation
$\left[-\frac{1}{2}\nabla^2 + V_{\text{eff}}^{\sigma}(\mathbf{r})\right]\psi_i^{\sigma}(\mathbf{r}) = \varepsilon_i^{\sigma}\psi_i^{\sigma}(\mathbf{r})$
Calculate electron density
$n^{\sigma}(\mathbf{r}) = \sum_i f_i^{\sigma}\left|\psi_i^{\sigma}(\mathbf{r})\right|^2$
No
Self-consistent?
Yes
Output quantities
Energy, forces, stresses, eigenvalues, …

Figure 2.4 – From [85]. Schematic illustration of the self-consistent procedure for solving the Kohn-Sham equations.

Using these theorems, we can define an energy functional in terms of the electron density :

$$E_{HK} = T[n] + E_{int}[n] + \int d^3r V_{ext}(r)n(r) + E_{II} \tag{2.23}$$

Here, $T[n]$ refers to the kinetic energy, $E_{int}[n]$ represents electron-electron interaction, the term $\int d^3r V_{ext}(r)n(r)$ describes the interaction between the electrons and the external potential (typically from nuclei), and E_{II} accounts for the interaction between nuclei.

Although this reformulation seems to simplify the problem by replacing equations for individual electrons with a functional of the particle density, it remains analytically unsolvable due to complex many-body interactions. To manage this, Walter Kohn and Lu Jeu Sham proposed an alternative framework, reducing the problem to non-interacting electrons in an effective potential [61]. In the Kohn-Sham (K-S) approach, the energy functional is expressed as :

$$E_{KS} = T_s[n] + \int d^3r V_{ext}(r)n(r) + E_{Hartree}[n] + E_{II} + E_{XC}[n] \tag{2.24}$$

In this formulation, T_s denotes the kinetic energy of non-interacting electrons, written as :

$$T_s = -\frac{1}{2}\sum_{\sigma}\sum_{i=1}^{N^\sigma}\langle\psi_i^\sigma|\nabla^2|\psi_i^\sigma\rangle = \frac{1}{2}\sum_{\sigma}\sum_{i=1}^{N^\sigma}\int d^3r|\nabla\psi_i^\sigma(r)|^2 \tag{2.25}$$

where $\psi_i^\sigma(r)$ is the electronic wavefunction of a spin σ electron indexed by i and N^σ is the total number of electrons in spin state σ. The term $E_{Hartree}$ refers to the classical Coulomb interaction between the electron densities :

$$E_{Hartree} = \frac{1}{2}\int d^3r, d^3r' \frac{n(r)n(r')}{|r-r'|} \tag{2.26}$$

while E_{XC} encapsulates exchange and correlation effects, which are typically approximated for practical calculations.

Minimizing the Kohn-Sham energy functional with respect to the wavefunctions leads to Schrödinger-like equations :

$$(H_{KS}^\sigma - \varepsilon_i^\sigma)\psi_i^\sigma(r) = 0 \tag{2.27}$$

where ε_i^σ are the Kohn-Sham eigenvalues, and the Kohn-Sham Hamiltonian H_{KS}^σ is given by :

$$H_{KS}^\sigma = -\frac{1}{2}\nabla^2 + V_{KS}^\sigma \tag{2.28}$$

with the effective potential V_{KS}^σ defined as :

$$V_{KS}^\sigma = V_{ext}(r) + \frac{\partial E_{Hartree}}{\partial n(r,\sigma)} + \frac{\partial E_{XC}}{\partial n(r,\sigma)} = V_{ext}(r) + V_{Hartree}(r) + V_{XC}(r) \tag{2.29}$$

These equations are typically solved self-consistently, as depicted in fig. 2.4.

The accuracy of the resulting solutions is dependent on the quality of the exchange-correlation approximation E_{XC}. A common approximation is the Local Density Approximation (LDA), where the exchange-correlation functional depends solely on the local electron density :

$$E_{XC}^{LDA} = \int \varepsilon_{XC}(n)n(r), d^3r \tag{2.30}$$

In this work, we frequently use the Perdew–Burke–Ernzerhof (PBE) functional [98], which belongs to the class of Generalized Gradient Approximation (GGA) functionals. Unlike LDA, GGA takes into account both the electron density and its gradient, which helps to capture the inhomogeneity of the electron density :

$$E_{XC}^{GGA} = \int \varepsilon_{XC}(n, \nabla n)n(r), d^3r \tag{2.31}$$

2.4.1 . DFT+U

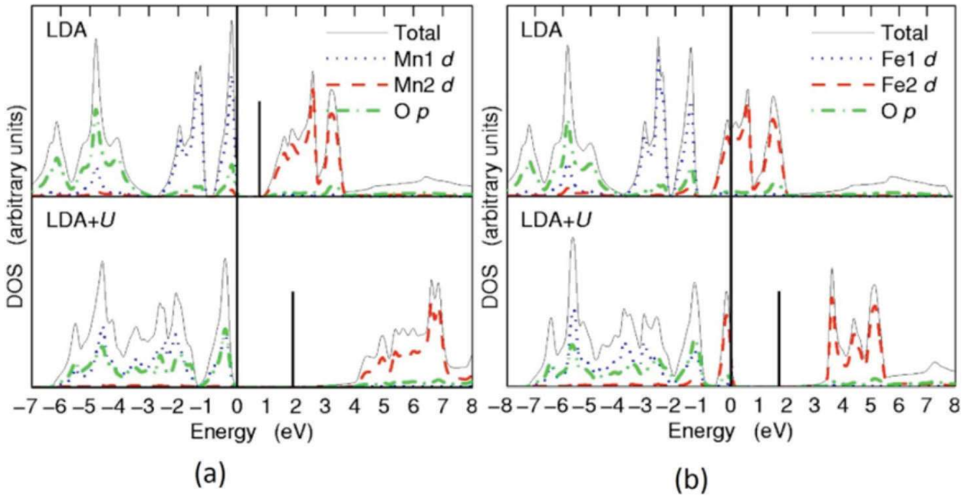

Figure 2.5 – Density of states (DOS) calculated by LDA and LDA+U for (a) MnO and (b) FeO. Notice the opening of the band gap in LDA+U. Adapted from [129].

Density functional theory (DFT) has proven to be highly successful in systems where electronic interactions are relatively weak, and where quasiparticle-like excitations can describe the system's behavior. However, it struggles to accurately describe systems dominated by strong electronic correlations, such as Mott insulators [16][92]. In these systems, strong Coulomb interactions localize electrons on specific orbitals, resulting in insulating behavior. Standard DFT functionals like LDA (local density approximation) and GGA (generalized gradient approximation) often over-delocalize valence electrons, leading to an erroneous prediction of metallic ground states and a failure to capture the physics of strong correlation and electron localization.

Referring back to the Hubbard model in equation 2.9, when $t \ll U$, where t is the hopping parameter and U is the on-site Coulomb repulsion, an insulating state can emerge. This occurs even with a half-filled band, where electron counting would otherwise predict a conductor. This behavior is not captured by standard DFT, which typically works well when $U \ll t$, where the system exhibits quasiparticle-like excitations.

Although more sophisticated many-body techniques, such as DMFT (dynamical mean field theory) [35] and cluster approximations [47], can handle such strongly correlated behavior, these methods are computationally intensive. In contrast, DFT remains computationally efficient, leading to the development of methods like LDA+U [23] (or more generally, DFT+U), which introduces strong corrections to describe correlated states (like d or f orbitals) while the rest of the electrons are treated in the original DFT framework.

In the DFT+U approach, the total energy functional is modified as :

$$E_{\text{LDA+U}}[\rho(r)] = E_{\text{LDA}}[\rho(r)] + E_{\text{Hub}}[n^{I\sigma}_{mm'}] - E_{\text{dc}}[n^{I\sigma}] \tag{2.32}$$

Here, E_{Hub} represents the electron-electron interaction as described by the Hubbard model, while E_{dc} is the double-counting correction, which removes interaction energy already included in the E_{LDA} term to avoid double-counting errors. The occupation number of localized orbitals is represented by $n^{I\sigma}_{mm'}$, where m, m' index the localized states at site I. This can be represented as the projection of the occupied Kohn-Sham wavefunctions ψ^{σ}_{kv} with momentum k and band index v on the localized basis set, $\phi^{I,\sigma}_{m}$, as

$$n^{I\sigma}_{mm'} = \sum_{k,v} f^{\sigma}_{kv} \langle \psi^{\sigma}_{kv} | \phi^{I,\sigma}_{m'} \rangle \langle \phi^{I,\sigma}_{m} | \psi^{\sigma}_{kv} \rangle \tag{2.33}$$

where f^{σ}_{kv} is the Fermi-Dirac occupation of Kohn-Sham states.

As described in [27], the total Hubbard correction, $E_U = E_{\text{Hub}} - E_{\text{dc}}$, can be simplified to

$$E_U[n^{I\sigma}_{mm'}] = \sum_{I,\sigma} \frac{U^I}{2} \text{Tr}[\mathbf{n}^{I,\sigma}(1 - \mathbf{n}^{I,\sigma})] \tag{2.34}$$

where only one effective parameter U^I is used for the correlations. $\mathbf{n}^{I,\sigma}$ is the matrix for the occupation of electrons in localized orbitals.

Even this simplified approach with effective correlation term U has been successfully used to describe many materials. Specifically, these calculations have been able to describe the formation of band gaps in correlated materials which are otherwise ungapped in DFT calculations (fig. 2.5) [127]. In coordination with experiments, DFT+U calculations have enabled us to have a much better understanding of the electronic structure of correlated materials.

3 - Experimental Techniques

This work primarily utilizes the experimental techniques of angle resolved photoemission spectroscopy (ARPES) and Scanning Tunneling Microscopy/ Spectroscopy (STM/STS) to investigate the electronic properties of the materials under investigation. The following is a short primer on the details of these techniques.

3.1 . Angle resolved photoemission spectroscopy

3.1.1 . Photoelectric effect

Angle resolved photoemission spectroscopy (ARPES) is a powerful tool which directly probes the electronic band structure and interactions in a material. It is based on the phenomenon of the photoelectric effect, which was first observed and documented in the 19th century by Heinrich Hertz, Aleksandr Stoletov, and Philipp Lenard. A concrete mathematical description was provided later by Albert Einstein, who was awarded the Nobel Prize in Physics in 1921 for "his discovery of the law of the photoelectric effect" [28].

Now, the photoelectric effect is essentially the observation that some materials eject electrons when illuminated by photons, mostly in the ultraviolet (UV) energy range. These ejected electrons must follow the conservation of energy principle, and from that, we derive the relation :

$$E_{\text{kin}} = h\nu - W - |E_B| \tag{3.1}$$

where E_{kin} is the kinetic energy of the ejected electron, $h\nu$ is the energy of the incoming photon, W is the work function of the material, i.e., the minimum energy required to free an electron at the surface of the material from the electrostatic attractive force and place it at a point outside in the vacuum, and E_B is the binding energy of the electron inside the solid.

Therefore, by illuminating a material with light above the threshold of its work function and measuring the kinetic energy of the outgoing electrons, we get information about the energetic character of the bound electrons inside the material. This phenomenon is widely utilized in the technique called X-ray photoelectron spectroscopy, to study the chemical composition and electronic structure of materials [29].

If we are dealing with crystalline materials with the conservation of translational symmetry, the outgoing electrons are also subject to another conservation law : the conservation of momentum. Therefore, they must also follow the following relation :

$$\mathbf{p}_{\parallel} = \hbar\mathbf{k}_{\parallel} = \sqrt{2mE_{\text{kin}}} \cdot \sin\vartheta \tag{3.2}$$

where $\mathbf{p}_{||}$ is the momentum of the ejected electron parallel to the plane of the material, which is equal to $\mathbf{k}_{||}$, the momentum of the electron parallel to the surface inside the material. ϑ is the angle between the normal to the material surface and the angle of the incoming photon.

This second conservation law allows us to directly probe the momentum dispersion of crystalline materials, offering much richer insight into their properties compared to just the energy landscape of the bound electrons. This insight has been precisely exploited by the development of ARPES since the 1960s, after the breakthrough in the development of microchannel plates [126], which allowed precise position tracking of ejected electrons in space.

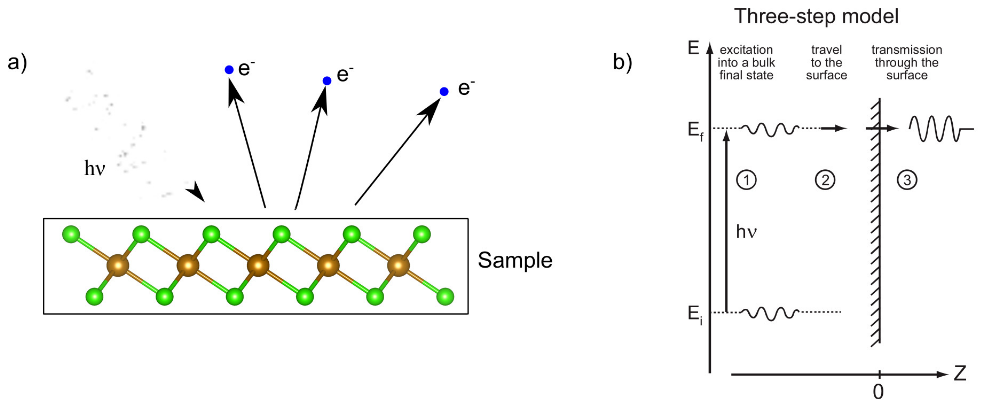

Figure 3.1 – a) Cartoon representation of Einstein's photoelectric effect. b) Schematic of the three-step model of photoemission, adapted from [49].

3.1.2 . The 3-step model of photoemission

To quantify the process of photoemission, a commonly used framework called the 3-step model is applied.

This 3-step model of photoemission entails :

1. Excitation of electrons in the material bulk by incoming photons.
2. Travel of the excited electrons to the material surface.
3. Escape of the electrons into the vacuum.

Excitation of electron in the material bulk by incoming photon

The incoming photon excites the electron in the bulk from its initial state in an N-electron wavefunction ψ_i^N to the final state ψ_f^N, and the probability of this excitation is given by Fermi's golden rule :

$$w_{f,i} = \frac{2\pi}{\hbar} \left|\langle\psi_f^N|\mathbf{H}_{\text{int}}|\psi_i^N\rangle\right|^2 \delta\left(E_f - E_i - \hbar\omega\right) \tag{3.3}$$

where $w_{f,i}$ is the transition probability between the initial and final state wavefunctions, $\mathbf{H}_{\text{int}}$ is the interaction Hamiltonian governing the light-matter

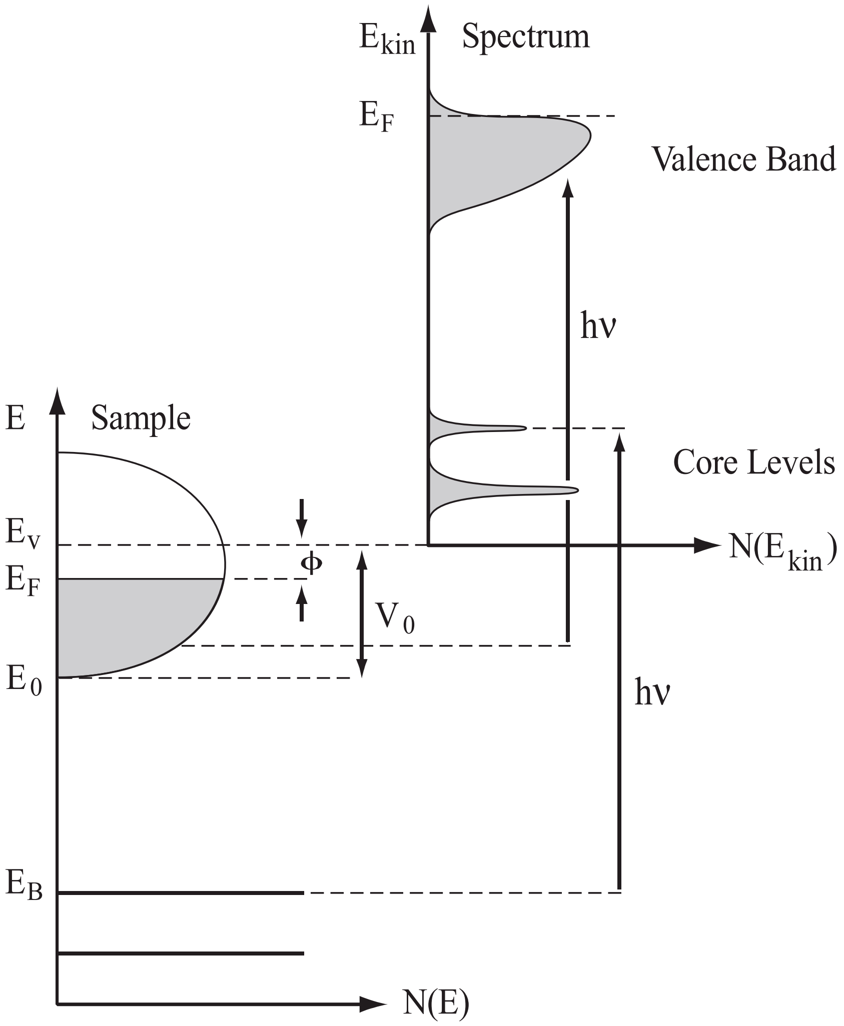

Figure 3.2 – Representation of the excitation of an electron in a material with binding energy E_B to some kinetic energy E_{kin} by a photon with energy $h\nu$. From [49].

interaction, and E_f, E_i are the energies of the electron in the final and initial states, respectively.

The interaction Hamiltonian in the electron system with perturbations due to the electromagnetic field, in the gauge where the electromagnetic scalar field $\Psi = 0$, can be approximated as :

$$H_{\text{int}} = \frac{e}{2mc}(\mathbf{A}\cdot\mathbf{p} + \mathbf{p}\cdot\mathbf{A}) \tag{3.4}$$

where we have dropped the quadratic terms in $\mathbf{A}$, which are negligible in the linear optical regime. Here, $\mathbf{A}$ is the electromagnetic vector potential, and $\mathbf{p}$ is the electron momentum.

Now, $[\mathbf{p}, \mathbf{A}] = -i\hbar\nabla \cdot \mathbf{A}$, and in the UV regime, $\mathbf{A}$ can be approximately considered constant over atomic distances, as the wavelength of UV light (100–4000 Å) is much larger than interatomic distances (few Å). This results in $\nabla \cdot \mathbf{A} = 0$, and the interaction Hamiltonian can now be written as :

$$\mathbf{H}_{\text{int}} = -\frac{e}{mc}\mathbf{A} \cdot \mathbf{p} \tag{3.5}$$

and,

$$w_{f,i} = \frac{2\pi}{\hbar}\left|\left\langle \psi_f^N \left| -\frac{e}{mc}\mathbf{A} \cdot \mathbf{p} \right| \psi_i^N \right\rangle\right|^2 \delta\left(E_f - E_i - \hbar\omega\right) \tag{3.6}$$

The N-electron wavefunction ψ_N can be decomposed into a Slater determinant of a one-electron state and an N-1-electron state, i.e., $\psi^N = \mathcal{A}\phi^k\Psi^{N-1}$, where $\mathcal{A}$ is the antisymmetrization operator and ϕ^k is the one-electron wavefunction of an electron with momentum k.

We can use this to write

$$\begin{aligned}\langle\Psi_f^N \left| -\frac{e}{mc}\boldsymbol{A} \cdot \boldsymbol{p} \right| \Psi_i^N\rangle &= \langle\phi_f^k \left| -\frac{e}{mc}\boldsymbol{A} \cdot \boldsymbol{p} \right| \phi_i^k\rangle\langle\Psi_m^{N-1}|\Psi_i^{N-1}\rangle \\ &\equiv M_{f,i}^k\langle\Psi_m^{N-1} \mid \Psi_i^{N-1}\rangle\end{aligned} \tag{3.7}$$

where m is the index given to the N-1 final state wavefunction and $M_{f,i} = \langle\phi_f^k \left| -\frac{e}{mc}\boldsymbol{A} \cdot \boldsymbol{p} \right| \phi_i^k\rangle$.

The total photoemission intensity (sum over all possible initial and final states), as a function of electron momentum $\mathbf{k}$ and kinetic energy E_{kin}, $I(\boldsymbol{k}, E_{\text{kin}}) = \sum_{f,i} w_{f,i}$, is given as :

$$I\left(\boldsymbol{k}, E_{kin}\right) = \sum_{f,i}\left|M_{f,i}^k\right|^2 \sum_m \left|c_m\right|^2 \delta\left(E_{kin} + E_m^{N-1} - E_i^N - hv\right) \tag{3.8}$$

where $|c_m|^2 = |\langle\Psi_m^{N-1} \mid \Psi_i^{N-1}\rangle|^2$. The term $|M_{f,i}^k|^2$ is known as the ARPES matrix element and modifies the photoemission intensity depending on the symmetry of the incoming light with respect to the sample geometry and the initial state of the electronic wavefunction.

The rest of the photoemission intensity involving the sum over excited states m constitutes the one-electron removal spectral function A.

$$A = \sum_m \left|c_m\right|^2 \delta\left(E_{kin} + E_m^{N-1} - E_i^N - hv\right) \tag{3.9}$$

ARPES matrix elements

By using the commutation relation $\hbar\mathbf{p}/m = -i[\mathbf{x}, H]$, the matrix element term $|M_{f,i}^k|^2$ is proportional to $\left|\left\langle \phi_f^{\mathbf{k}}|\varepsilon \cdot \mathbf{x}|\phi_i^{\mathbf{k}}\right\rangle\right|^2$, where ε is the unit vector pointing in the direction of $\mathbf{A}$ and $\mathbf{x}$ is the position operator.

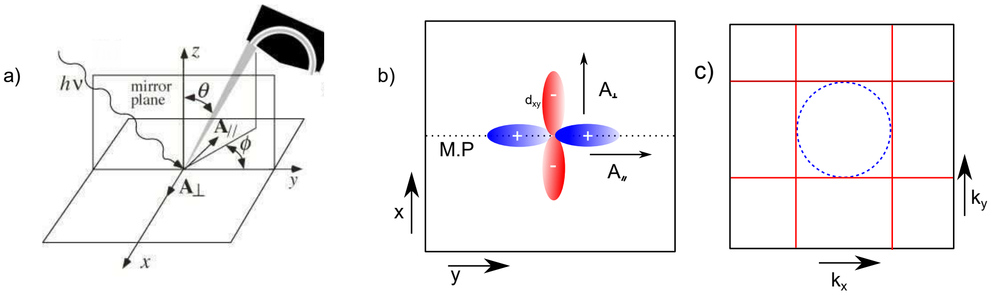

Figure 3.3 – a) Geometry of the ARPES setup. θ and ϕ angles define the angle of emitted photoelectrons. $A_{\|}$ and $A_{\perp}$ are the parallel and perpendicular components of **A**, respectively, with respect to the mirror plane. b) Top-down view of the sample with the symmetry of the d$_{xy}$ orbital with respect to the mirror plane (M.P.). c) Momentum space schematic of the Fermi surface of SrVO$_3$. The blue circle corresponds to the contribution of the d$_{xy}$ orbital and would change intensity depending on the light polarization direction in b.

Consider the scenario demonstrated in fig. 3.3 b. We have the d$_{xy}$ orbital, which is antisymmetric in the mirror plane, and the detector is located in the mirror plane. To have a non-vanishing photoemission intensity, $\left|\left\langle \phi_f^{\mathbf{k}} | \varepsilon \cdot \mathbf{x} | \phi_i^{\mathbf{k}} \right\rangle\right|^2 \neq 0$. Now, $\phi_f^{\mathbf{k}}$ must be even, as an odd wavefunction is zero everywhere in the mirror plane, and therefore it is zero at the detector. This then implies that $\varepsilon \cdot \mathbf{x} | \phi_i^{\mathbf{k}} \rangle$ must be an even function for a non-zero integral. The direction of light polarization given by the vector ε determines the parity of the $\varepsilon \cdot \mathbf{x}$ term, which can be even with light polarized parallel to the mirror plane (p-polarized) or odd if it is perpendicular to the mirror plane (s-polarized). In the case of our d$_{xy}$ orbital, the initial state wavefunction $\phi_i^{\mathbf{k}}$ is odd in the mirror plane, so the light has to be s-polarized to get some photoemission signal at the detector. This can be summarized by :

$$\left\langle \phi_f^{\mathbf{k}} | \mathbf{A} \cdot \mathbf{p} | \phi_i^{\mathbf{k}} \right\rangle \begin{cases} \phi_i^{\mathbf{k}} \text{ even } \langle + | + | + \rangle & \Rightarrow \mathbf{A} \text{ even} \\ \phi_i^{\mathbf{k}} \text{ odd } \langle + | - | - \rangle & \Rightarrow \mathbf{A} \text{ odd} \end{cases} \tag{3.10}$$

This works very well when the sample and the detector geometry are well defined, as in the case of detectors with horizontal slits or slit direction along the mirror plane, where the incoming electrons are mostly collected from the emissions along the mirror plane ; however, with detectors with vertical slits, where the incoming electrons may not lie in the mirror plane, the situation is complicated. More sophisticated methods are required to quantitatively obtain the matrix elements. [91] is a comprehensive review for understanding and simulating ARPES matrix elements for different types of light polarization and the initial state wavefunctions.

One electron removal spectral function

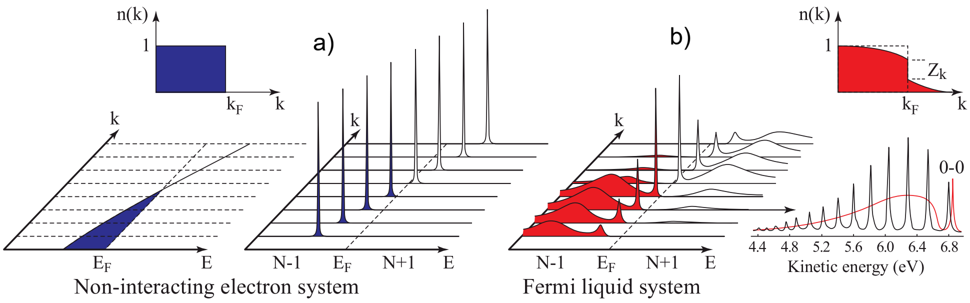

Figure 3.4 – a) Schematic of a single-band non-interacting system. b) Schematic of an interacting Fermi liquid system. Bottom right : Photoelectron spectrum of gaseous hydrogen (black) and ARPES spectrum of solid hydrogen (red). Adapted from [25].

In eq. 3.9, the term $|c_m|^2 = |\langle \Psi_m^{N-1} \mid \Psi_i^{N-1} \rangle|^2$ is non-zero only when $m = i$, i.e. if the final state wavefunctions Ψ_m^{N-1} are still the eigenstates of the initial N-1-electron Hamiltonian. This will produce Dirac delta peaks at the energies of the N-1 initial state wavefunction. However, in real systems with electron-electron interactions, the final state can no longer be described by a single wavefunction and is a superposition of initial state wavefunctions. Introducing such electronic correlations will change the magnitude and width of the original Dirac delta peaks.

These modifications to the spectral function in the presence of electronic correlations can be derived from the modified Green's function, which represents the propagation of an electron in a system, and is given by :

$$G(\mathbf{k}, \omega) = \frac{1}{\omega - \varepsilon^b_{\mathbf{k}} - \Sigma(\mathbf{k}, \omega)} \tag{3.11}$$

.

where ω is the energy of the particle, $\varepsilon^b_{\mathbf{k}}$ is the bare band dispersion energy at momentum k, and $\Sigma(\mathbf{k}, \omega)$ is a complex quantity called the electron self-energy, which encodes the electronic correlations. The self-energy can be expanded into its real and imaginary parts, $\Sigma(\mathrm{k}, \omega) = \Sigma'(\mathrm{k}, \omega) + i\Sigma''(\mathrm{k}, \omega)$. The real part $\Sigma'(\mathrm{k}, \omega)$ contains information about the energy shift or the energy renormalization of the electron, while the imaginary part $\Sigma''(\mathrm{k}, \omega)$ gives information about the lifetime of the electron.

The one-particle spectral function is given by $-(1/\pi)\,\mathrm{Im}\,G(\mathrm{k}, \omega)$ [111], and we can arrive at the expression :

$$A(\mathrm{k}, \omega) = -\frac{1}{\pi} \frac{\Sigma''(\mathrm{k}, \omega)}{\left[\omega - \varepsilon^b_{\mathbf{k}} - \Sigma'(\mathbf{k}, \omega)\right]^2 + [\Sigma''(\mathrm{k}, \omega)]^2} \tag{3.12}$$

.

The self-energy can thus be obtained from high-resolution ARPES experiments by fitting the imaginary and real parts of the self-energy to the broadening and energy shift of bands, respectively [32].

Travel of the excited electron to the material surface

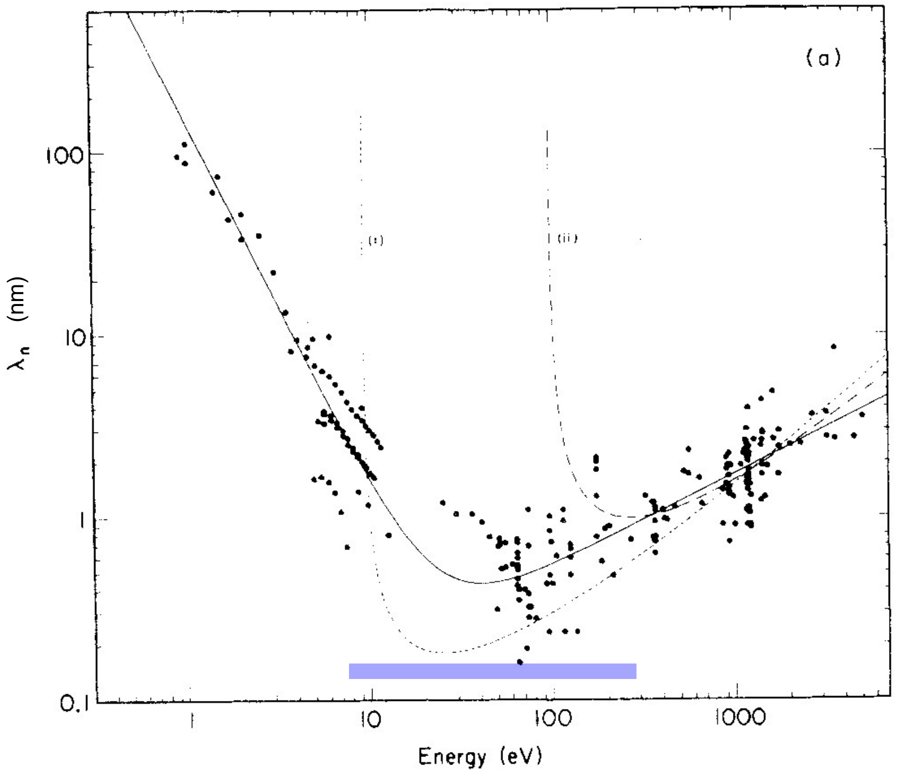

Figure 3.5 – Compilation of inelastic mean free path of various materials. Blue bar indicates typical operating energy in ARPES experiments. Adapted from [113].

The excited electron from the bulk must now travel to the sample surface before it can leave the sample. On its way, it can interact with other electrons and scatter. For the electron to preserve its initial momentum, its mean free path in the material must be greater than its path length from the bulk to the surface.

In general, the mean free path λ_n of the excited electrons has been observed to fit the empirical relation [113] (fig. 3.5) :

$$\lambda_{\rm n} = \frac{538}{E^2} + 0.41aE^{1/2} \text{ nm} \tag{3.13}$$

where a is the thickness of one monolayer of the material, in nanometers (nm), and E is the electron kinetic energy in eV.

Escape of the electron into vacuum

Once the electron reaches the surface, it must overcome the potential well of the surface to escape the material, defined by the work function W of the material. Therefore, it loses energy equal to W from its total energy before it can escape into vacuum (eq. 3.1).

The electron does not preserve its crystal momentum normal to the material surface due to the surface-vacuum discontinuity and the breaking of translational symmetry in the normal direction.

If we assume that the final state wavefunction still follows a parabolic dispersion, we can write :

$$E_f(\mathbf{k}) = \frac{\hbar^2|\mathbf{k}|^2}{2m} + E_0 = \frac{\hbar^2\left(k_\parallel^2 + k_\perp^2\right)}{2m} + E_0 \tag{3.14}$$

.

where E_0 is the energy at the bottom of the assumed parabolic dispersion, and $E_f(\mathbf{k}) = E_B(\mathbf{k}) + h\nu$, and $E_f = E_{\text{kin}} + W$. Thus, we get :

$$\begin{aligned} \hbar k_\perp &= \left[2m\left(E_{\text{kin}}\cos^2\theta + W - E_0\right)\right]^{\frac{1}{2}} \\ &= \left[2m\left(E_{\text{kin}}\cos^2\theta - V_0\right)\right]^{\frac{1}{2}} \end{aligned} \tag{3.15}$$

.

The parameter $V_0 = E_0 - W$ is called the "inner potential" and is a fitting parameter calculated based on the periodicity in the out-of-plane dispersion.

Final ARPES photoemission intensity

In the final stage of detection of the photoelectron at the detector, the intensity is given by :

$$I(\mathbf{k},\omega) = I_0(\mathbf{k},\nu,\mathbf{A})f(\omega)A(\mathbf{k},\omega) \otimes R(\Delta k, \Delta\omega) \tag{3.16}$$

.

where $I_0(\mathbf{k},\nu,\mathbf{A})$ is the matrix element term, and as we are probing only the occupied states with ARPES, we have to multiply the intensity by the Fermi distribution $f(\omega) = \left(e^{\omega/k_BT} + 1\right)^{-1}$. $A(\mathbf{k},\omega)$ is the one-electron removal spectral function. A convolution with the resolution function of the detector $R(\Delta k, \Delta\omega)$ is applied at the end to account for instrumentation limits to photoelectron detection.

3.1.3 . Experimental considerations

Light source

UV light sources required for the photoexcitation process can be produced by lasers (energy range of 6–11 eV), monochromatized gas discharge lamps (photons at discrete energies of 8.4, 9.6, 11.6, 21.2 eV, etc.), or synchrotron facilities, where undulators or wigglers are used to produce photons at variable energies from accelerating electrons (fig. 3.6).

Synchrotron light sources are the most versatile, in the sense that they allow the most freedom with the photon energy and polarization accessible, while also providing a highly intense source of photons. This intensity can come with the tradeoff of the bandwidth of the light (few meV to tens meV) compared to lab-based setups with lasers and gas discharge lamps, which results in a decreased energy resolution in measurements.

Sample environment

The experiments take place in an ultra-high-vacuum (UHV) environment with pressure in the range of 10^{-9} to 10^{-12} mbar. As ARPES is a highly surface-sensitive technique, a UHV environment is important to minimize contamination of the sample surface from molecules like CO_2, O_2, and H_2O in the environment.

Preparation of a clean, atomically flat sample surface is really important before measurement. The exact process of this preparation will depend on the type of sample studied. Some materials can be cleaved in-situ to expose flat crystalline surfaces. Some samples, such as Au(111) and Cu(111), etc., require the sputtering-annealing process, where the surface is bombarded by heavy ions followed by annealing to allow for the surface to reconstruct. Materials with layers separated by van der Waals gaps, like Bi2Se3, transition metal dichalcogenides (TMDCs), and graphene, can be prepared by exfoliating the sample. Finally, some sensitive materials can be directly grown in the UHV environment and transferred to the measurement chamber without being exposed to the outside atmosphere.

The detection process

Fig. 3.6 shows the hemispherical analyzer used to detect the ejected electrons. The analyzer has two concentric hemispheres of radius R_1 and R_2, and a potential difference of V is maintained between the two. Before reaching the entrance of the analyzer, the electrons are decelerated by the electrostatic lens and focused at the entrance slit with aperture width a and acceptance angle α. Only those electrons in an energy range of pass $E_{\text{pass}} = \frac{eV}{(R_1/R_2 - R_2/R_1)}$ can pass through the entrance, which allows us to measure the kinetic energy of electrons with a resolution of $\Delta E_a = E_{\text{pass}}\left(\frac{a}{R_0} + \frac{\alpha^2}{4}\right)$, where $R_0 = \frac{(R_1+R_2)}{2}$. By scanning the decelerating potential in the electrostatic lens, we can record the intensity in a wide range of electron kinetic energy. In the current state-of-the-art analyzers, based on the initial momentum of the elec-

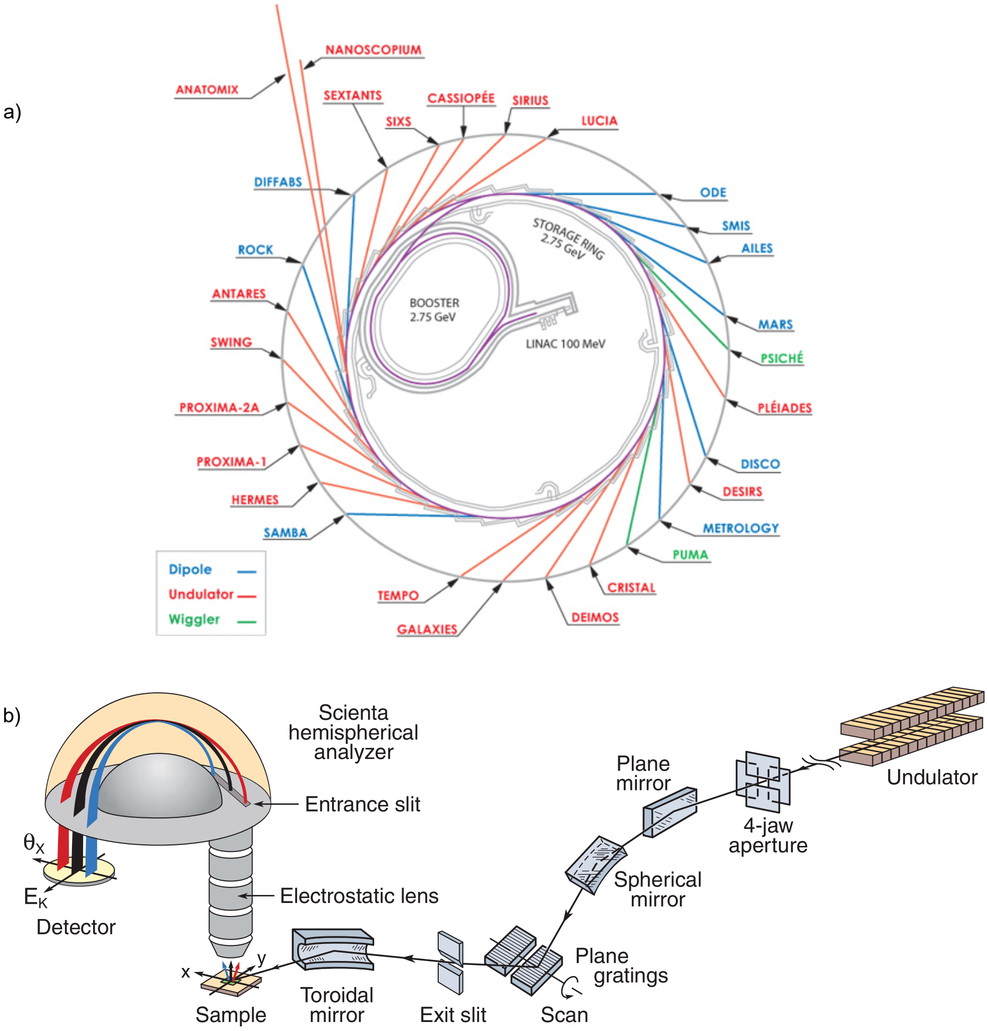
a)
ANATOMIX
NANOSCOPIUM
SEXTANTS
CASSIOPÉE
SIRIUS
SIXS
LUCIA
DIFFABS
ODE
SMIS
AILES
ROCK
STORAGE RING 2.75 GeV
BOOSTER 2.75 GeV
LINAC 100 MeV
ANTARES
SWING
MARS
PSICHÉ
PROXIMA-2A
PLÉIADES
PROXIMA-1
DISCO
DESIRS
HERMES
SAMBA
METROLOGY
PUMA
CRISTAL
TEMPO
GALAXIES
DEIMOS
Dipole
Undulator
Wiggler
b)
Scienta hemispherical analyzer
Entrance slit
θX
EK
Detector
Electrostatic lens
x
y
Sample
Toroidal mirror
Exit slit
Scan
Plane gratings
Spherical mirror
Plane mirror
4-jaw aperture
Undulator

Figure 3.6 – a) Map of synchrotron SOLEIL with the location of various beamlines and insertion devices indicated. b) Schematic of a beamline ARPES setup with an analyzer sensitive to both energy and angle information simultaneously. Adapted from [25].

tron, the electron enters the analyzer at different positions of the entrance slit and ends up at different positions in the X direction (fig. 3.6 b) at the end of its journey. By recording the location of this electron by means of micro-channel plates and CCD cameras, we get the momentum resolution. Also, based on the kinetic energy of the electron in a narrow range defined by E_{pass}, it lands at different spots in the Y direction at the detector, thus allowing for simultaneous $E - k$ dispersion measurement along a specific k direction.

The sample can then be rotated perpendicular to the slit direction, and measured to get multiple $E - k$ dispersions, which can then be combined to form a 3-D data volume with the E vs k_x-k_y information. There are some new analyzers, like the DA30-L series from Scienta Omicron, which further remove the need to rotate the sample by using electronic deflection and effectively deflecting the slit position perpendicular to its aperture [1]. This allows the sample position to be fixed throughout the measurement, which is particularly advantageous for small samples and samples with different crystalline domains.

3.1.4 . Analyses of ARPES data

Usually, the extraction of high-quality ARPES data involves long acquisition times (which in recent times have been significantly reduced by new experimental breakthroughs [1], as well as the introduction of machine learning tools [141]). Following the data acquisition, there is a much longer time spent afterwards analyzing the acquired raw data. Some tools commonly used to process the data include :

Analysis of energy distribution curves (EDCs) and momentum distribution curves (MDCs). EDCs and MDCs are basically just slices of the energy-momentum dispersion data along the energy and momentum axis, respectively. Peak positions from MDC cuts at different energies can be extracted by fitting them to Lorentzian or Voigt profiles and thus can be parameterized by fitting the extracted peaks to the function defined by a model Hamiltonian. The extracted information can also be used to gain insight into many-body interactions in the system through self-energy analyses [63]. Momentum-integrated EDCs are often good first-order approximations of the average density of states (DOS) of the system.

Normalization is frequently used to enhance dispersing features in ARPES data. Specifically, normalization of individual EDCs across different momenta, by choosing a specific energy-window like the energy window of the valence band of the system, or noise above the Fermi-level, can help reduce the influence of any anisotropic detector sensitivity. A note of caution with normalization is that it often drastically changes the angular intensity profile of bands, depending on the specific procedure employed, and thus any analyses involving the determination of photoelectric matrix elements is not reliable.

Second derivatives of ARPES measurements along any or all the measurement axes are often used to achieve an accurate determination and resolution of intensity peaks in data, which can often be noisy or have multiple features that are hard to distinguish from the raw data.

3.2 . Scanning Tunneling Microscopy

Scanning tunneling microscopy (STM) is a surface-sensitive experimental technique used to probe atomically flat surfaces with a resolution that could be smaller than individual atoms. In contrast to conventional micro-

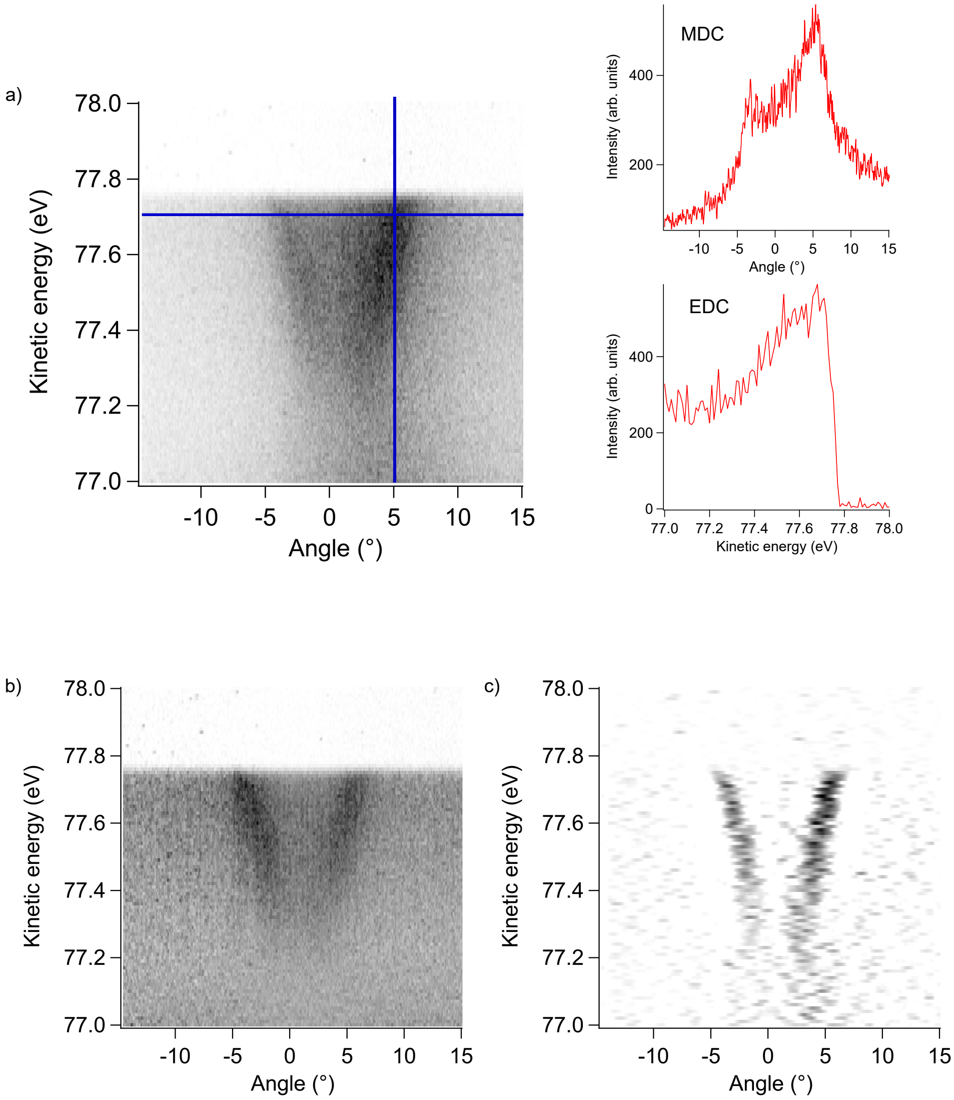

Figure 3.7 – a) A typical kinetic energy–angle dispersion raw data acquired by ARPES. The horizontal and vertical lines represent the MDC and EDC slices shown on the right. b) The same data normalized along the EDC slices. c) The raw data processed to show second derivative intensity peaks along the angular direction.

scopy, which relies on photons to relay information about the fine structure of the object studied, STM, invented by Binnig and Rohrer in the early 1980s [14], relies on the tunneling of electrons from the material to the metallic probe to achieve this.

The STM tip, usually made up of tungsten, platinum-iridium, or a noble metal such as gold and silver, is brought very close to the sample surface, such that the sample and the tip wavefunction overlap. Upon the application of a

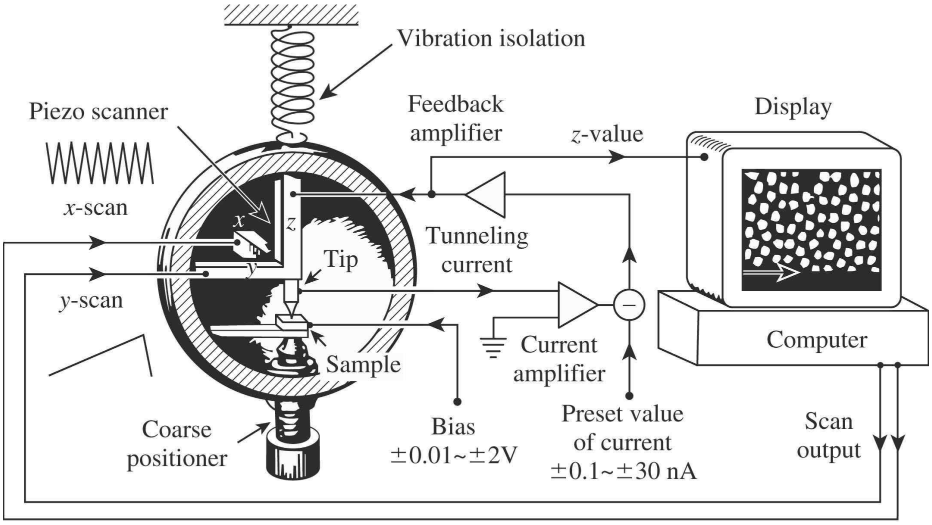
Vibration isolation
Piezo scanner
Feedback amplifier
z-value
Display
x-scan
x
z
y
Tip
Tunneling current
y-scan
Sample
Current amplifier
Computer
Coarse positioner
Bias ±0.01~±2V
Preset value of current ±0.1~±30 nA
Scan output

Figure 3.8 – Scanning tunneling microscope in a nutshell. From [22]

small bias voltage V, between the sample and the tip, which acts as the two electrodes in the closed system, there is a flow of electrons from the sample to the tip and vice-versa.

The tip is attached to a piezodrive, consisting of three orthogonal piezoelectric transducers, which control the expansion and contraction of the piezodrive along the x, y, and z directions in response to an applied voltage. This piezoelectric system allows for fine motor control on the scale of angstroms or smaller.

If the bias is small, the tunneling current I can be approximated by

$$I \propto \frac{CV}{z} e^{-2\kappa z} \tag{3.17}$$

where C is a constant, z is the separation length between the tip and the sample, and κ is the inverse decay length [118].

3.2.1 . Experimental considerations

As STM is extremely sensitive to the sample surface, to obtain information about pure sample surfaces, a UHV environment with pressure in the range of 10^{-10} to 10^{-12} mbar is essential. In addition to the same UHV environment constraints encountered with ARPES, we now have the additional complexity of isolating the physical tip, which scans the sample surface, from any environmental effects. This means complete electrical and vibrational isolation for the STM setup. Nowadays, mechanical or gas springs are typically used for vibration isolation in the STM setup. The tip head itself is also isolated from the main body of the STM.

3.2.2 . Operating modes

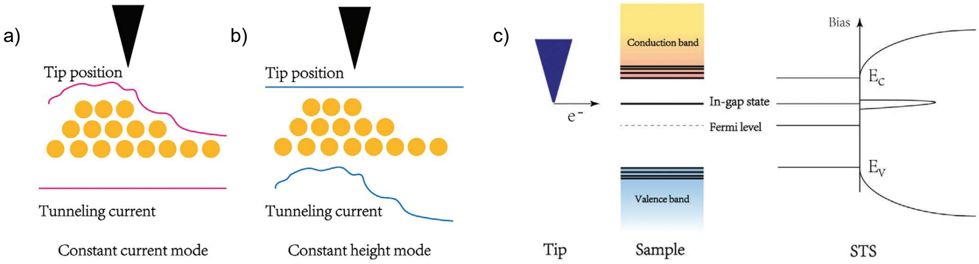

Figure 3.9 – a) Constant current and b) constant height operating modes of STM/STS. c) Schematic of STS measurements. The sample is polarized with respect to the tip which is grounded. Adapted from [96]

STM is typically operated in two modes : the constant-height mode and the constant-current mode.

As the name suggests, during constant-height mode, the z-motor is locked at a fixed height, and the tunneling current is recorded as a function of the x-y position. The contrast in the 2-D image obtained then is the contrast of the tunneling current (which is a function of sample-tip distance as well as the local density of states). As the feedback system, which controls the z-motor as a function of the tunneling current, is not in operation, the processing overhead is greatly reduced, allowing for much faster scans of the surface and potentially enabling time-resolved measurements. One potential downside is that this technique requires atomically flat surfaces ; otherwise, the tip can easily crash into the sample.

In the constant-current mode, the tunneling current is set constant for the set sample bias. As the tip moves over the surface, to compensate for changes in the tunneling current, the tip z-distance is modulated by a feedback loop. In this way, we can track the surface topography, and it is especially useful in samples with rough surface morphology.

3.2.3 . Scanning tunneling spectroscopy (STS)

STS is used to obtain information about the local density of states (LDOS) of the sample, as a function of the sample bias. The basic mechanism of electron tunneling for the STS measurements is illustrated as follows.

The electron tunneling current I from the sample to the tip can be given by

$$I = \int_0^{eV} T(E, eV, z)\rho_s(E)\rho_t(E, eV)dE \tag{3.18}$$

where $\rho_s(E)$ represents the DOS of the sample, and $\rho_t(E, eV)$ represents the DOS of the tip. $T(E, eV, z)$ is the transmission coefficient, which gives the probability of electron tunneling from the sample to the tip at the sample bias V

and the tip distance z. Under the assumption of a one-dimensional potential barrier between the tip and the sample, we can write $T(E, eV, z)$ as

$$T(E, eV, z) = e^{-z\sqrt{\frac{4m}{\hbar^2}(\phi_t+\phi_s+eV-2E)}}. \tag{3.19}$$

where ϕ_t and ϕ_s are the tip and sample work functions. Here, we have implicitly assumed that only the electron states from the Γ point contribute to tunneling. When working in the usual open feedback mode, where the tip height is set constant, and if we assume that the tip DOS is also constant in the energy range of our measurements, the tunneling current can be written as

$$I \propto \int_0^{eV} T(E, eV)\rho_s(E)dE \tag{3.20}$$

and,

$$dI/dV \propto e\rho_{\mathrm{s}}(eV)T(eV, eV) + e\int_0^{eV} \rho_{\mathrm{s}}(E)\frac{d}{d(eV)}(T(E, eV))dE. \tag{3.21}$$

As $T(E, eV)$ has an exponential dependence on the sample bias V, the dI/dV signal diverges at higher biases and thus makes direct comparison with LDOS difficult. However, we can normalize the measurement by dividing by I/V, which cancels out the exponential dependence of $T(E, eV)$ [31]. Thus, the normalized conductance is given by

$$\frac{dI/dV}{I/V} = \frac{\rho_{\mathrm{s}}(eV) + \int_0^{eV} \frac{\rho_{\mathrm{s}}(E)}{T(eV,eV)}\frac{d}{d(eV)}(T(E, eV))dE}{\frac{1}{eV}\int_0^{eV} \rho_{\mathrm{s}}(E)\frac{T(E,eV)}{T(eV,eV)}dE} \tag{3.22}$$

and is proportional to the LDOS ρ_{s} of the sample with some background term.

3.2.4 . Quasi Particle Interference

Fourier-transform STM (FT-STM) [100], now more commonly referred to as the quasi-particle interference (QPI) technique, is a well-established method that has been widely applied to study surface states in various metals [121], topological surface states [107], high-temperature superconductors [45], other correlated materials, materials with charge density waves [138], and a host of other interesting materials.

As we have seen before, we can acquire information about the LDOS through STM/STS techniques. An interesting phenomenon observed in the STM topography and dI/dV spatial maps is oscillations around point defects, edges, and impurities on the surface. These oscillations, also known as Friedel oscillations, have a certain wavelength and form a standing wave pattern in the STM image [33].

For point defects on the metallic surface, like Au(111), these oscillations form a circular pattern. This is the result of elastic scattering of electrons of

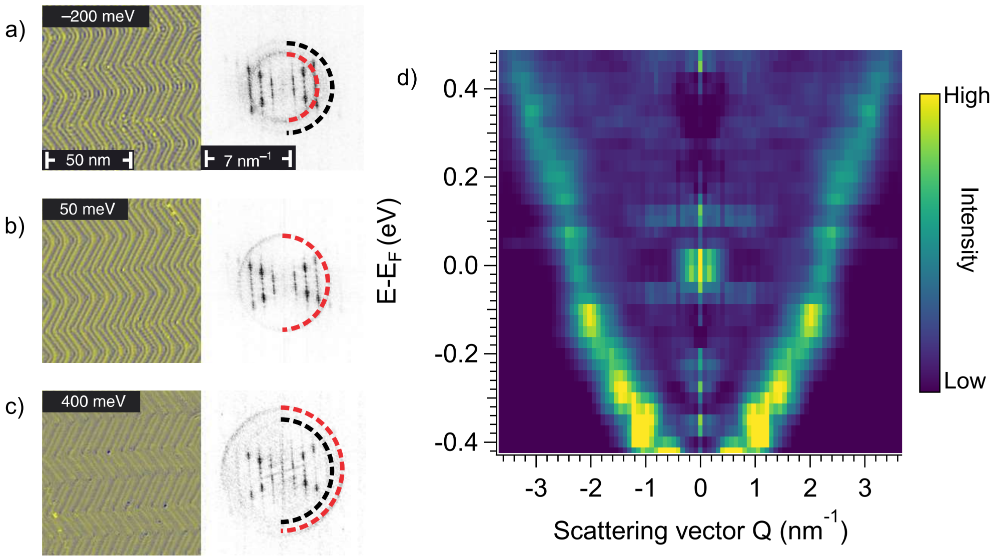

Figure 3.10 – dI/dV images and their FT for the Au(111) surface at a) -200 meV, b) 50 meV, and c) 400 meV. Adapted from [114]. d) **q**-E dispersion extracted from the Au(111) surface. (See Chapter 6)

momentum k_i to k_f at the same energy $\epsilon(k)$. The dominant contribution to scattering on the Au(111) surface states (SS) comes from backscattering, i.e., $k_f = -k_i$. Therefore, the quasiparticle wavefunction $\Psi(k, E)$ will be a standing wave with a wavelength $q = (k_i - k_f)/2 = k_i$, and as LDOS $\propto \Psi(k, E)^2$, the spatial map of LDOS (the dI/dV map) will have standing waves with wavelength $q = 2k_i$ at bias $\epsilon(k_i)$ and $q = 2k_F$ at the Fermi energy $\epsilon(k_F)$.

The scattering wave-vector q, and thus the quasiparticle dispersion wavevector $k = q/2$, can be extracted easily by a Fourier transform of the dI/dV maps. Doing this for maps at different energies, we can obtain a detailed dispersion, as shown in fig. 3.10 b, for the case of Au(111) Shockley states.

3.3 . QPI vs ARPES as electronic structure probes

QPI measurements are a powerful tool to probe momentum-resolved electronic structure, similar to ARPES, but have a few peculiarities of their own. As it is based on LDOS measurements in a very small (usually nanometers-sized) area, it is extremely local, as opposed to conventional ARPES, which gives average electronic structure information integrated over a much larger area (up to millimeters). In addition, QPI distinctly probes the surface state electronic structure, whereas ARPES can sometimes make it difficult to resolve surface and bulk contributions. One of the most powerful advantages of QPI is the ability to measure states above the Fermi level by probing sample states in the positive bias range, which is not possible with conventional ARPES. Therefore, QPI is well suited for low-dimensional systems such as 2-D Van der Waals materials or surface states in metals and topological insulators.

While it has it's advantages, extracting the actual momentum dispersion from QPI measurements can be challenging due to the indirect nature of the information obtained. In QPI, the observed interference patterns correspond to scattering vectors q, which represent differences between initial and final electron momenta ($q = k =_f -k_i$). As a result, the Fourier-transformed data reflect the joint density of states associated with these scattering processes rather than providing direct access to the absolute momentum positions of electronic states. Reconstructing the band structure (energy versus momentum) from QPI data often requires complex analysis and modeling, including assumptions about the scattering mechanisms and the underlying electronic structure. Factors such as multiple scattering events, anisotropic scattering amplitudes, and the presence of impurities can further complicate the interpretation. In contrast, ARPES directly measures the kinetic energy and momentum of photoemitted electrons, offering a more straightforward determination of the electronic dispersion.

The momentum space resolution of the QPI image is inherently limited by the finite size of the image. For a detailed QPI measurement, the image should have a sufficiently large number of pixels, as the discrete Fourier transform results in a momentum space resolution of $\Delta k \propto$ number of pixels, which takes a large amount of time. At this moment, ARPES measurements are much faster and more efficient.

Another difference between the two measurements is that the actual physical phenomenon underlying the two is different. While ARPES is generally understood as a sudden photoexcitation of electrons from the material, QPI involves adiabatic measurements of electrons. This can result in differences due to electron-phonon and electron-hole dynamics observed in the two measurements.

4 - Thermoelectricity in CuRhO$_2$ doped with Mg

4.1 . Introduction

Materials that can efficiently convert thermal energy into electricity and vice versa, i.e. good thermoelectric materials, are desirable for solid-state cooling applications and waste heat conversion to usable energy [83]. Among many classes of materials under consideration for thermoelectric device applications, such as bismuth chalcogenides [139] or lead telluride [71], oxides possess the advantages of thermal stability (which makes them operable at high temperatures), low toxicity, and high oxidation resistance [84].

The thermoelectric performance of a material is characterized by the thermoelectric figure of merit, $ZT = S^2\sigma T/\kappa$, where S is the Seebeck coefficient, σ is the electrical conductivity, T is the temperature, and κ is the thermal conductivity.

A high Seebeck coefficient, along with good electrical conductivity and low thermal conductivity, are therefore critical for potential applications.

However, materials with large carrier concentration, and hence good electrical conductivity, like most metals, usually have a low Seebeck coefficient and large thermal conductivity [15].

Introducing carriers through doping increases both the electrical and electronic thermal conductivity, due to the Wiedemann-Franz law [54]. As a result, this strategy to increase the figure of merit requires efforts to reduce the lattice thermal conductivity.

In particular, the layered oxide CuRhO$_2$ has raised interest as a thermoelectric material [69, 131, 68].

It belongs to the $166 - R\overline{3}m$ space group with the typical delafossite structure, with RhO$_2$ layers stacked between the triangular Cu layers (see fig. 4.3), a semiconducting band gap of 1.9 eV [44], and a high Seebeck coefficient of ~ 200 μV/K at 300 K [68]. Mg substitution of Rh leads to the introduction of hole carriers in the material, resulting in a transition to a metallic state. The Seebeck coefficient decreases systematically with doping in single-crystalline samples, but the 10% Mg-substituted compound CuRh$_{0.9}$Mg$_{0.1}$O$_2$ (CRMO) still exhibits a relatively large Seebeck coefficient of ~ 100 μV/K at 300 K [68].

DFT calculations on this material suggest that the high thermopower has a purely band structure origin. The observed band near the Fermi level is called the "pudding mold" band, which has the peculiar feature of having very different band velocities above and below the Fermi level. In addition to CuRhO$_2$, this "pudding mold" type band has been theoretically investigated in oxides such as Na$_x$CoO$_2$ [70], LaRhO$_3$, and other materials like FeAs$_2$ and PtSe$_2$ [132], among others.

Transition-metal oxides, some of which are both conductive and thermoelectric materials, are in principle good candidates for realizing such "pudding-mold" band structure scenario, thanks to the narrow d-orbitals constituting their conduction band and the natural occurrence of layered structure, which promotes in-plane electrical conductivity and minimizes the out-of-plane thermal conductivity [105].

The correlated nature of the narrow bands [83] can also enhance thermopower. This has been observed in the commensurate charge density wave (CDW) phase in 1T-TaS$_2$ [59]. Strong correlation-induced spin degeneracy has also been proposed as the mechanism behind enhanced thermopower in NaCo$_2$O$_4$ [64].

.

Narrow bands with strong electron correlations typical in d orbitals of transition metals may not be captured well with DFT calculations [6]. Therefore, accessing the experimental electronic structure of thermoelectric transition-metal oxides is essential to disentangle the effects of strong correlations from those of pure band-structural origin, and to verify the mechanism driving the enhanced Seebeck coefficient.

More generally, an experimental demonstration of a "pudding-mold" band in a good thermoelectric material, together with a proof that such band structure is at the origin of the material's large Seebeck coefficient, has been so far missing.

In this study, we investigate the direct observation, through angle-resolved photoemission spectroscopy (ARPES), of a "pudding mold" electronic structure in metallic 10% Mg-doped CuRhO$_2$ (CuRh$_{0.9}$Mg$_{0.1}$O$_2$).

4.2 . The pudding mold band

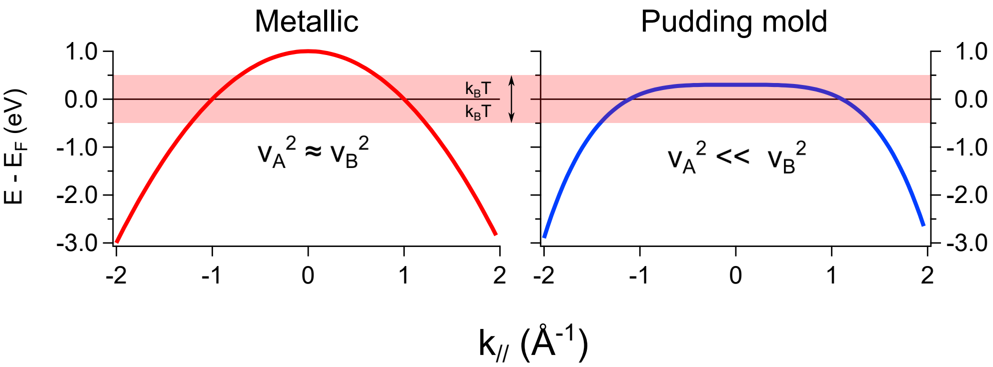

Figure 4.1 – Schematic for a metallic and pudding mold-type band. v$_A$ and v$_B$ represent the band velocities above and below the Fermi level in the highlighted red region of width 2k$_B$T.

According to Boltzmann theory, the Seebeck coefficient is given by the equation [7]

$$\mathbf{S} = \frac{1}{eT}\mathbf{K_1}\mathbf{K_0^{-1}} \tag{4.1}$$

$$\mathbf{K}_n = \sum_{\mathbf{k}} \mathbf{v}(\mathbf{k})\tau(\mathbf{k})\mathbf{v}(\mathbf{k}) \left(-\frac{\partial f(\varepsilon)}{\partial \varepsilon}(\mathbf{k})\right)(\varepsilon(\mathbf{k}) - \mu)^n \tag{4.2}$$

where e (<0) is the electron charge, T is the temperature, $\mathbf{v}(\mathbf{k}) = \nabla_k \varepsilon(\mathbf{k})$ is the group velocity, $\tau(\mathbf{k})$ is the quasiparticle lifetime, $f(\varepsilon)$ is the Fermi-Dirac distribution, and μ is the chemical potential. Now, assuming $\tau(\mathbf{k})$ is independent of $\mathbf{k}$ [110] and considering only the diagonal part of the Seebeck coefficient tensor as S, we can approximately write $K_0 \sim \sum_k' v_B^2 + v_A^2$, where $K_1 \sim k_B T \sum_k' v_B^2 - v_A^2$ and

$$S = \frac{k_B}{e} \frac{\sum_k' v_B^2 - v_A^2}{\sum_k' v_B^2 + v_A^2} \tag{4.3}$$

where k_B is the Boltzmann constant, $\sum_{\mathbf{k}}'$ is the sum over states with $|\varepsilon(\mathbf{k}) - \mu| < k_B T$, and v_A, v_B are the group velocities of states just above and below μ, respectively. Now, as discussed in [70], the presence of a flat band just above (below) μ, which changes to a highly dispersive band below (above) μ (i.e., $v_A^2 \ll v_B^2$ or $v_A^2 \gg v_B^2$), results in a large value of $|S| \sim O(k_B/|e|) \sim O(100)\mu V K^{-1}$ along with low resistivity. This type of band structure is referred to as the "pudding mold" type band (fig. 4.1).

4.3 . Enhanced thermoelectricity from correlations

The Hubbard model is given by the Hamiltonian :

$$H = \sum_{\langle i,j\rangle\sigma} \left(c_{i\sigma}^\dagger c_{j\sigma} + \text{H.C.}\right) + U\sum_i n_{i\uparrow}n_{i\downarrow}, \tag{4.4}$$

where t is the hopping integral between neighboring sites, $c_{i\sigma}^\dagger, c_{i\sigma}$ are the electron creation and annihilation operators at site i and spin $\sigma = (\uparrow, \downarrow)$, U is the onsite Coulomb interaction, and $n_{i\sigma}$ is the occupation of electrons at site i and spin σ.

In the limits of high temperatures and strong correlations, $t, U \ll k_B T$ and $t \ll k_B T \ll U$, eq. 4.1 reduces to

$$\mathbf{S} = -\frac{\mu}{eT}. \tag{4.5}$$

The chemical potential μ can also be expressed as

$$\frac{\mu}{T} = -\left(\frac{\partial s}{\partial N}\right)_{E,V}, \tag{4.6}$$

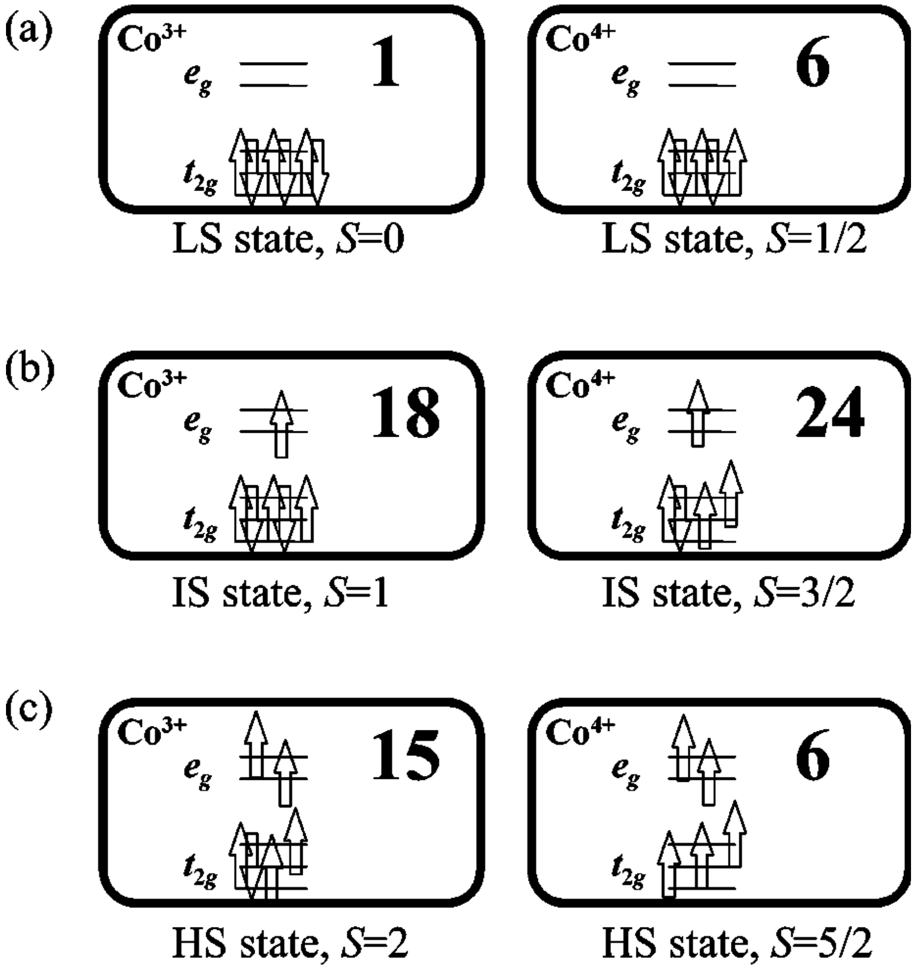
(a)
Co^{3+}
e_g
t_{2g}
1
LS state, S=0
Co^{4+}
e_g
t_{2g}
6
LS state, S=1/2
(b)
Co^{3+}
e_g
t_{2g}
18
IS state, S=1
Co^{4+}
e_g
t_{2g}
24
IS state, S=3/2
(c)
Co^{3+}
e_g
t_{2g}
15
HS state, S=2
Co^{4+}
e_g
t_{2g}
6
HS state, S=5/2

Figure 4.2 – Schematic representation of possible states in Co^{3+} and Co^{4+} ions in the material NaCo$_2$O$_4$. The number in the box represents the total possible degenerate states corresponding to the configuration represented. From [64].

where s is the entropy of the system, N is the number of electrons, E is the internal energy, and V is the volume of the system. In the limit of $T \to \infty$, the entropy can be expressed as $s = k_B \ln g$, where g is the number of possible configurations. Using Eq. 4.5, we get

$$\frac{\mu}{k_B T} = -\left(\frac{\partial \ln g}{\partial N}\right)_{E,V} \tag{4.7}$$

and the Seebeck coefficient is

$$S = -\frac{k_B}{e}\frac{\partial \ln g}{\partial N}. \tag{4.8}$$

Therefore, in the high T limit, $S \propto \partial \ln g$, i.e., the total number of possible configurations of the system. This implies that orbital and spin degenerate systems enhance the Seebeck coefficient (see fig. 4.2).

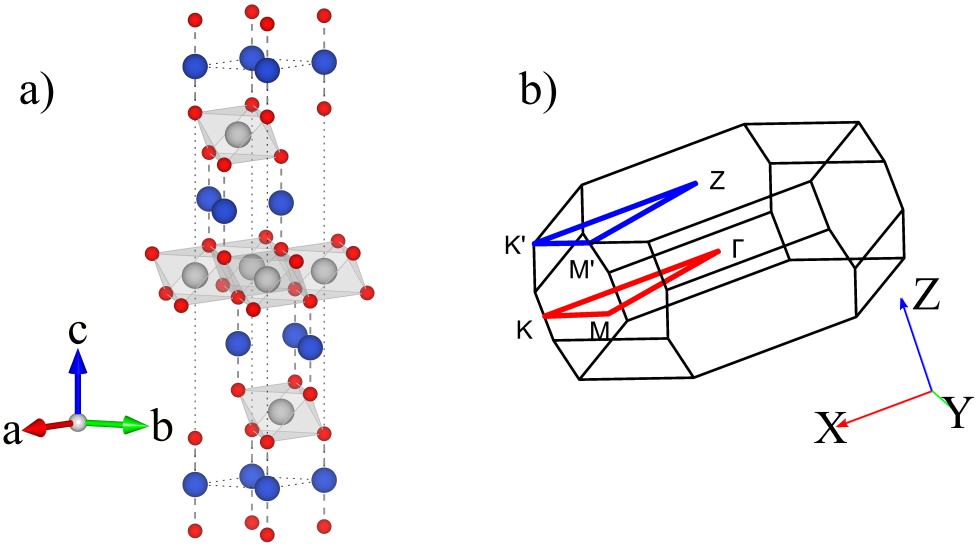

Figure 4.3 – a) Conventional hexagonal unit cell of CuRhO$_2$. Red, blue and grey atoms represent O, Cu and Rh respectively. b) Primitive Brillouin zone of CuRhO$_2$. High symmetry points and the path connecting them are indicated.

4.4 . Measurements and Observations

ARPES measurements were performed using synchrotron radiation at the BL2-A (Mushashi) beamline in Photon Factory, KEK. The electron analyzer in the setup was a Scienta-Omicron SES-2002 with horizontal slits. Soft x-rays (SX) in p-polarization with energies in the range of 500-620 eV and vacuum ultra-violet (VUV) radiation of 182 eV in p-polarization were used. The CuRh$_{0.9}$Mg$_{0.1}$O$_2$ samples were cleaved along $[001]$ and measured in UHV conditions with pressure maintained around 5×10^{-11} mbar at a temperature of 20 K. The Fermi level was set by fitting a Fermi function convoluted with a linear function to the momentum integrated energy slices of the energy-momentum measurements.

As shown in fig. 4.4 a, the Fermi surface of CRMO at the K-M-Γ plane is composed of six symmetrical triangular hole-like pockets centered around the hexagonal Brillouin-zone vertices, increasing in size as one goes higher in binding energy—figs. 4.4 b-d.

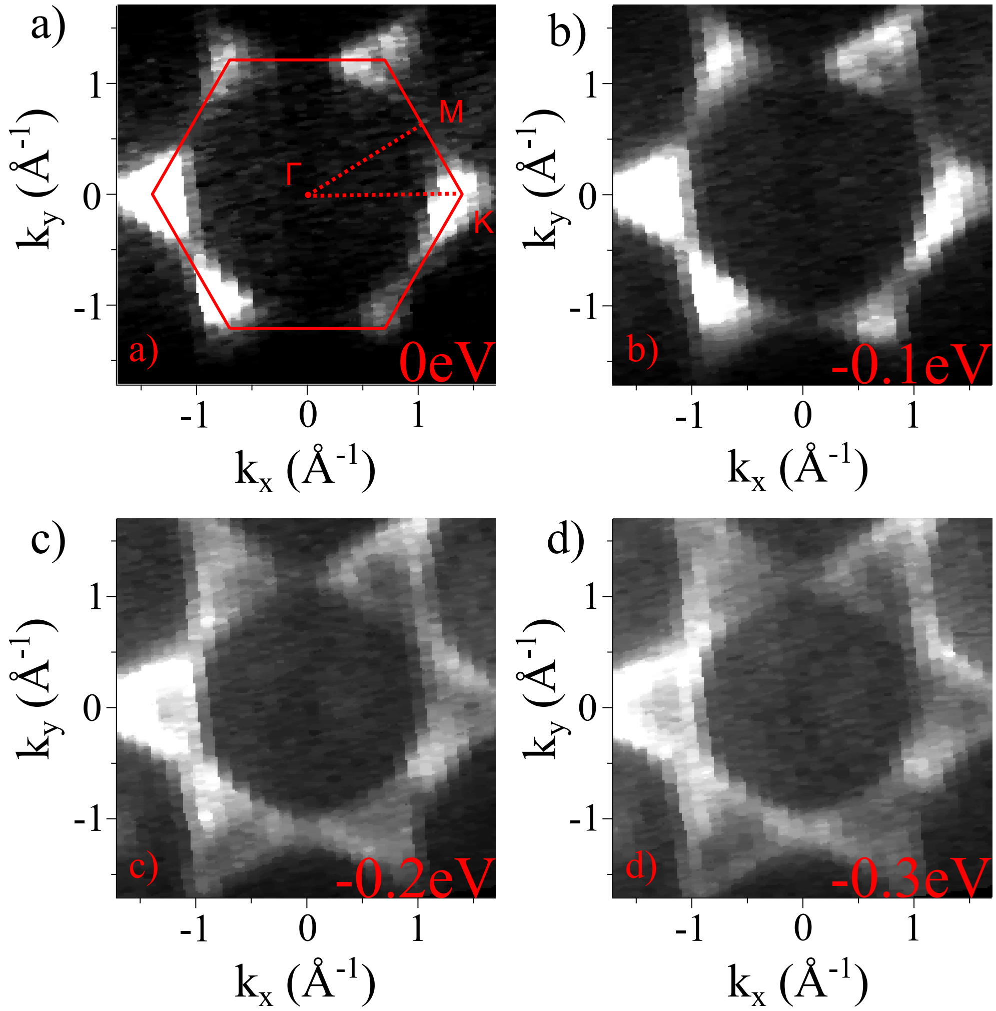

Figure 4.4 – Constant energy maps at a) 0eV, b) -0.1eV, c) -0.3eV, and d)-0.4eV relative to Fermi level. Data was taken at s-polarization and 182 eV photon energy. The Brillouin zone is overlaid in red in a.

Figs. 4.5 a, b show the second derivatives along the energy-axis for the ARPES dispersion along the high-symmetry paths K-M-Γ-K taken at 542 eV and K'-M'-Z-K' taken at 590 eV, respectively, overlaid with the corresponding DFT calculations.

Fig. 4.5 c shows the out-of-plane Fermi surface map, spanning the Γ11 and Z11 high-symmetry points in the reciprocal space. The corresponding ARPES energy-momentum dispersion along k_z (momenta along the out-of-plane z direction), shown in fig. 4.5 d, reveals a cosine-like band dispersion with an electron-like minimum around $k_z = \Gamma$ and a hole-like maximum at $k_z =$ Z.

The experimental bandwidth along k_z is smaller than the calculated one by a factor ~ 0.65. This can be due to the unaccounted correlations of the Rh

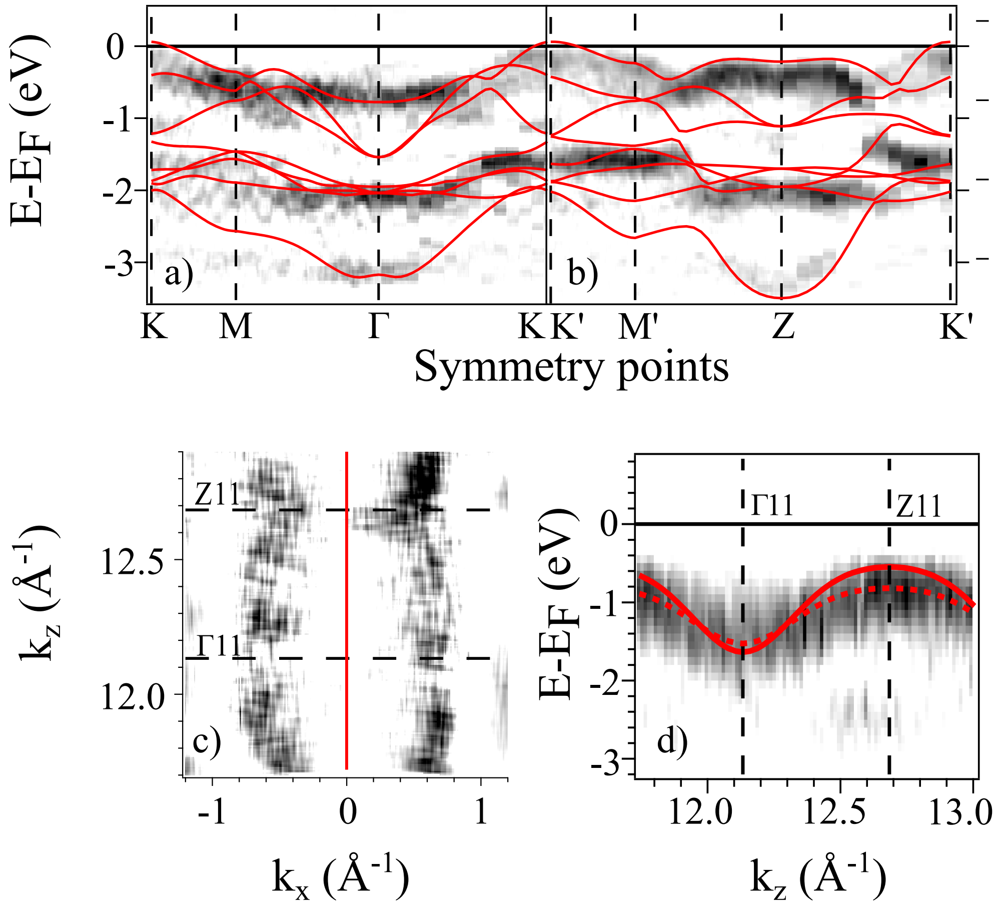

Figure 4.5 – a) In-plane band cut at 542 eV photon energy overlaid with calculated bands at $k_z = \Gamma$ in red. b) In-plane band cut at 590 eV photon energy overlaid with calculated bands at $k_z = Z$ in red. c) Out of plane Fermi surface along $k_z - k_x$ axis, spanning the Γ11 (538 eV photon energy) and Z11 (590 eV photon energy) high symmetry points. The black dotted lines are positions of high symmetry points along k_z. d) Second derivative along energy of the energy-momentum dispersion along k_z at normal emission. Solid red lines are the calculated bands and dotted red lines is the experimental fit. In panels c and d, the data was obtained using photons in the range of $500 - 620$eV. Γ11 is calculated to lie at 538 eV by fitting with the k_z measurement and using an inner potential 3.15 of 23.5 eV in the three step model approximation [49].

t$_2$g orbitals in the calculations.This discrepancy in band dispersion along k_z is also seen in the in-plane dispersion at $k_z = Z$, where the band around Z is shifted by about -0.2 eV compared to the calculations. Overall, the momentum dispersion is captured well in the DFT calculations. However, there are small shifts in energy, particularly for the Cu d orbitals around -2 eV binding energy. At $k_z = \Gamma$, these Cu d orbitals are shifted by +0.15 eV, and at $k_z = Z$, the shift is around +0.25 eV in the calculations compared to the data.

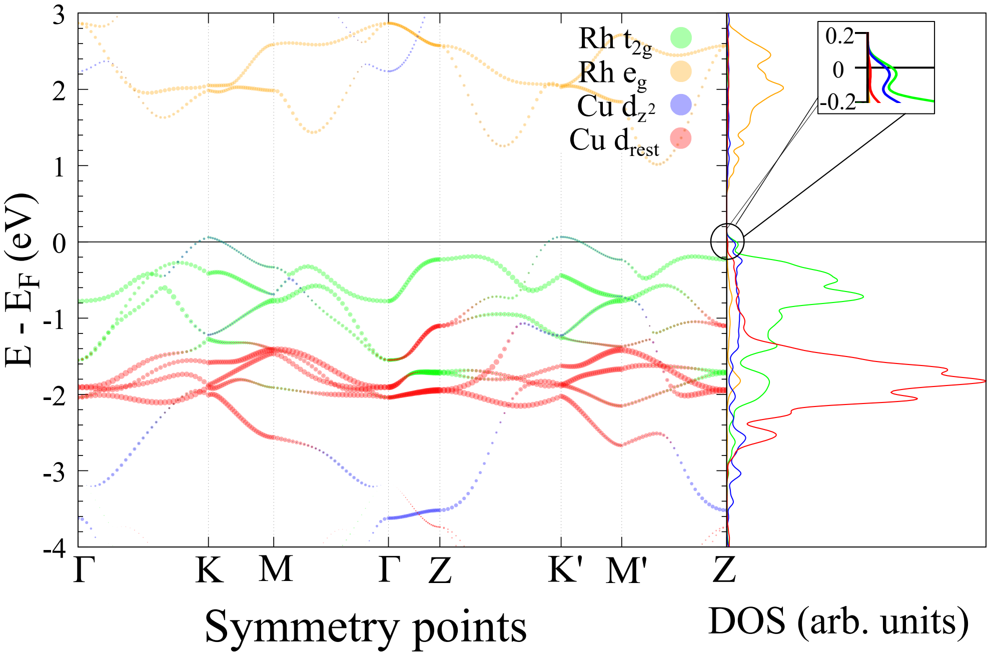

Figure 4.6 – Left : Orbital project bands of CRMO (with the Fermi level set shifted to -0.06 eV from the top of the valence band) with orbital weights indicated by the size of colored circles. Right : Orbital project density of states (DOS). Inlaid : Closer view of the DOS near the Fermi level which shows that the density of Rh t_{2g} orbitals and Cu d_{z^2} orbitals is similar at the Fermi level.

As shown in Figure 4.6, the calculated band gap is $\sim$ 0.8 eV before the rigid shift of the Fermi level by -0.06 eV, which is smaller than the experimental value. This is due to the well-known underestimation of the insulating band gap by DFT [97]. The calculations reveal that the top of CRMO's conduction band around K and K' momenta has the orbital character of Cu d_{z^2} hybridized with the Rh t_{2g} orbitals, the d_{xz}, and the d_{yz}, with most of the weight of the d_{xy} band lying around the Γ point.

From the calculated bands, the in-plane group velocities near K, i.e., the top of the conduction band, are $v_A = 0.57$ eVÅ and $v_B = 1.00$ eVÅ , while the group velocities near K' are $v_A = 0.49$ eVÅ and $v_B = 1.36$ eVÅ within an energy window of $k_B T \sim 1000$ K around the Fermi level.

Assuming that the Seebeck coefficient in CRMO comes essentially from electronic states around K', and using the above values of group velocities above and below E_F around K', one obtains from eq. 4.3, an estimated value of $S \sim 66\mu$V/K, which is of the same order as the experimental value of $\sim 100\mu$V/K in CRMO measured at 300K [68].

Thus, we see the enhancement of the Seebeck coefficient in the $k_z = Z$ plane, due to the 'pudding mold' band around K', with a larger difference in v_A and v_B.

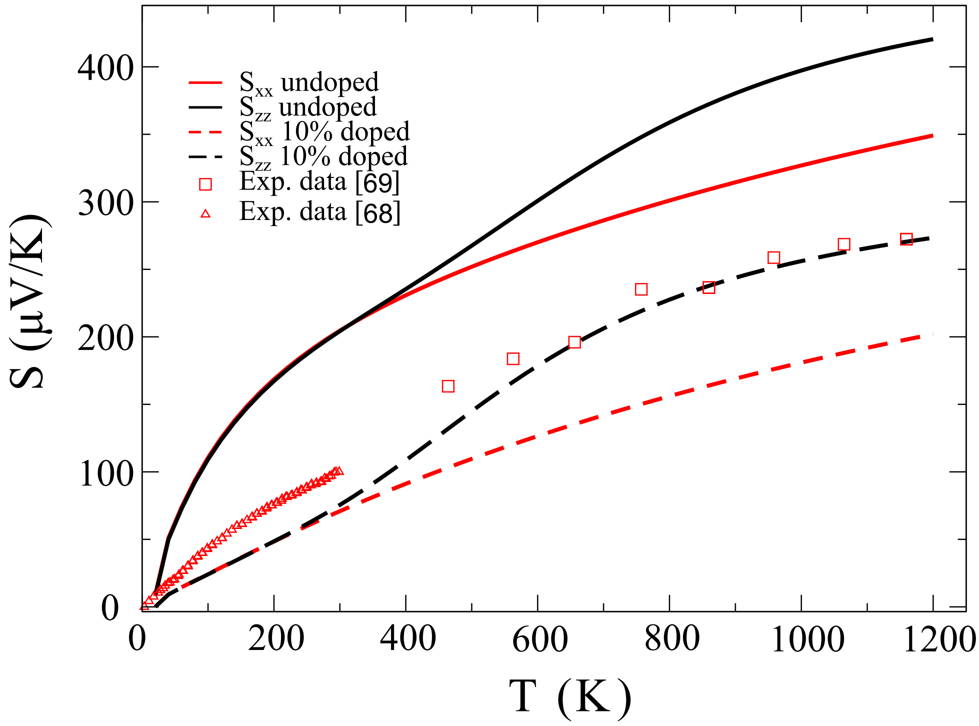

Figure 4.7 – The S$_{xx}$ and S$_{zz}$ components of the calculated Seebeck coefficient S vs temperature T for the undoped sample and the 10% doped sample. Experimental data from [69] and [68] are compared to the calculations of doped Seebeck coefficient.

Figure 4.7 shows that the calculated Seebeck coefficient agrees well with the experimental data, with the non-doped CuRhO$_2$ having a Seebeck coefficient of $\sim 200\mu$V/K at 300 K, and the 10% doped sample CuRh$_{0.9}$Mg$_{0.1}$O$_2$ having a Seebeck coefficient of $\sim 70\mu$V/K at 300 K [116], but is slightly smaller than the values measure by [68]. Furthermore, the comparisons between the in-plane (S$_{xx}$) and out-of-plane (S$_{zz}$) Seebeck coefficient show that above 300 K, the in-plane component does not increase while the out-of-plane component keeps on increasing till 1000 K. This is ascribed to the flat dispersion in the K-K' direction along the out-of-plane momentum direction. The high value of S$_{zz}$, $\sim 256\mu$V/K at 1000 K for the doped sample, is very close to the experimental value of $\sim 260\mu$V/K in ref. [69] where measurement was done on a polycrystalline doped samples.

4.5 . Conclusion and future outlook

In conclusion, our observation of a flat band in CRMO fits well with the calculated band structure and it's description in terms of the “pudding mold” band model without any ambiguity.

Our work provides an experimental basis for the realization of materials with large Seebeck coefficients originating from the flat 'pudding-mold' type band. This process of material discovery can now be accelerated by machine learning tools [146] and computational databases like "The Materials Project" [52].

In this study, we have not focused on magnetism and its effect on thermoelectricity. However, as discussed in [79], magnon drag and increased spin entropy might enhance the thermopower in magnetic materials, as reported in NaCoO_2 [134], CuCr_2S_4 [57], CaFe_4S$b_1 2$ [109], and EuMnSb_2 [123]. An intersection of the flat band and magnetism might be another ripe area for exploration and investigation in thermoelectric materials.

4.6 . Appendix

4.6.1 . DFT calculations

DFT calculations of the undoped system were performed using the *QUANTUM ESPRESSO* [36] code with a plane-wave basis, using a polarized general gradient approximation (GGA) exchange-correlation functional of Perdew-Burke-Ernzerhof (PBE) from the Standard solid-state pseudopotentials (SSSP) efficiency library [101, 75]. The plane wave kinetic energy cutoff is set to 55 Ry and the charge density kinetic energy cutoff is 440 Ry. The lattice parameters used for the calculations were $a = 3.068$ Å and $c = 17.09$ Å with respect to the conventional hexagonal lattice. The parameter a is about 0.2% smaller than the value cited in ref. [13] to account for the reduction in the average radius at the Rh site due to the Mg doping, as described in ref. [68].

The parameter c is the same as the one for the undoped material. The unit cell was then relaxed by allowing the atoms to move, but constraining the unit cell dimensions.

TThe calculated DFT band structure was then matched with the one measured in the doped compound by applying a rigid band shift of -0.06 eV from the top of the valence band of the calculated bands of the undoped material.

4.6.2 . Thermopower calculation with BoltzTrap

From Boltzmann theory, the electric current j, in terms of conductivity tensors σ, can be written as

$$j_i = \sigma_{ij} E_j + \sigma_{ijk} E_j B_k + \nu_{ij} \nabla_j T + \cdots \tag{4.9}$$

where E, B and ∇T are the electric field, the magnetic field and the thermal gradient.

The energy-projected conductivity can be defined as,

$$\sigma_{\alpha\beta}(\varepsilon) = \frac{1}{N}\sum_{i,\mathbf{k}} \sigma_{\alpha\beta}(i,\mathbf{k})\frac{\delta\left(\varepsilon - \varepsilon_{i,\mathbf{k}}\right)}{d\varepsilon}. \tag{4.10}$$

We input DFT band energy values to BoltzTrap [82], which then expands them in terms of its Fourier components using so-called star functions $\mathbf{R}(\mathbf{k})$, which preserve the crystal symmetry,

$$\tilde{\varepsilon}_i(\mathbf{k}) = \sum_{\mathbf{R}} c_{\mathbf{R}i} S_{\mathbf{R}}(\mathbf{k}), \quad S_{\mathbf{R}}(\mathbf{k}) = \frac{1}{n}\sum_{\{\Lambda\}} e^{i\mathbf{k}\cdot\Lambda\mathbf{R}} \tag{4.11}$$

where R is a direct lattice vector, $\{\Lambda\}$ are the n point-group rotations. More details regarding this Fourier expansion can be found at [82].

Subsequently, the necessary derivatives of 4.10 can be calculated using fast Fourier transforms (FFTs) [24], which are then finally used to calculate the Seebeck coefficient S

$$S_{ij} = E_i\left(\nabla_j T\right)^{-1} = \left(\sigma^{-1}\right)_{\alpha i} v_{\alpha j}. \tag{4.12}$$

5 - Metal-Insulator Transition in $CaVO_3$

5.1 . Introduction

Metal-insulator transitions (MITs) are a hallmark of strong electronic correlations. In contrast to conventional metals and insulators, whose properties are understood based on the partial or complete filling of the highest occupied band and can be explained by the weakly interacting electron framework of Fermi liquid theory, materials that have a partially occupied conduction band but behave as insulators cannot be explained by weak electron interaction theory.

Initially observed in many transition metal oxides with partially occupied d-orbitals, such as NiO, Rudolf Peierls [72] pointed out the possible role of strong electron-electron repulsion, which may favor electron localization.

Fast forward to the present, and strong correlations originating from the narrow d-orbitals in transition metal compounds have been observed in a wide array of interesting phenomena, including high-Tc superconductors [73], non-Fermi liquid metals [122], and MITs [50].

In particular, MITs are still far from being fully understood. What makes them especially difficult to study is that, depending on the system, the MIT can be triggered by a variety of external parameters such as temperature, doping, electric fields, and strain, which can induce changes in structural, magnetic, or orbital characteristics. Consider the case of vanadium oxides VO_2 and V_2O_3, which are considered prototypical systems for observing MIT in strongly correlated materials. There have been decades of experimental and theoretical work on these materials, which have been the subject of numerous debates regarding the mechanisms driving the MIT. The current consensus on the MIT differs significantly between VO_2 and V_2O_3. The MIT in VO_2 is now thought to be driven by the dimerization of V atoms along the c-axis and occurs between a high-temperature (HT) paramagnetic metallic rutile phase and a low-temperature (LT) insulating monoclinic phase at 340 K [90, 41, 115]. However, in V_2O_3, the MIT occurs between a high-temperature paramagnetic corundum phase and a low-temperature antiferromagnetic monoclinic phase, and the driving force behind the MIT is still under intense study [20, 81, 125, 76].

The ability of resistive switching by several orders of magnitude, which depends sensitively on external parameters, has shown promise for enabling the creation of new devices. These devices, based on transistors with fast and efficient switching driven by strong correlations, form the basis of "Mottronics" [78]. These Mottronic devices can be exploited in the emerging field of neuromorphic computing [103], where devices are modeled after neurons that respond to external stimuli.

Motivated by the pursuit of materials for these applications, we turn toward thin films of strongly correlated materials. One such material of interest is $CaVO_3$, another vanadate in the family of correlated vanadates. $CaVO_3$ is metallic in bulk and thick films but undergoes a strong MIT for film thicknesses below 20 unit cells (u.c.) [148, 147, 86]. This behavior is shared by other transition metal oxides like $SrVO_3$, $LaNiO_3$, and $SrIrO_3$ [145, 38, 80]. However, the MIT cannot be accounted for by dimensional crossover in thin films, as suggested for MIT in ultrathin $SrVO_3$ [145]. This MIT in $CaVO_3$ appears to be mediated in a complex way by epitaxial strain, surface crystal field splitting, and possible structural and magnetic transitions. Our goal is to characterize the electronic structure of this MIT through ARPES and gain insights into the mechanisms driving this phenomenon.

5.2 . Crystal structure

$CaVO_3$ belongs to the perovskite family of compounds with the typical chemical configuration $A^{+2}B^{+4}O_3^{-2}$. The bulk crystal structure is orthorhombic, belonging to the $Pnma$ space group, with octahedral tilting (rotation around the in-plane axis, denoted as ϕ) and rotation (around the out-of-plane axis, denoted as θ) [see fig. 5.1]. These octahedral distortions cause a doubling of the unit cell along the c-axis and an enlargement of the in-plane unit cell with $\sqrt{2} \times \sqrt{2}$ lattice vectors. The unit cell parameters are a = 5.32 Å, b = 5.34 Å, and c = 7.55 Å. The nearest-neighbor V-V distance is $\approx$ 3.77 Å in the orthogonal directions.

5.3 . Electronic structure

In $CaVO_3$, the vanadium atoms exhibit an oxidation state of +4, with a d^1 occupation of the 3d orbitals. The V-O octahedral crystal field results in the splitting of the 3d levels of V into lower-energy t_{2g} states, consisting of the d_{xy}, d_{xz}, and d_{yz} orbitals, and higher-energy e_g states consisting of the $d_{x^2-y^2}$ and d_{z^2} orbitals. The d^1 electron occupies the t_{2g} orbitals, resulting in a nominally metallic system.

5.3.1 . DFT calculations

Theoretical calculations of the bulk band structure of $CaVO_3$ were performed using DFT within the Quantum Espresso software [36]. We used a plane wave basis with a generalized gradient approximation (GGA) exchange-correlation functional of Perdew-Burke-Ernzerhof (PBE) from the Standard Solid-State Pseudopotentials (SSSP) efficiency library [101].

In the case of a perfect perovskite crystal like $SrVO_3$, the Fermi surface in the k_x-k_y plane is composed of the three t_{2g} bands : a circular structure

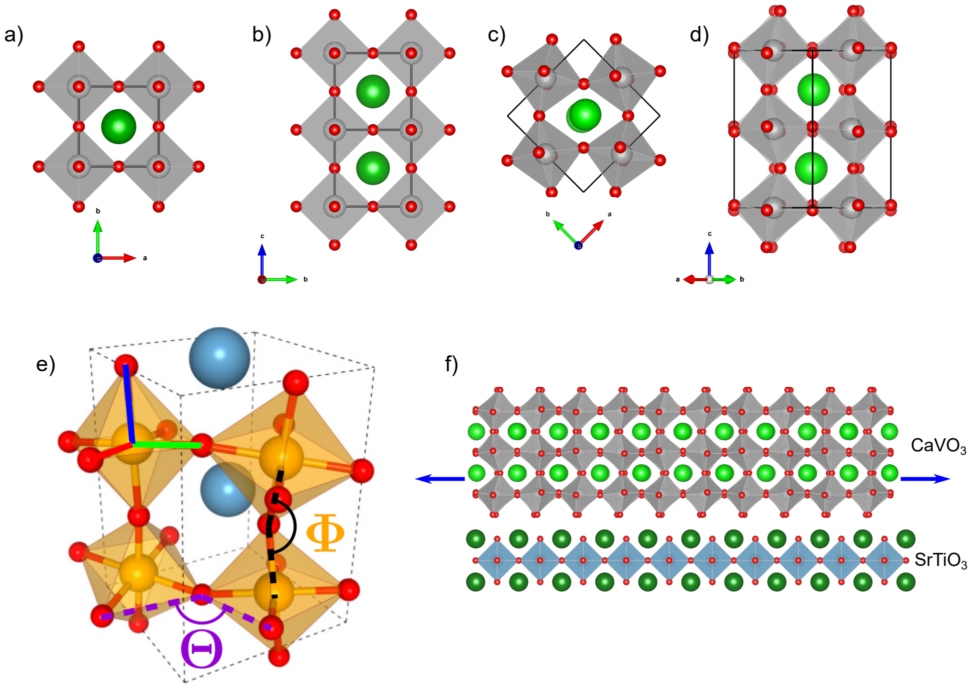

Figure 5.1 – Crystal lattice for a perfect perovskite structure along the a) in-plane and b) out-of-plane directions. Crystal lattice for CaVO$_3$ along the c) in-plane and d) out-of-plane directions. The unit cell is represented by black lines. Green, silver, and red spheres represent Ca, V, and O, respectively. The V-O octahedra are represented by the silver polygons. e) Θ and Φ represent O-O-O and V-O-V angles used to characterize tilts. Adapted from [11]. f) Schematic showing tensile strain direction due to lattice mismatch between SrTiO$_3$ and CaVO$_3$.

originating from the d$_{xy}$ orbital, and a pair of orthogonal lines arising from the d$_{xz}$ and d$_{yz}$ orbitals, which disperse only along the k$_x$ and k$_y$ directions, respectively (see fig. 5.2).

Substituting Ca for Sr in the perovskite structure leads to distortions due to the smaller ionic radius of Ca compared to Sr. These V-O octahedral distortions are characterized by an $a^-a^-c^+$ tilt system in Glazer notation [37]. To account for these distortions, a new periodicity is introduced, with the unit cell enlarged to a $\sqrt{2} \times \sqrt{2} \times 2$ supercell containing 20 atoms, compared to just 5 atoms in the ideal perovskite structure (see fig. 5.1).

The DFT band structure for CaVO$_3$ is qualitatively similar to that of SrVO$_3$ (see fig. 5.2), but with additional bands due to Brillouin zone (BZ) folding. The calculations reveal that the three t$_{2g}$ orbitals form the conduction band and are nearly degenerate, with slight energy differences due to octahedral distortions. The band bottom of these parabolic conduction bands lies 0.94 eV below the Fermi level.

To achieve a better match with the ARPES spectral function, a band-unfolding procedure [95] was used to unfold the bands back to the nominal perovskite $1 \times 1 \times 1$ unit cell. Fig. 5.2 f, g shows the unfolded bands along the $k_{<100>}$ and $k_{<001>}$ directions of the base $1 \times 1 \times 1$ unit cell. Compared to the band dispersion of SrVO$_3$, the CaVO$_3$ bands are qualitatively very similar, and the intensity of the additional bands from folding is relatively weak. For this reason, we adopt the convention of using the orthogonal axes $k_{<100>}$, $k_{<010>}$, and $k_{<001>}$, which follow the BZ of the $1 \times 1 \times 1$ periodicity, rather than the conventional periodicity of the CaVO$_3$ BZ.

5.4 . ARPES measurements

ARPES measurements were performed on CaVO$_3$ [001] crystals grown on a SrTiO$_3$ [001] substrate. The SrTiO$_3$ substrate and the CaVO$_3$ lattice have a mismatch in lattice constants (3.9 Å for SrTiO$_3$ [4], 3.77 Å for CaVO$_3$ [94], see fig. 5.1 f). Samples with thicknesses of 90 u.c., 45 u.c., and 15 u.c. were measured at the BL2A beamline at Photon Factory, KEK, Japan, while the 30 u.c. and 20 u.c. thick samples were measured at the CASSIOPEE beamline at SOLEIL, France. All measurements were conducted at a sample temperature of approximately 15 K. The following section summarizes the experimental observations for the measured samples.

5.4.1 . 90 u.c.

The thickest 90 u.c. (≈ 34 nm) crystals are assumed to represent the baseline bulk electronic structure of CaVO$_3$. At this thickness, any interfacial strain between the substrate and the grown CaVO$_3$ crystal is considered negligible.

Fig. 5.3 shows the Fermi surface along the $k_{<001>}$-$k_{<100>}$ plane, as well as the band dispersion along the $k_{<001>}$ direction. Photon energies ($h\nu$) ranging from 45 eV to 110 eV were used to map the electronic structure along the $k_{<001>}$ direction. An inner potential (eq. 3.15) of 7 eV was used to match the observed energy at Γ of 88 eV with the expected energy of Γ_{006}, based on the crystal lattice c-axis length of 7.55 Å.

The band cut along the $k_{<001>}$ direction reveals a parabolic band centered around $k_{<001>}$ = 4.99 Å^{-1}, along with a weakly intense parabolic band around $k_{<001>}$ = 4.14 Å^{-1}, which corresponds to the location of Γ_{005}. The location of Γ_{005} corresponds to the Z point in the $1 \times 1 \times 1$ unit cell. As a result, the spectral intensity around this point is suppressed due to the structural factor contribution to the matrix elements (eq. 3.8), and matches well with the unfolded band calculations (see fig. 5.2 g).

The $k_{<100>}$ - $k_{<010>}$ Fermi surface was measured at $h\nu = 82$ eV, which corresponds to $k_{<001>} = \Gamma_{<006>} - 0.16$ Å^{-1} (see fig. 5.4). An intense elliptical Fermi contour is observed, with strong dispersion along $k_{<100>}$. This is attributed to the V d_{xy} orbitals, which disperse along both $k_{<100>}$ and $k_{<010>}$ directions. The Fermi momentum, k_F, is estimated to be ≈ 0.48 Å^{-1} along $k_{<100>}$, and the band width is ≈ 0.38 eV below the Fermi level. This indicates significant renormalization of the bands, with a mass enhancement factor $Z \approx 0.9/0.4 = 2.25$. This is close to the value of ~ 2 observed in SrVO$_3$ [144]. A cut along $k_{<100>}$ passing through $k_{<010>} = 0$ Å^{-1} reveals the presence of a flat, broad, non-dispersing band at -0.34 eV, which is attributed to d_{yz} orbitals.

It is noteworthy that there is an asymmetry in the in-plane Fermi momenta of the d_{xy} bands along the $k_{<100>}$ and $k_{<010>}$ directions, measuring 0.48 Å^{-1} and 0.40 Å^{-1}, respectively. While the bulk lattice parameters are asymmetric in the x and y directions, this asymmetry is at most $\sim 1\%$; however, the asymmetry in the Fermi momenta here is $\sim 17\%$. The estimated BZ from the observed Fermi surface has a length of 1.93 Å^{-1} along $k_{<100>}$ and 1.63 Å^{-1} along $k_{<010>}$, corresponding to in-plane lattice vectors of 3.85 Å and 3.24 Å along the x and y directions, respectively. The origin of this large asymmetry is not entirely clear, as the substrate should not be causing significant strain at such film thicknesses. A possible explanation could be the formation of oxygen vacancies [135] during annealing, which may distort the surface of the film, or it could be an artifact of imperfect film growth, or signatures of a structural transition.

5.4.2 . 45 u.c.

The 45 u.c. (≈ 17 nm) thick film at 82 eV (see fig. 5.4 d) is qualitatively similar to the 90 u.c. thick film. The Fermi momentum, k_F, is estimated to be ≈ 0.46 Å^{-1} along $k_{<100>}$ and 0.38 Å^{-1} along $k_{<010>}$, with a band width of 0.38 eV below the Fermi level, similar to the 90 u.c. thick film. The dispersion along $k_{<100>}$ passing through $k_{<010>} = 0$ Å^{-1} shows that the non-dispersing d_{yz} bands lie at an energy of -0.32 eV below the Fermi level.

The flat band now appears much sharper compared to the 90 u.c. sample, indicating that the dispersion is taken at an energy close to the bulk Γ. This difference in dispersion could be an effect of excessive annealing of the 45 u.c. sample compared to the 90 u.c. sample. The 45 u.c. sample was subject to additional annealing due to problems with sample preparation. This extra annealing could have resulted in excessive oxygen vacancies and relaxation of the lattice constant along the z-direction, leading to a change in bulk Γ photon energy.

5.4.3 . 30 u.c.

The Fermi surface of the 30 u.c. (≈ 11.3 nm) thick film, taken at 82 eV, is shown in fig. 5.5 a. The most prominent difference in the Fermi surface, compared to previous samples, is the reduction in anisotropy along the $k_{<100>}$ and $k_{<010>}$ directions for the d_{xy} band, with $k_F \approx 0.39$ Å^{-1} along $k_{<100>}$ and

$k_F \approx 0.38$ Å^{-1} along $k_{<010>}$. This reduction in anisotropy might be attributed to the effects of strong epitaxial tensile strain from the SrTiO$_3$ substrate, which has an isotropic in-plane lattice structure.

If the sample is rotated by 45°, as shown in fig. 5.5 c, the edges of the second BZ become visible, which are then used to determine the approximate lattice constants. We estimate the lattice constants $b \approx 1.59$ Å^{-1} and $a \approx 3.94$ Å, where b and a are the momentum space and real space lattice constants, respectively. The estimated lattice constant value of 3.94 Å matches closely with the lattice constant value of SrTiO$_3$, $a = 3.9$ Å [4]. This indicates that the 30 u.c. thick sample is already experiencing close to the maximum epitaxial strain from the SrTiO$_3$ substrate.

The cut along $k_{<100>}$ passing through $k_{<010>} = 0$ Å^{-1} (see fig. 5.6 d) reveals a strong broadening of band features below -0.22 eV. There is also a lack of a clear signature of the flat d_{yz} band. We believe that this strong broadening of the spectral function is due to changes in the d_{yz} band, caused by variations in the c-axis length. A change in the c-axis can cause variations in the spectral intensity of the folded bands along $k_{<001>}$. Another reason could be that we are moving further away from the bulk Γ photon energies, causing the spectral function of the d_{yz} band to broaden away from Γ. As the in-plane lattice constants expand due to the epitaxial strain from the substrate, there is an accompanying reduction in the out-of-plane lattice constant. If the dispersion is measured at the same photon energy for the thinner samples, it may move away from the actual dispersion at bulk Γ. To illustrate this point, consider that at 82 eV, we are approximately 20% of the BZ lattice constant away from the bulk Γ along $k_{<001>}$ with a c-axis length of 7.55 Å. If the c-axis length is reduced to 7.35 Å, we are now 35% of the BZ lattice constant away from Γ. Fig. 5.6 g,h shows the dispersion along bulk Γ and 0.35 BZ unit cells away from bulk Γ for the 90 u.c. sample. There is clear broadening of spectral features in the region of the d_{yz} band for the dispersion away from Γ.

5.4.4 . 20 u.c.

The Fermi surface of the 20 u.c. (≈ 7.5 nm) thick film is shown in fig. 5.5c. The spectral function looks qualitatively very similar to that of the 30 u.c. sample. The Fermi momenta are $k_F \approx 0.39$ Å^{-1} along $k_{<100>}$ and $k_F \approx 0.385$ Å^{-1} along $k_{<010>}$, respectively. The most distinct feature of the 20 u.c. sample compared to the 30 u.c. sample is the increased broadening of band dispersion along momentum, with even stronger broadening of bands below -0.24 eV compared to the 30 u.c. sample (see fig. 5.6 b, c, e, f).

5.4.5 . Bandwidth changes across metallic samples

To track changes in the dispersion of the d_{xy} band across the measured metallic samples, peak positions from the MDC cuts along $k_{<100>}$ passing through $k_{<010>} = 0$ were extracted by fitting the MDCs with Lorentzian peaks for all the samples. Since the d_{xy} band disperses only in the in-plane direction, changes in the out-of-plane lattice constant across the samples should have minimal effects on the dispersion, and the band should be sensitive only to changes in the in-plane lattice caused by epitaxial strain. The peak positions were fitted to a line (see fig. 5.7), and the extracted Fermi velocities (v_F) are tabulated in table 5.1.

	90 u.c.	**45 u.c.**	**30 u.c.**	**20 u.c.**
$\|\mathbf{v}_F\|$ (eVÅ)	3.12 ± 0.97	2.66 ± 0.71	1.51 ± 0.23	1.47 ± 0.22

Table 5.1 – Extracted absolute values of v_F from linear fits in the range of 0.14 eV below E_F

We observe a consistent decrease in v_F going from thicker to thinner samples, which indicates a corresponding decrease in the bandwidth of the d_{xy} band. This observation is consistent with prior experimental and theoretical studies [86]. Qualitatively, we observe that the d_{xy} orbital dominates the intensity near the Fermi level. However, the presence of the d_{xz} band, which also contributes to the dispersion along $k_{<100>}$, might confound the results, presenting a limitation to the above analysis.

5.4.6 . 15 u.c.

The electronic structure at 15 u.c. ($\approx$ 5.6 nm) changes critically from metallic to insulating. There is no longer a sharp Fermi level; instead, a flat band appears at -0.86 eV with a bandwidth of $\approx$ 1.3 eV. The Hubbard band, which increases in relative intensity compared to the dispersing bands at the Fermi level from the 90 u.c. to the 45 u.c. sample, completely disappears in the 15 u.c. sample, being replaced by the flat band (see fig. 5.8 a). This is consistent with the expected Mott-Hubbard transition as the strength of electron-electron correlation increases.

5.4.7 . Core level XPS

Core-level spectra for the 90 u.c., 45 u.c., and 15 u.c. samples were measured in the binding energy (BE) range of 505 eV to 540 eV to track changes in the O 1s and V 2p peaks as a function of sample thickness (see fig. 5.9 a, b, c, d). For the conducting samples (90 u.c., 45 u.c.), the Fermi level was used to fix the BE. For the insulating 15 u.c. sample, the BE of the Ca 2s peak at 438.54 eV, measured in the 90 u.c. sample, was used as the reference. The contributions of the V^{3+}, V^{4+}, and V^{5+} states to the V $2p_{3/2}$ peak and the positions of O 1s and its satellite were extracted by fitting to a Voigt function [58] and are summarized in table 5.2.

A closer look at the V $2p_{3/2}$ states reveals the emergence of localized V^{3+}

Sample	Core line	BE (eV)	FWHM (eV)
90 u.c.	V^{3+} 2p$_{3/2}$	514.60	1.26
	V^{4+} 2p$_{3/2}$	515.62	3.25
	V^{5+} 2p$_{3/2}$	517.61	2.39
	O 1s	529.33	0.75
	O 1s sat.	530.25	2.03
45 u.c.	V^{3+} 2p$_{3/2}$	514.85	2.42
	V^{4+} 2p$_{3/2}$	516.43	1.77
	V^{5+} 2p$_{3/2}$	517.72	2.36
	O 1s	529.34	0.79
	O 1s sat.	530.38	2.02
15 u.c.	V^{3+} 2p$_{3/2}$	514.54	1.72
	V^{4+} 2p$_{3/2}$	515.50	2.13
	V^{5+} 2p$_{3/2}$	516.41	2.73
	O 1s	529.83	1.02
	O 1s sat.	not significant	-

Table 5.2 – XPS fit parameters for V 2p and O 1s peaks for the 90 u.c, 45 u.c. and 15 u.c. samples

states at a BE of $\approx$ 514.6–514.8 eV. These states increase in intensity, accompanied by a decrease in the intensity of V^{5+} and V^{4+} peaks, from the 90 u.c. to the 45 u.c. sample. In the 15 u.c. sample, a dominant V^{3+} peak at 514.54 eV emerges, accompanied by a shift of the O 1s main peak from 529.35 eV to 530.83 eV BE, going from the 90 u.c. to the 15 u.c. sample.

The presence of a large O 1s satellite is attributed to the O–V hybridization difference between V^{3+} and V^{4+} oxidation states. The higher BE peak is associated with weaker covalency between V^{3+} and O, as the V^{3+} states have higher electron density on V sites and are, hence, more localized in nature. The lower BE peak is due to V^{4+}–O hybridization, where V^{4+} is the expected oxidation state in bulk CaVO$_3$.

5.5 . Discussion

We observe a sharp transition to an insulating state for the 15 u.c. sample, consistent with previous observations [86]. The significant epitaxial strain caused by the lattice mismatch between the SrTiO$_3$ substrate and CaVO$_3$ is evident from the substantial change in the in-plane lattice constants, from $a_x \approx 3.84$ Å and $a_y \approx 3.25$ Å in the 90 u.c. films to $a_x, a_y \approx 3.94$ Å in the 30 u.c. films, where a_x and a_y represent in-plane lattice constants in the x and y directions, respectively. This is accompanied by an increase in localized V^{3+} states in the insulating 15 u.c. sample.

There is a significant shift in the V oxidation state from V^{4+} to V^{3+} and a strong decrease in V–O covalency, which seems to be driven by the increased octahedral tilt caused by the epitaxial strain and the enhanced d–d correlation, as indicated by the reduction in the bandwidth of the d$_{xy}$ band. This ARPES observation aligns well with previous RHEED measurements [86].

5.6 . Conclusions and future outlook

In this ARPES study, we have tracked changes in the electronic structure near the Fermi surface across the MIT. We observe direct evidence of bandwidth reduction, changes in the Fermi surface, and the formation of local V^{3+} moments in the thin-film samples.

Much work remains to be done to fully understand this complex MIT. In particular, future studies focusing on changes in the electronic structure across the thermal MIT may be crucial for tracking structural and magnetic transitions independently of epitaxial strain. The measurements in this study were mostly limited to one photon energy for all the samples, which might correspond to different locations in the BZ along k$_{<001>}$ due to changes in c-axis length. Therefore, careful selection of photon energy is essential in future studies.

The large increase in V^{3+} suggests the formation of local moments and possible magnetic order. Bulk CaVO$_3$ crystals have been found to be paramagnetic [30] ; however, magnetism in correlated thin films under epitaxial strain has not been thoroughly investigated. There is one study where signatures of antiferromagnetic order have been observed in these crystals [89]. Interestingly, in that study, the authors claimed they used stoichiometric CaVO$_3$ crystals, and the sample in which they observed signatures of antiferromagnetism also happened to be insulating.

There is also a lack of theoretical work that considers magnetic and structural transitions in combination with epitaxial strain, as most studies have focused solely on epitaxial strain or reduced dimensionality in the study of MIT in CaVO$_3$ [106, 11, 10, 112], .

We believe this work will be valuable for future studies and the development of applications involving correlated thin-film oxides.

5.7 . Appendix

5.7.1 . Band unfolding

CaVO$_3$ structurally differs from a perfect cubic perovskite crystal due to octahedral distortions, which enlarge the unit cell. This enlargement of the unit cell into a larger supercell (SC) results in the folding of bands into a smaller

BZ (see fig. 5.2 d). In DFT calculations of the SC bands, there is additional coupling $V_{kj,k'j'}$ between the originally uncoupled Kohn-Sham orbitals $|kj\rangle$ and $|k'j'\rangle$ of the smaller unit cell. This coupling extends the Kohn-Sham orbitals and introduces a new crystal momentum K and band index J to represent the periodicity of the enlarged system. However, according to [66], if $V_{kj,k'j'}$ is not significantly strong, the spectral function can still be expressed in terms of the original orbitals $|kj\rangle$ with an added perturbation from V. The retarded one-particle Green's function can be written as

$$G^{-1}_{kj,k'j'}(\omega) = G^{-1}_{0kj,kj}(\omega)\delta_{k,k'}\delta_{j,j'} - V_{kj,k'j'} \tag{5.1}$$

where G_0 is the Green's function of the smaller unit cell system before V is applied. Therefore, the spectral function $A = -\operatorname{Im} G/\pi$ in the smaller unit cell basis can be written as

$$A_{kj,kj}(\omega) = \sum_{KJ} |\langle kj \mid KJ\rangle|^2 A_{KJ,KJ}(\omega). \tag{5.2}$$

The ARPES intensity I is given by

$$\begin{aligned} I &\propto \sum_{KJ} |\mathbf{e}\cdot\langle f|\mathbf{p}|KJ\rangle|^2 A_{KJ,KJ}(\omega) \sim \sum_{KJkn} |\mathbf{e}\cdot\langle f|\mathbf{p}|kn\rangle|^2 |\langle kn \mid KJ\rangle|^2 A_{KJ,KJ}(\omega) \\ &= \sum_{kn} |\mathbf{e}\cdot\langle f|\mathbf{p}|kn\rangle|^2 A_{kn,kn}(\omega), \end{aligned} \tag{5.3}$$

where $\mathbf{e}$ is the light polarization and $|f\rangle$ is the final excited state. The term $|\mathbf{e}\cdot\langle f|\mathbf{p}|kn\rangle|^2$ gives the polarization-dependent matrix elements, and the spectral function $A_{kn,kn}$ implicitly contains the term $\langle kj \mid KJ\rangle$ (which captures structural modulation of the spectral function and is referred to as the structure function) that is absent in A_{KN}. Therefore, the unfolded spectral function $A_{kj,kj}$ is more relevant for direct comparison with ARPES.

The unfolding was implemented using the Unfold-X code [95].

5.7.2 . XPS background subtraction

Excited photoelectrons are subject to interactions within the solid as they escape into the vacuum. These interactions may cause inelastic scattering, which lowers their kinetic energy and gives rise to a background signal in addition to the sharp peaks associated with the photoexcitation energies of atomic orbitals.

As derived by Hüfner [49], the first approximation of the exact Tougaard-type background [128] can be given by the empirical Shirley background [117] :

$$S(E) = k\int_E^{+\infty} \mathrm{d}E' \left(j\left(E'\right) - S_0\left(E'\right)\right) \tag{5.4}$$

where $j\left(E'\right)$ is the intensity at energy E', and S_0 is the intensity just before the peak.

This approximation is only valid if the intensities before and after the peak are not too different. A more accurate form of the background is given by the iterative Shirley function :

$$S_i(E) = k \int_{E}^{+\infty} \mathrm{d}E' \left(j\left(E'\right) - S_{i-1}\left(E'\right)\right), \tag{5.5}$$

where S_0 is a constant background. This empirical fit for the background is found to match well with the exact Tougaard background [133] and has been used in our XPS study of CaVO$_3$ samples.

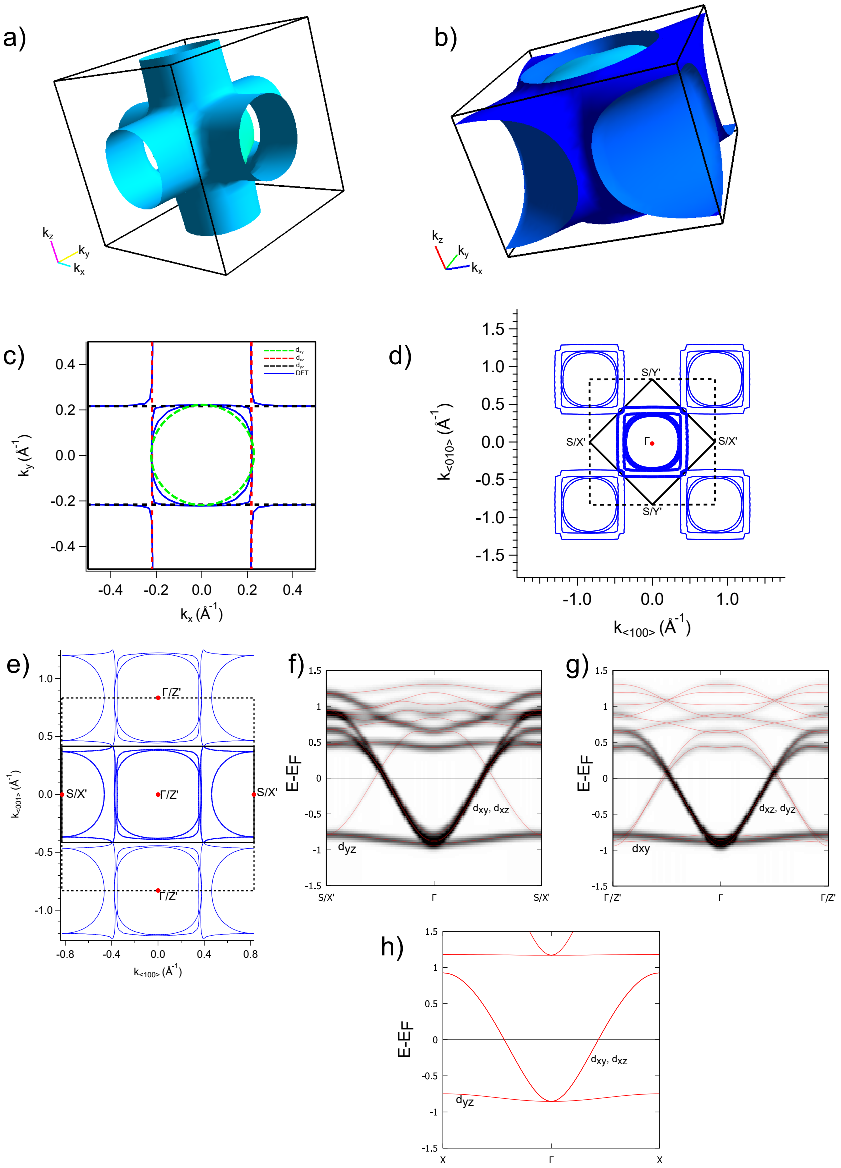

Figure 5.2 – a) Fermi surface of SrVO$_3$, an example of a perfect pervoskite crystal. b) Fermi surface of CaVO$_3$. c) In-plane Fermi surface of SrVO$_3$ at k$_z$=0 plane. Schematic d$_{xy}$, d$_{xz}$ and d$_{yz}$ are represented by dotted lines. d) Fermi surface of CaVO$_3$ along k$_{<100>}$ - k$_{<010>}$ plane at k$_{<001>}$=0. e) Fermi surface of CaVO$_3$ along k$_{<100>}$ - k$_{<001>}$ plane at k$_{<010>}$=0. Black solid line represents the actual BZ boundaries of CaVO$_3$ while black dotted line represents the Fermi surface boundaries of the unfolded 1×1×1 BZ. Band dispersion of CaVO$_3$ calculated along f) k$_{<100>}$ passing through Γ and g) k$_{<001>}$ passing through Γ. Red lines represent the DFT calculated bands and the intensity of unfolded bands to 1×1×1 periodicity is represented in black. X′, Y′ and Z′ are the corresponding high symmetry points in the 1×1×1 BZ. h) Band dispersion along k$_x$ through Γ for SrVO$_3$.

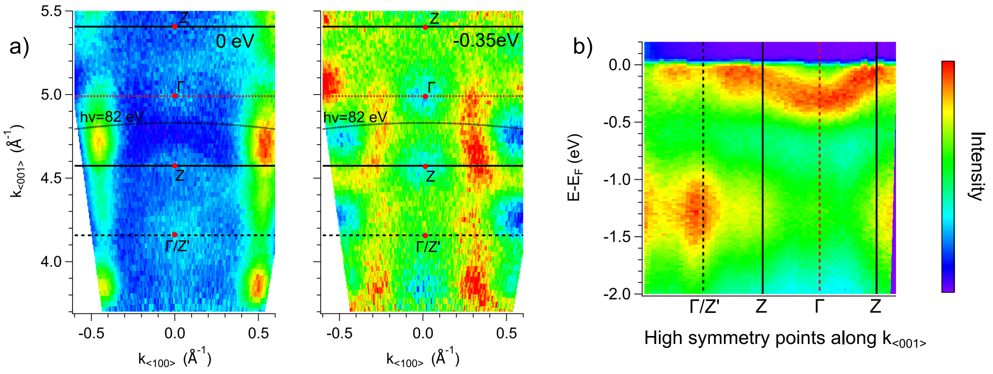

Figure 5.3 – a) Out-of-plane constant energy surface of the 90 u.c. film along k$_{<001>}$ - k$_{<100>}$ at Fermi level and -0.35 eV from Fermi level. b) Band dispersion along k$_{<001>}$ at k$_{<100>} = 0$. All measurements are done with s-polarized light.

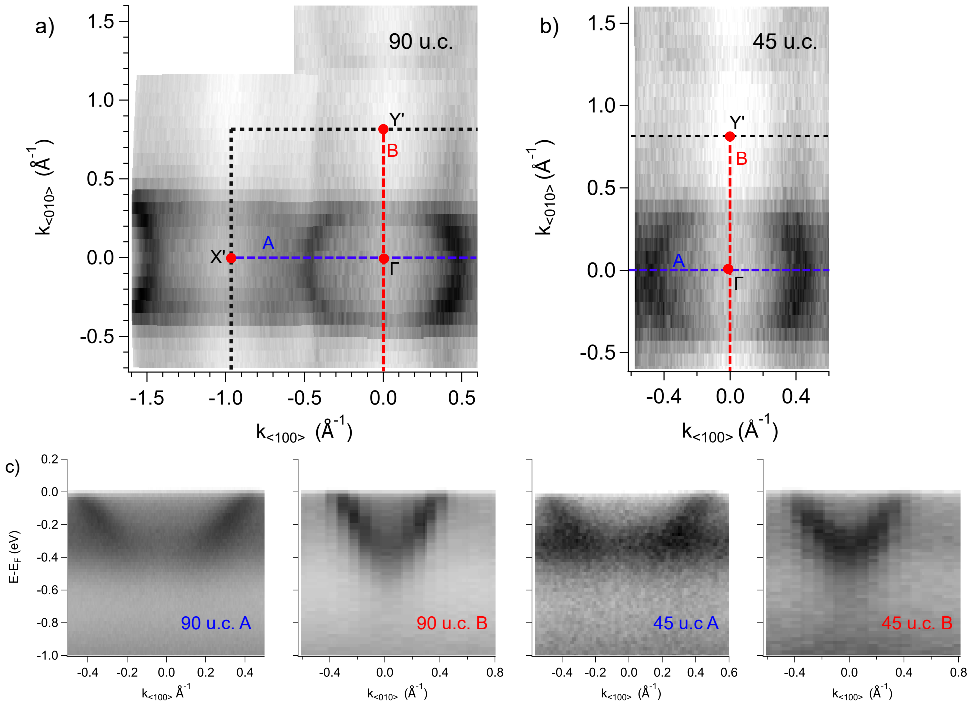

Figure 5.4 – a) Fermi surface of the 90 u.c. sample along k$_{<100>}$ - k$_{<010>}$ plane d) Fermi surface of the 45 u.c. sample along k$_{<100>}$ - k$_{<010>}$ plane. d) Band dispersion along cuts A and B indicated in the Fermi surface plots. All measurements are done with s-polarized light at $h\nu$ = 82 eV.

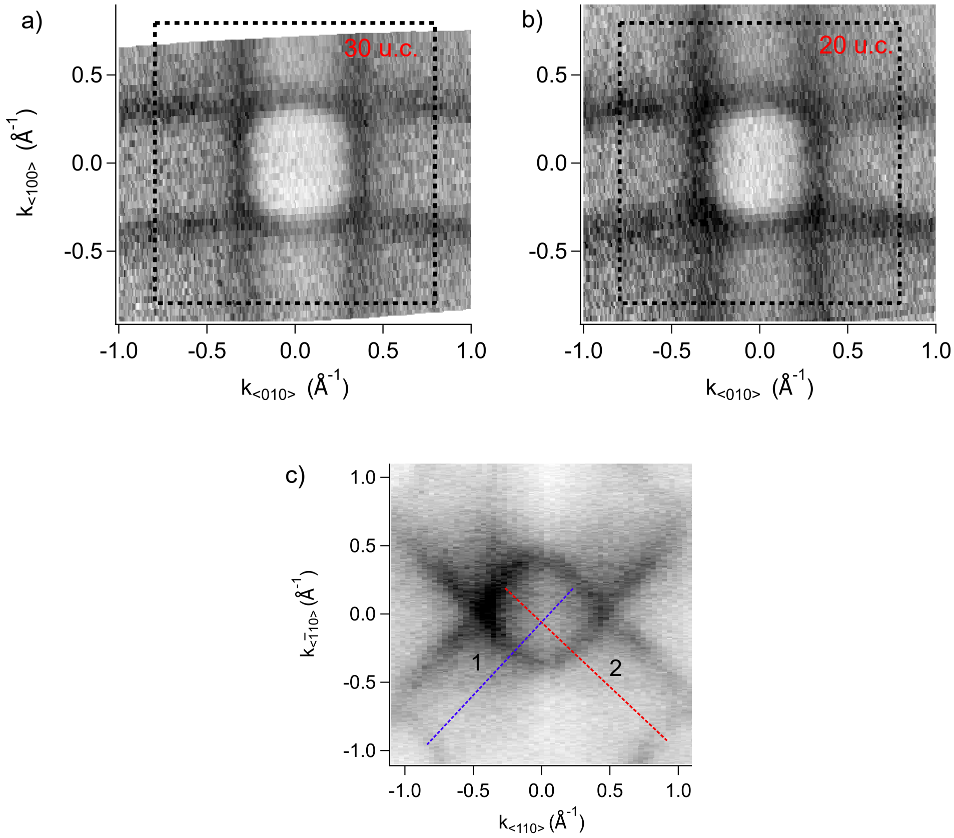

Figure 5.5 – Fermi surface on the k$_{<100>}$ - k$_{<010>}$ plane for a) 30 u.c. sample and b) 20 u.c. sample. c) In-plane Fermi surface of the 45° rotated 30 u.c. sample. Lines 1 and 2 are used to estimate the BZ size. Fermi surfaces were taken at $h\nu$= 82 eV with s-polarized light.

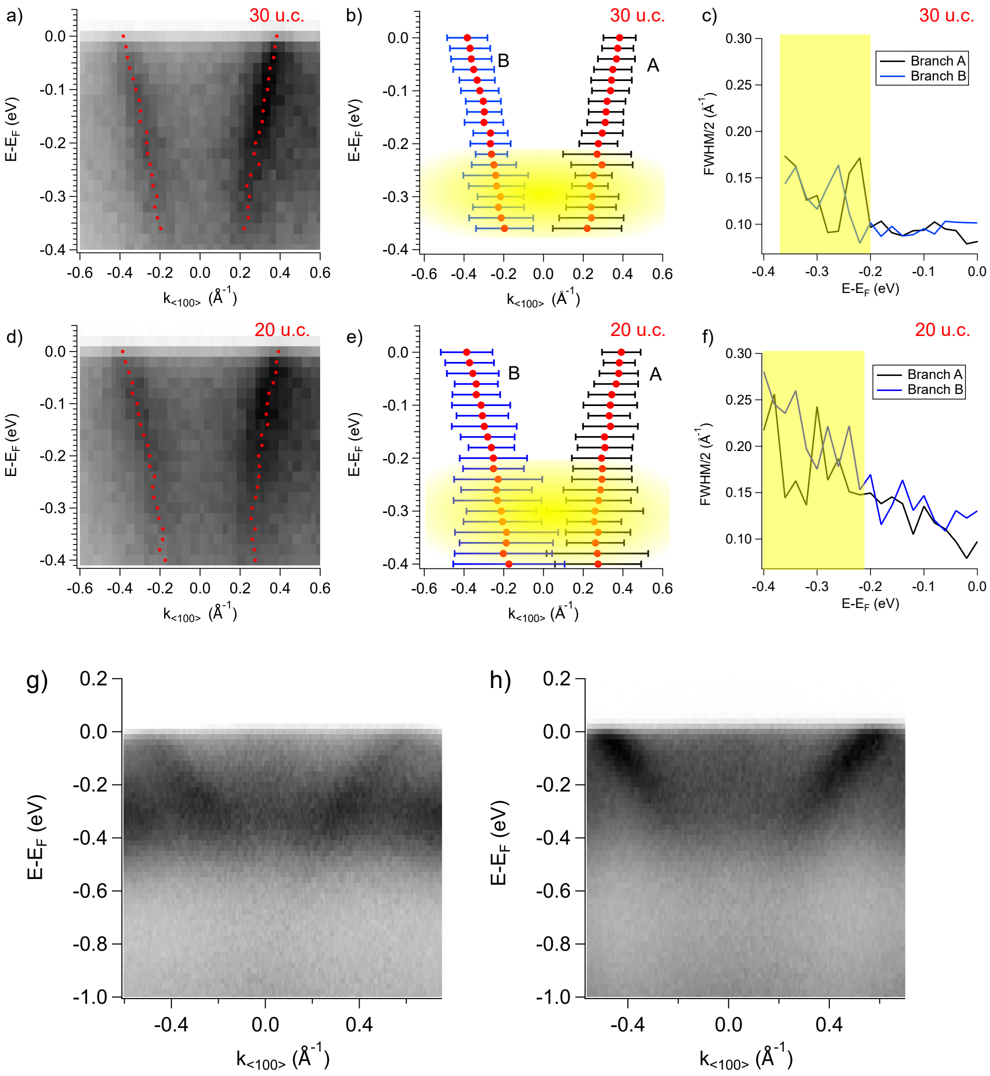

Figure 5.6 – Band dispersion along k$_{<100>}$ at k$_{<010>}$ = 0 for a) 30 u.c. sample and d) 20 u.c. sample. Peak positions from lorrentzian fits of MDC are overlaid with red points. Extracted Lorentzian peaks and broadening (full width at half maxima (FWHM)) represented by error bars for b) 30 u.c. sample and e) 20 u.c. sample. Associated FHWM as a function of energy for extracted bands for c) 30 u.c. sample and f) 20 u.c. sample. Yellow translucent regions indicate region of sudden increase in broadening of Lorentzian peaks. Band dispersions were taken at 82 eVt. Band dispersion along k$_{<100>}$ at k$_{<010>}$ for the 90 u.c. sample at g) 88 eV (bulk Γ) and h) 77 eV ($\Gamma - 0.35BZ$). All measurements were done with s-polarized light.

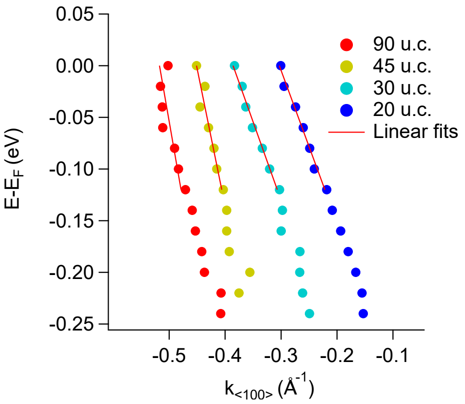

Figure 5.7 – Extracted Lorentzian peaks and linear fits for the 90 u.c., 45 u.c., 30 u.c. and 25 u.c. sample dispersion at 82 eV. The peaks from different samples are shifted along k$_{<100>}$ for better visualization.

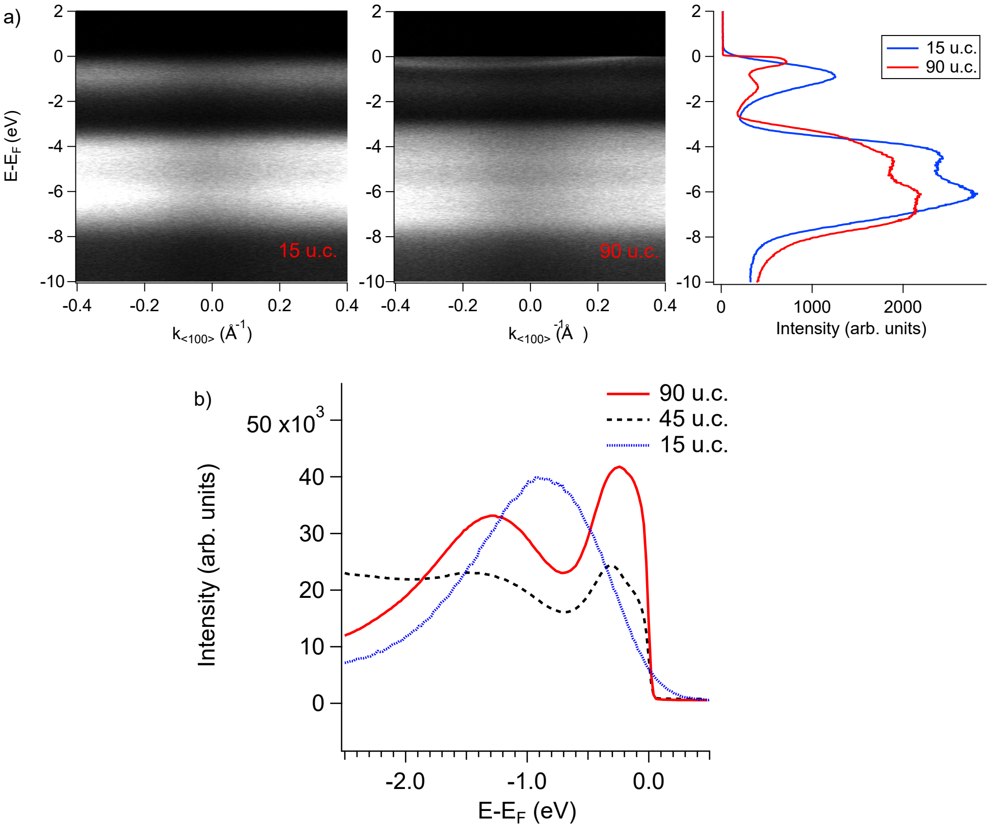

Figure 5.8 – a) Dispersion along k$_{<100>}$ at k$_{<010>}$ = 0 for the 90 u.c. and 15 u.c. samples along with the momentum integrated EDC. b) Integrated EDCs of the 90 u.c, 45 u.c. and 15 u.c. samples in the energy region of the Hubbard band and the quasiparticle peak near Fermi level. All measurements were taken with s-polarized photons at $h\nu$ = 82 eV.

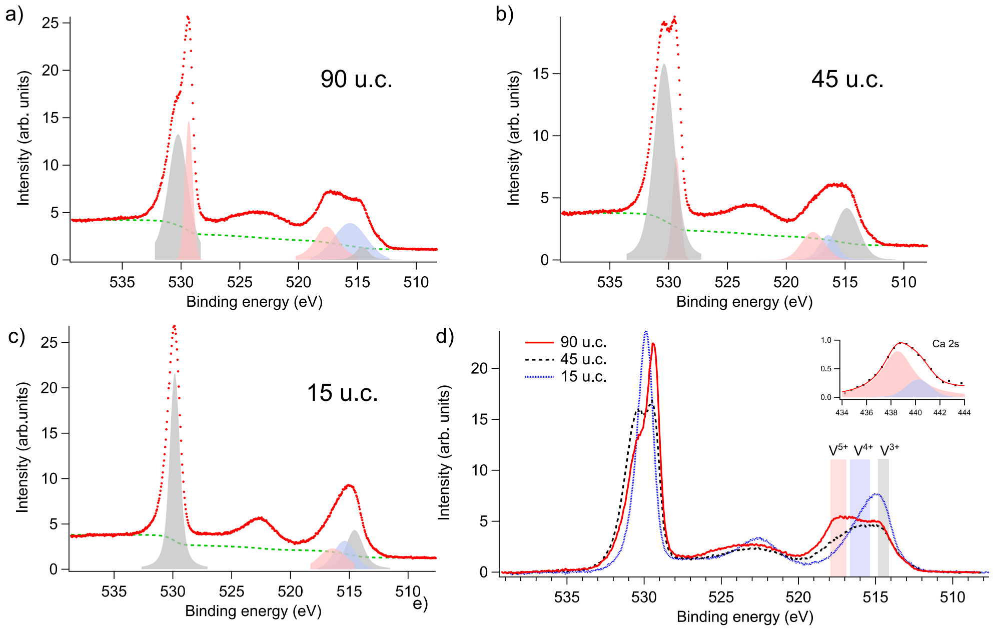

Figure 5.9 – XPS BE measurements for a) 90 u.c., b) 45 u.c. and c) 15 u.c. sample with Voigt peaks fitted to O1s and V $2p_{3/2}$ peaks. Green dotted line indicates the Shirley type background which is subtracted before fitting procedure. d) XPS BE measurements in the range of 505 eV to 540 eV for the 90 u.c., 45 u.c. and 15 u.c. samples. Inset shows Ca 2s peak used to calibrate binding energy of the insulating 15 u.c. sample.

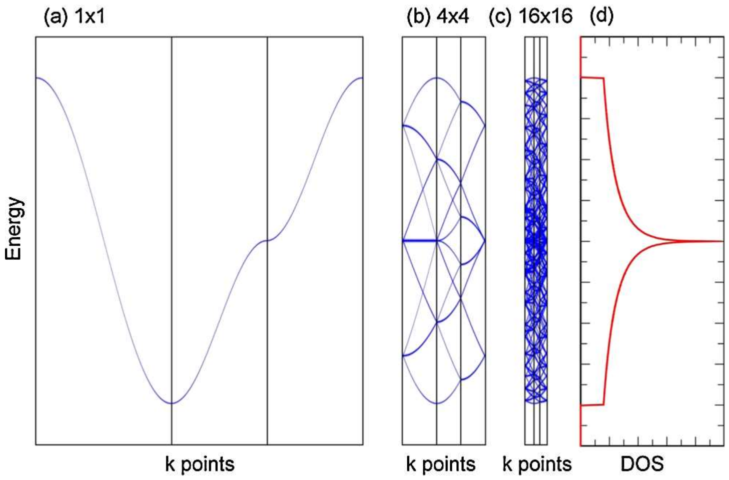

Figure 5.10 – Band structure calculations for a)1×1 unit cell of a nearest neighbour 1-band tight binding model b) 4×4 SC and c) 16×16 SC. The BZ is seen to be shrinking for larger SCs. d) DOS plot for the system. From [66].

6 - Quantum states of 2-D metal dihalide $FeCl_2$ on Au(111)

6.1 . Introduction

2-D materials are defined to be materials with a thickness of few nanometers or less and the electrons are essentially confined to travel in the plane of the material. The discovery of the 2-D material graphene [93], caused an explosion in interest in the investigation of the properties of low-dimensional materials, owing to the unique structural and electronic properties that are very different from those of bulk 3-D materials. These materials have wide-ranging potential applications and are promising substrates for the advancement of new technologies. Graphene-based nanomaterials have also been employed for a variety of medical applications [119]. One of the potential applications envisioned is the replacement of silicon as the de-facto basis for our technology. New materials that overcome the performance and scalability limits inherent to silicon are highly desirable, and 2-D materials provide a rich mine of potential candidates for this task.

Several new 2-D materials have now been discovered and studied, and one of the most popular of them is 2-D transition metal dichalcogenides (TMDCs), MX_2, where M is a transition metal and X is a chalcogen atom. They are especially popular due to their semiconducting nature and are a potential alternative to silicon for technological applications. Another advantage of these materials is that, due to their layered nature with layers separated by a van der Waals (vdW) gap, new heterostructures can be designed by stacking these layers from different materials, analogous to Lego blocks [34], to obtain exotic properties.

Another class of 2-D materials gaining popularity is 2-D transition metal dihalides (TMDH) and trihalides [39], MX_2/ MX_3, where M is a transition metal and X is a halogen. These materials exhibit long-range magnetic order (see 6.9.1) and a semiconducting band gap down to the monolayer (ML) limit and are thus perfect candidates for spintronic applications [3]. Many of these materials are expected to be ferromagnetic from theoretical calculations, owing to their unfilled d-shells, and have also been experimentally verified to exhibit magnetism [137, 39, 77].

In this study, we focus particularly on $FeCl_2$ grown on Au(111) and examine the electronic structure of the resulting heterostructure. Our aim was to gain insights into the electronic structure of insulating $FeCl_2$ ML, and the Au(111) substrate was specifically chosen for its well-studied and widely characterized surface [9], and its ease of use with low-temperature scanning tunnelling microscopy (LT-STM) for sample characterization. However, we unexpectedly find signatures of strong ML-substrate interactions on the Au(111) surface states (SS) and try to characterize this observation with subsequent quasiparticle interference (QPI) measurements.

6.2 . Crystal structure

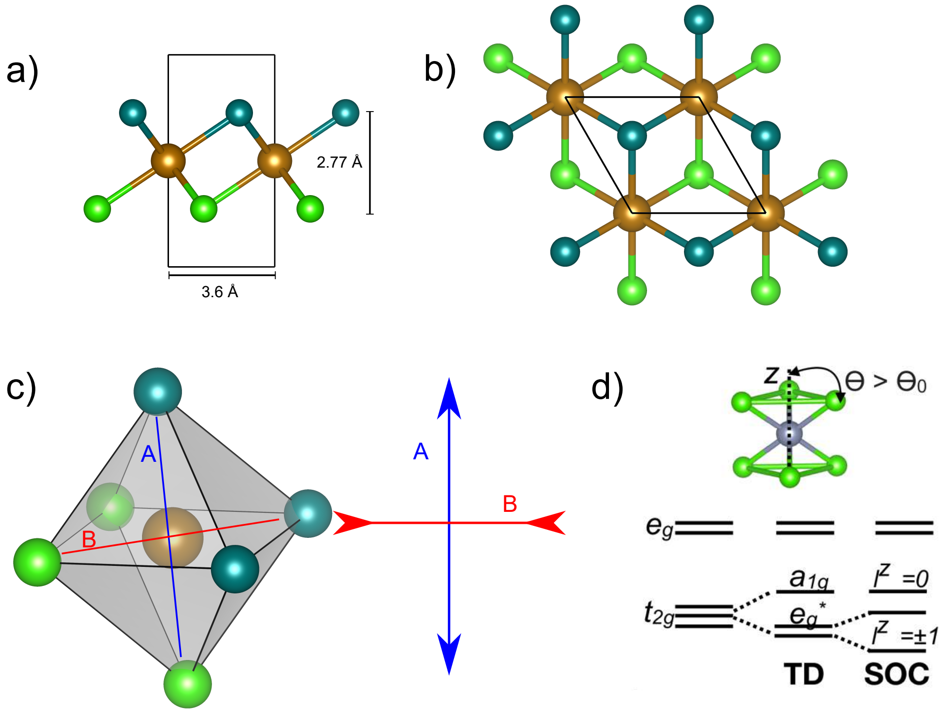

Figure 6.1 – a) Side and b) top view of $FeCl_2$ unit cell. c) Trigonal distortion (TD) of the $FeCl_2$ octahedra represented by elongation and contraction along the A and B axes, respectively. d) Schematic of energy levels of the occupied Fe 3d t_{2g} states in the presence of TD and SOC. Adapted from [17].

Bulk $FeCl_2$ crystals are made up of Cl-Fe-Cl layers separated by a vdW gap of 3 Å . These layers have been observed to exhibit strong ferromagnetic intralayer coupling and a weaker antiferromagnetic interlayer coupling with a large magnetic moment $\sim 4\mu_B$ perpendicular to the plane [137, 17]. The $FeCl_2$ ML still retains its ferromagnetic ground state with a Curie temperature $T_C = 21$ K [2].

A single ML of $FeCl_2$ consists of three atomic planes of Cl-Fe-Cl in a 1-T configuration, with the Fe layer stacked between two Cl layers (fig. 6.1 a, b). The Fe atoms are nominally octahedrally coordinated with some distortions (fig. 6.1 c, d), to 6 neighboring Cl atoms. The octahedral geometry results in the splitting of Fe 3d orbitals into t$_{2g}$ and e$_g$ components. The octahedral geometry results in the splitting of Fe 3d orbitals into t$_{2g}$ and e$_g$ components. Due to the trigonal distortions (TD) to the octahedra, there is a lifting of the degeneracy of the t$_{2g}$ orbitals into a$_{1g}$ and e$_g^*$ orbitals, which are further modified by spin-orbit coupling (SOC) (fig. 6.1 d). 3d^6 Fe^{2+} atoms are expected to have a high-spin (HS) moment of $4\mu_B$ with a total electron spin $S = 2$ [137].

The in-plane crystal forms a trigonal lattice with a unit cell lattice parameter of 3.6 Å and an out-of-plane ML thickness of 2.8 Å, [137]. Note that these values have been observed for bulk crystals, and a single ML might exhibit slight variations in lattice parameters.

6.3 . Monolayer growth

FeCl$_2$ MLs were grown on Au(111) crystals using anhydrous beads from Sigma-Aldrich with a purity of 99.99% [102] and a Knudsen cell evaporator with a quartz crucible.

During the deposition of FeCl$_2$ at 10^{-9} mbar, the substrate was constantly heated to 90°C to ensure large-area island growth. The amount of evaporated material was estimated before growth using a quartz crystal microbalance (QCM), while low-temperature scanning tunnelling microscopy (LT-STM) and low-energy electron diffraction (LEED) were used for final calibration.

The STM and scanning tunnelling spectroscopy (STS) experiments were performed using a commercial Scienta-Omicron LT-STM at 4.3 K from Laboratorio de Microscopias Avanzadas (University of Zaragoza) and 10^{-12} mbar base pressure.

Fig. 6.2 b, c show the large-scale topographical (0.5 μm × 0.5 μm) images of the prepared sample, which were then used to estimate the coverage of FeCl$_2$ to be $\sim$ 0.5 ML. The majority of the coverage is identified to be the FeCl$_2$ ML with an apparent thickness of 3.2 Å above the Au(111) surface. We observed a few small islands of material (fig. 6.2 c) over this ML with an apparent thickness of 3.1 Å which we attribute to the second ML of FeCl$_2$. The herringbone Au(111) [9] superstructure can still be observed on the FeCl$_2$ layer, which points to the weak interaction between the FeCl$_2$ ML and the Au(111) substrate. This weak interaction also suggests that the FeCl$_2$ ML is separated by a vdW gap from the substrate.

Smaller scale topographical images (fig. 10 nm× 10 nm) reveal the presence of modulation of the FeCl$_2$ ML by an apparent depth of 0.5 Å . These modulations are pseudo periodic in nature and appear as dark and bright spots in the image (fig. 6.2 d). The origin of this surface modulation is not clear. This modulation does not follow the herringbone pattern of the Au(111) substrate underneath and are not caused by defects of the top Cl layer of the FeCl$_2$ ML which can be verified by the observation of perfect hexagonal lat-

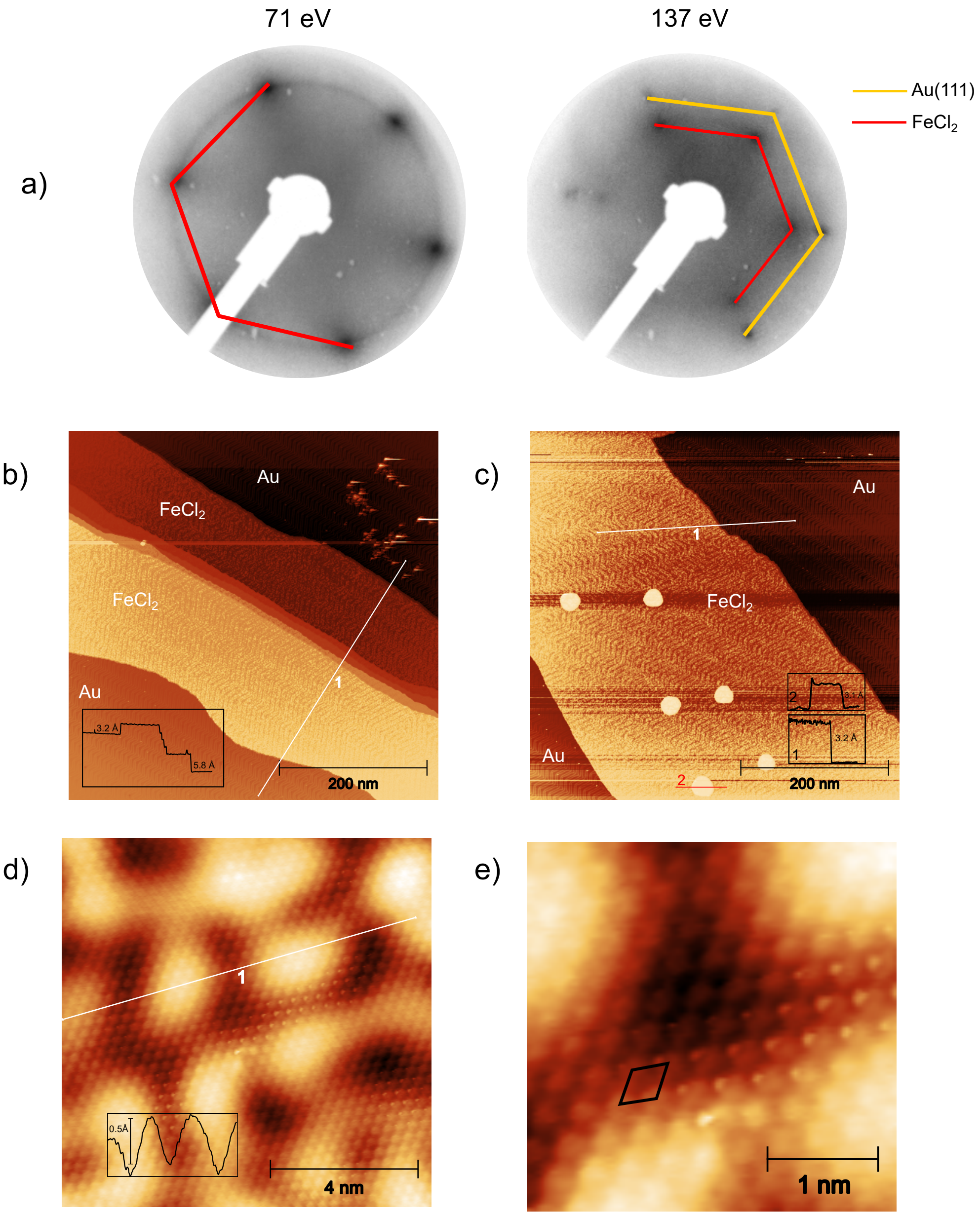
71 eV
137 eV
a)
Au(111)
FeCl$_2$
b)
Au
FeCl$_2$
FeCl$_2$
Au
3.2 Å
5.8 Å
1
200 nm
c)
Au
1
FeCl$_2$
2
3.2 Å
1
Au
2
200 nm
d)
1
0.5Å
4 nm
e)
1 nm

Figure 6.2 – a) LEED pattern for 0.5 ML $FeCl_2$/Au(111) at 71 eV and 137 eV. Hexagonal spots from Au(111) and $FeCl_2$ are drawn. b), c) Topographical images in a 0.5 μm × 0.5 μm region for the 0.5 ML $FeCl_2$/Au(111) (V_b = 1.6 V, I_t = 10 pA). Numbered line profiles are shown in the inset. d) A 10 nm × 10 nm topographical image of the $FeCl_2$ ML with the surface modulation shown in the inset (V_b = 3 mev, I_t = 300 pA). e) Small scale topographical image of the $FeCl_2$ ML with the unit cell drawn on (V_b = 3 mev, I_t = 300 pA).

tice observed in the topography. However, these surface modulations could be caused by defects in the underlying Fe and bottom Cl layer. The $FeCl_2$ ML lattice constant is observed to be $\sim 3.65 \pm 0.5$ Å which is slightly bigger than the bulk lattice constant of ~ 3.6 Å observed for these materials [137]. This slight enlargement on lattice hints at enhanced distortion of the octahedral co-ordination of Fe-Cl bonds.

6.4 . Bulk band spectra

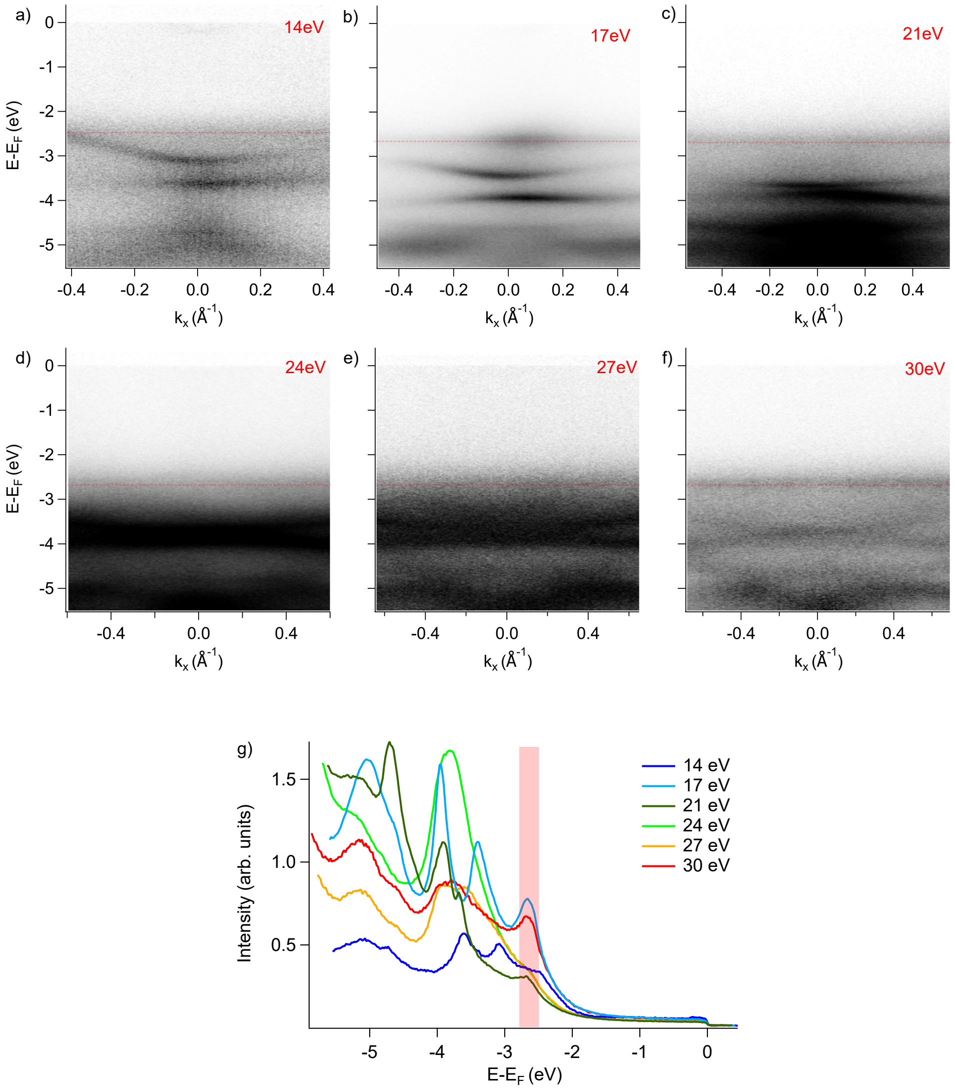

Figure 6.3 – ARPES measurements at 30K with $C+$ polarized photons with photon energy of a) 14 eV, b) 17 eV, c) 21 eV, d) 24 eV, e) 27 eV, and f) 30 eV. Dotted red line is overlaid on $FeCl_2$ valence band maxima. g) Angle-integrated EDCs of the ARPES measurements at different energies. Transparent red region indicates the position of $FeCl_2$ valence band.

Valence band ARPES spectra for 1 ML $FeCl_2$/Au(111) were measured at the LOREA beamline in synchrotron ALBA. A distinct non-dispersing flat band was observed at $\sim$ -2.7 eV with a bandwidth of $\sim$ 0.3 eV. Apart from a small shift in band position to $\sim$ -2.5 eV at hν = 14 eV compared to other photon energies used, no change in the nature of dispersion was observed for this band with varied photon energy. This behavior is expected of a 2-D system [88], which does not disperse normal to the sample plane. The origin of this band is assigned to the $FeCl_2$ valence band. The position of this band differs from the peak position observed in previous STS experiments [2], where the valence band maximum is at -2 eV. No other $FeCl_2$ bands could be identified. This could be due to the high intensity of bulk Au bands below -3 eV, which completely mask the signal from the $FeCl_2$ ML.

The reason for the shift in energy of this band at hν = 14 eV is not clear, it could be due to a larger than expected spread of the $FeCl_2$ wavefunction in the z-direction or due to contributions of Au bands near the binding energy of -2.5 eV.

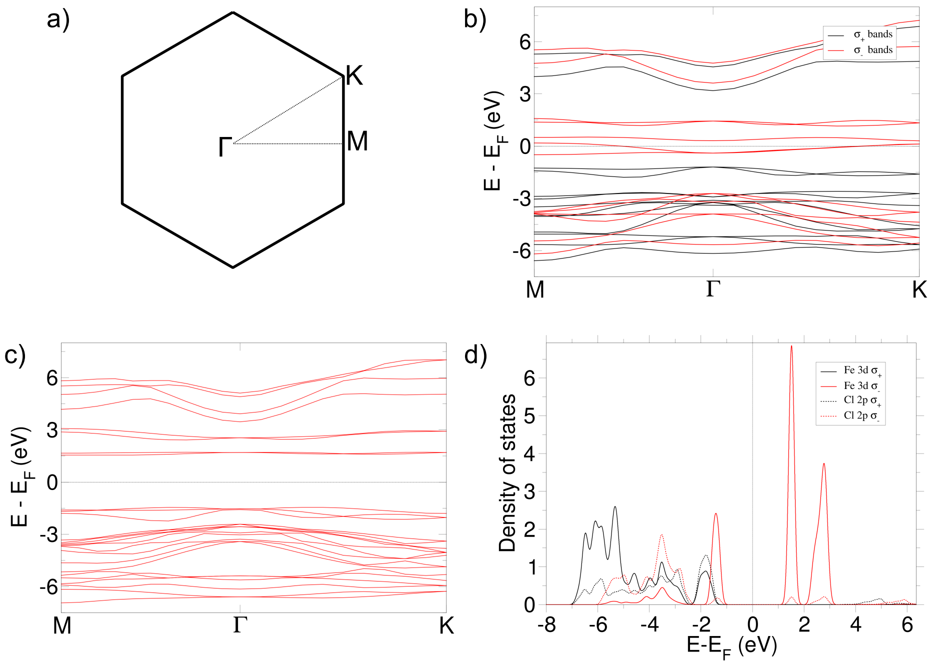

Figure 6.4 – a) 2-D Brillouin zone (BZ) of the ML $FeCl_2$ unit cell. b) Ferromagnetic band structure in the absence of SOC and Hubbard U. c) Band structure with SOC and U included. d) Orbital and spin-projected DOS of the $FeCl_2$ ML.

DFT+U+SOC calculation of the ML band-structure in the out-of-plane ferromagnetic configuration (the preferred magnetic ground state according to previous calculations [17, 67]) was performed and is shown in fig. 6.4 c. At the energy of -1.5 eV, we see three nearly flat bands well separated from the other bands. The exact energy of this valence band is arbitrary, as the Fermi level in the calculation can be set anywhere in the band gap. The bandwidth averaged along the M-Γ-K direction for these bands is 0.4 eV, which is equal to the bandwidth of $\sim$ 0.4 observed in ARPES. Using the value of 3.5 eV for Hubbard correlations, the calculated band gap is 3.04 eV, which is smaller than the reported value of 4.2 eV [2].

Ferromagnetic DFT calculations for the ML ground state also reveal that the ML FeCl$_2$ is conducting, with minority spin σ_- carriers crossing the Fermi level. With the introduction of U+SOC, it becomes insulating with a semiconducting band gap of 3.04 eV, similar to the gap reported in previous theoretical calculations [17, 67]. The Fe 3d t$_{2g}$ states in the majority spin σ_+ channel are completely occupied, while only one t$_{2g}$ state is occupied by σ_- electrons. The calculated magnetic moment per Fe atom is 3.56 μ_B, which corresponds to the high-spin (HS) $S = 2$ configuration for Fe^{2+} ions.

6.5 . STS measurements

Constant height STS measurements were performed at various points on the sample to measure the LDOS. The pure Au(111) surface has the SS peak at the expected energy of -0.45 eV. The STS spectra on FeCl$_2$ ML are seen to depend upon the location of the point on the sample. The bright spots, as observed in the topographic and dI/dV images at 1.5 eV sample bias, have peaks shifted closer to the Fermi level. There are now multiple peaks present near the Fermi level, the first being at -0.23 eV followed by peaks at -0.12 eV, 0 eV and 0.11 eV (fig. 6.5 e). The STS at dark spots has a broad LDOS peak centered around 0.3 eV bias. The LDOS at the bright spots also has a strong increase in intensity at 1.22 eV bias, suggesting the onset of the FeCl$_2$ conduction band at this energy. The conduction band onset value of 1.22 eV differs from previous STS measurements [2], where they assign $\sim$ 2 eV as the conduction band minima. This intensity increase at 1.22 eV is noticeably absent in STS at dark spots on FeCL$_2$.

6.6 . Surface state dispersion

ARPES measurements performed on the 0.5 ML FeCl$_2$/Au(111) near the Fermi level, reveal the presence of a dispersing band close to the Fermi level, with the band bottom $\sim$ -0.23 eV in addition to the Au(111) SS (fig.6.7 b). The energy of the band bottom matches the peak at -0.23 eV observed in STS on FeCl$_2$.

To gain insights into the origin of this band, we performed STM QPI measurements. dI/dV maps were obtained for a ML island of FeCl$_2$ on Au(111) at different bias voltages in the vicinity of the Fermi level (fig. 6.6 a,b). We then

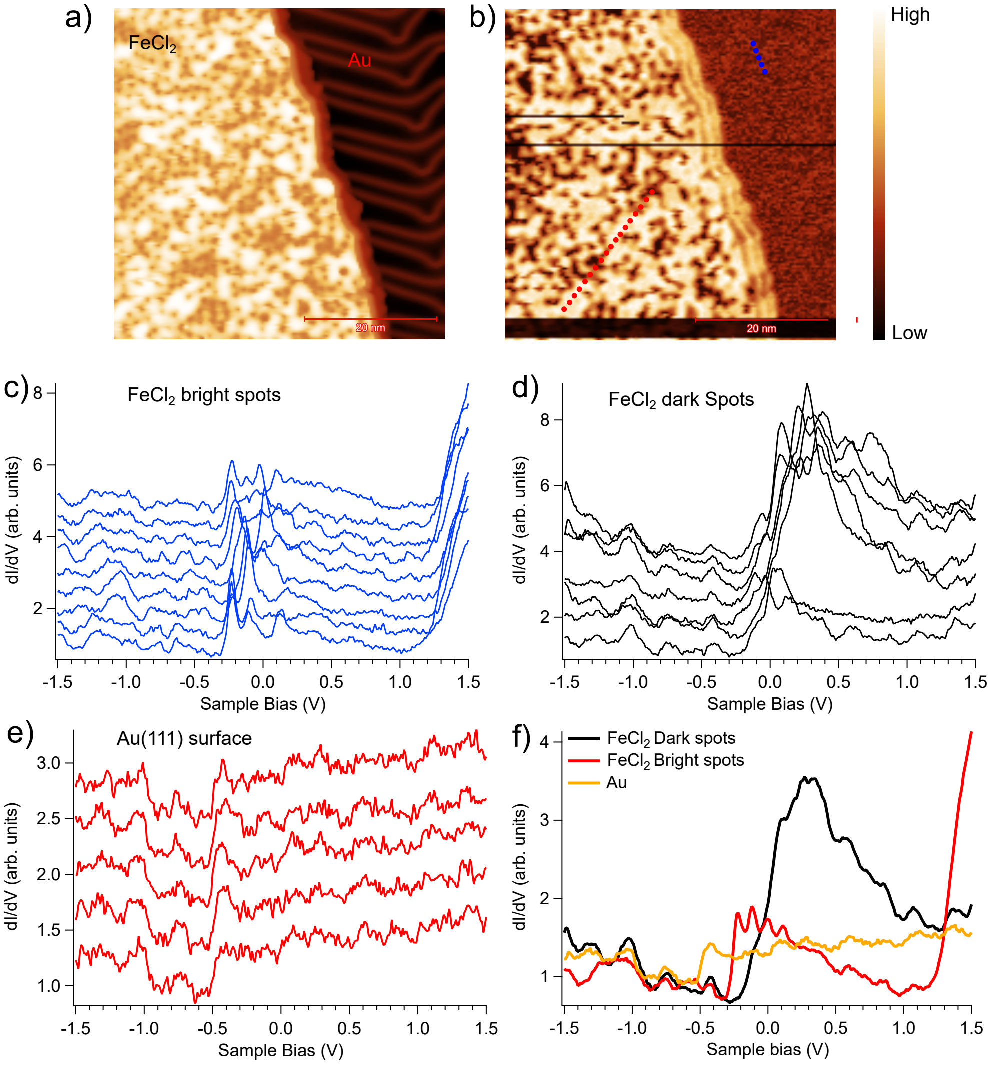

Figure 6.5 – a) Topographical image and b) dI/dV map of 1 ML $FeCl_2$ (V_b = 1.5 V, I_t = 50 pA) . Red and blue dots represent spots for STS point spectra at the $FeCl_2$ layer and Au(111) surface respectively. c) STS at bright spots in dI/dV map at 1.5 eV. d) STS at dark spots in dI/dV map at 1.5 eV. e) STS at points on Au(111) surface. f) Averaged STS profiles for bright, dark and Au spots from c,d and e.

isolated the $FeCl_2$ area and the Au(111) surface, and performed Fourier transformation of the dI/dV maps to get QPI maps at different energies, using the QPI data on the isolated Au(111) surface as a reference. The QPI maps were then integrated radially to get the angle-averaged scattering vector **q**. This was done to improve the poor signal-to-noise ratio in our data.

On the isolated Au(111) surface we recover the expected dispersion of the Au SS with the band bottom $\sim$ -0.45 eV. QPI measurements on the isolated $FeCl_2$ island reveal the presence of a dispersing band, which we call $FeCl_2$ α,

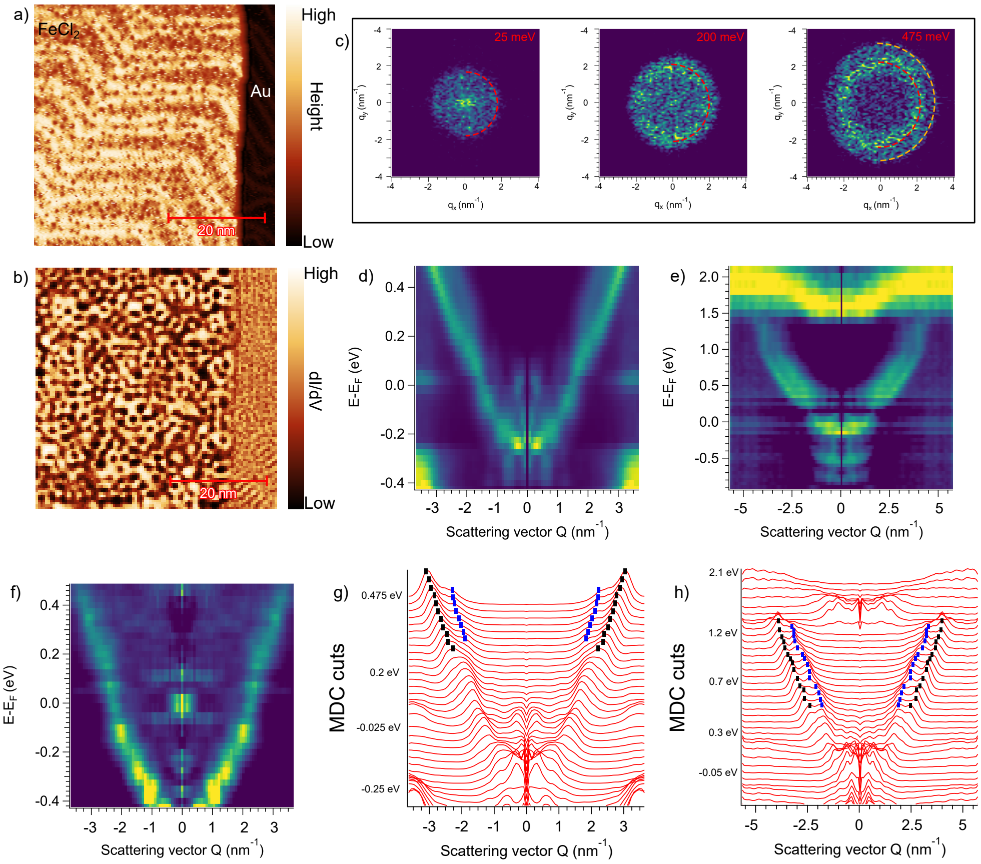

Figure 6.6 – a) Topographical image showing the FeCl$_2$ ML island (V_B = -0.45 e V, I_t = 50 pA) STM dI/dV map at 75 meV acquired in the same region as (a) . c) QPI maps obtained by Fourier transform of the dI/dV maps at 25 meV, 200 meV and 475 meV for the isolated FeCl$_2$ ML. Red and yellow dashed lines are guides for the observed scattering vector **q**. Dispersion relation between **q** and energy E obtained by radial integration of QPI maps for d) FeCl$_2$ ML in a small energy range around E_F, e) FeCl$_2$ ML in a wider energy range and f) Au(111) surface. MDC cuts for **q**-E dispersion in g) d and h) e at different energies.

with a band bottom at $\sim$ -0.23 eV, similar to the band observed in ARPES measurements. Curiously, we also observe the presence of an additional dispersing band, labeled FeCl$_2$ β, which is most clearly observed 0.2 eV above E_F, and for QPI measurements done in the bias range of -0.6 eV to 2.0 eV around the Fermi level (fig. 6.6 e, h).

The peaks from the radially integrated QPI maps are extracted by fitting with a Gaussian function, and the values are transformed from **q**-space to **k**-space, with the simple transformation **q** = 2**k**, which is valid here for the case of isotropic scattering from Au(111) SS [99]. The energy-momentum dispersion thus calculated is shown in fig. 6.7 (a). The β band appears to have a sharp decrease in effective mass and a nearly constant dispersion wave-vector independent of energy (see fig. 6.7 a) below 325 meV and merges with the α band at 200 meV. Then, going below 100 meV, we again recover parabolic dispersing features expected from the β band. Fig. 6.7 b shows the extracted QPI peaks overlaid on top of the ARPES data, which shows a really close agreement between the two experiments.

To uncover any structural contributions to the QPI maps, a similar procedure to obtain **q**-E dispersion from dI/dV maps was done for the Fourier transform of topographical images taken at different sample biases. As any contribution from the LDOS coming from the structure in dI/dV maps should not change with energy, it would result in a peak with an effectively constant **q** vector in the Fourier transform. Indeed, that is what we observe, with a distinct peak at **q** $\sim$ 1.9 nm^{-1}, corresponding to real space periodicity of 2.1 nm matches closely with the average pseudo-periodicity of 2.3 nm of dark spots calculated from the small scale topographical image as shown in fig. 6.8 c.

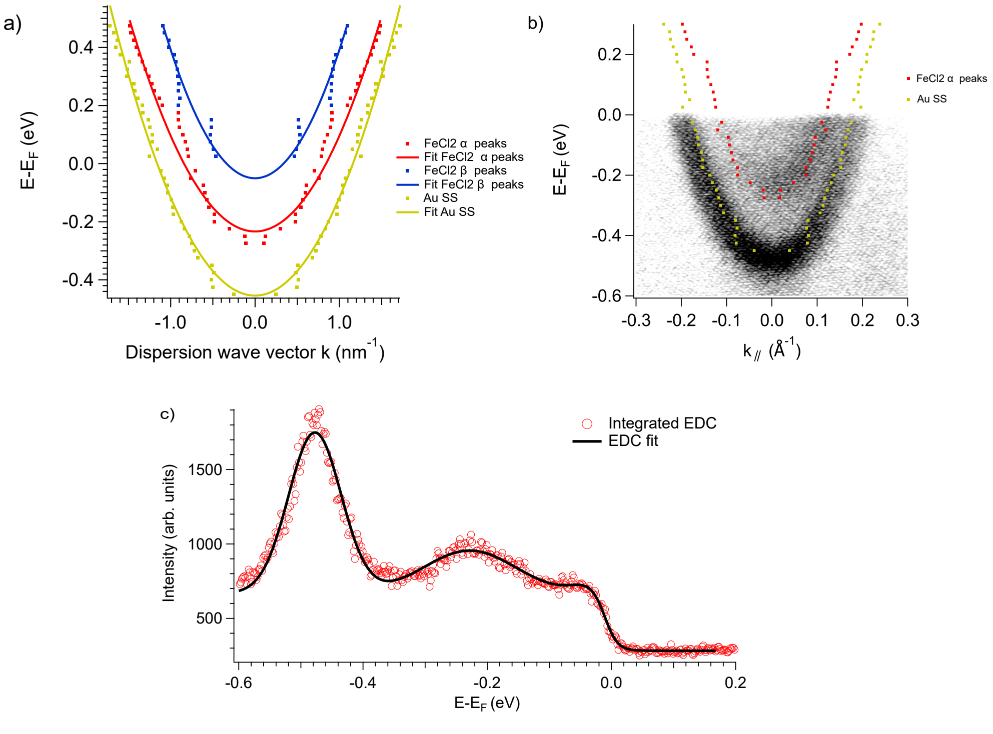

Figure 6.7 – a) Extracted peaks for Au SS and FeCl$_2$ α and β bands from QPI dispersion. b) STM extracted peaks overlaid on ARPES data for 0.5 ML FeCl$_2$/ Au(111). The data was obtained at temperature T= 16 K and photon energy hν = 17 eV. c) EDC obtained by integrating the ARPES dispersion in a region of 0.05 Å $^{-1}$ around $k_{\|} = 0$.

The extracted peaks were fitted to a parabolic function, and the fitting parameters are summarized in table 6.1. The region between 0 eV and 0.2

eV is omitted for the fit of $FeCl_2$ α peaks, as the dispersion seems to deviate from the expected parabolic behavior in this region. Similarly, the region between 0.1 eV and 0.3 eV is ignored for the fit of $FeCl_2$ β peaks. We also included the band bottoms obtained by fitting the EDC integrated in a region of 0.05 Å^{-1} around $k_{\|} = 0$ from the ARPES measurements with Gaussian functions convolved with a Fermi function.

Band	**Band bottom (eV) (STM)**	**Band bottom (eV) (ARPES)**	**Effective mass (m*/m$_e$)**
Au SS	-0.45 $\pm$ 0.01	-0.48 $\pm$ 0.04	0.37 $\pm$ 0.02
$FeCl_2$ α	-0.23 $\pm$ 0.01	-0.23 $\pm$ 0.07	0.38 $\pm$ 0.02
$FeCl_2$ β	-0.05 ± 0.01	-0.04 $\pm$ 0.03	0.28 $\pm$ 0.02

Table 6.1 – Surface state band parameters extracted from ARPES and QPI

The effective mass (m^*) value is calculated by using the parameters from parabolic fits of the bands in the modified free electron dispersion formula $E(k) = k^2/2(m^*/m_e)$. The effective mass $m^* = 0.37 \pm 0.02\, m_e$ for the Au(111) SS, which agrees with previous experimental studies [140]. The values of $FeCl_2$ α and β bands are $0.38 \pm 0.02\, m_e$ and $0.28 \pm 0.02\, m_e$, which are similarly close to the Au(111) SS masses observed in previous experiments [104].

Overall, we see good agreement between the STM QPI dispersion and the ARPES measurements below the Fermi level.

6.7 . Discussion

The observation of the two dispersing bands with effective masses close to the Au SS is an unexpected finding.The dispersing $FeCl_2$ α band at -0.23 eV, observed both in ARPES and QPI measurements, can be explained by the shift of the Au(111) SS at the $FeCl_2$/Au(111) interface towards the Fermi level. This shift is caused by the decrease in potential well thickness normal to the surface and subsequent depletion of electrons in the surface state. This effect has been well documented in previous experiments involving the deposition of semiconductors [142] and rare gases [5] on the Au(111) surface. However, the origin of a second dispersing band, $FeCl_2$ β, cannot be explained just by this shift.

Second derivatives of intensity along **q**-direction for the large energy range QPI map (fig. 6.9 b) clearly show that indeed there are significant contributions of intensity in our QPI measurements from two dispersing bands. The bands are split by $\Delta k \approx 0.38$ nm^{-1} and $\Delta E \approx 300$ meV. For reference, the values of

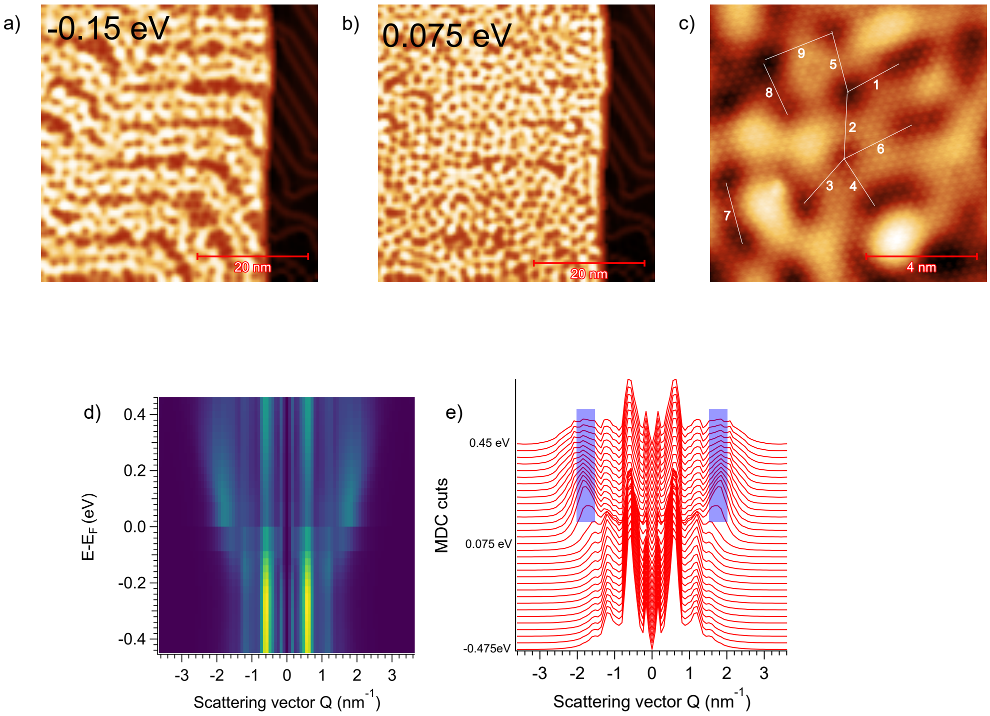

Figure 6.8 – Topographical image at a) V$_B$ = -0.15 eV (I$_t$ = 50 pA) and b) V$_B$ = 0.075 eV ((I$_t$ = 50 pA). c) Small scale atomic resolution topographical image. The numbered line segments are plotted between nearest neighbour defects and are used to calculate average defect distance (V$_b$ = 3 meV, I$_t$ = 500 pA. d) Scattering wave vector **q** obtained by Fourier transform of topographical image in the same region as a) and b) for different energies. e) MDC cuts for d at different energies. Blue region indicates peaks associated with defects in topography.

the Rashba splitting of Au(111) surface states are $2k_{SOC} = 0.26$ nm^{-1} [46, 74] and $\Delta_{SOC} \approx 135$ meV [104] at the Fermi level.

As MLs of FeCl$_2$ are known to exhibit out-of-plane ferromagnetic behavior [2], the magnetic exchange interactions can cause a split in the Fermi sheets of the spin textured surface states (fig. 6.10) [8] by magnetic proximity effects [136]. The difference between the band bottom energies of α and β bands is $\sim$ 0.2 eV, which is the estimate for energy split of these bands. The 0.2 eV energy split would correspond to an extremely large magnetic field of $\sim$ 2000 T. Ni(111) has also been shown to host split surface states, which have been observed by QPI measurements [65], where the splitting is ascribed to majority and minority spin carriers split by an exchange gap.

This situation is very different from Au(111) SS, where the SOC split bands have a strong in-plane spin texture. Inter-band scattering between Rashba split bands such as Au SS is usually strongly suppressed as the two bands

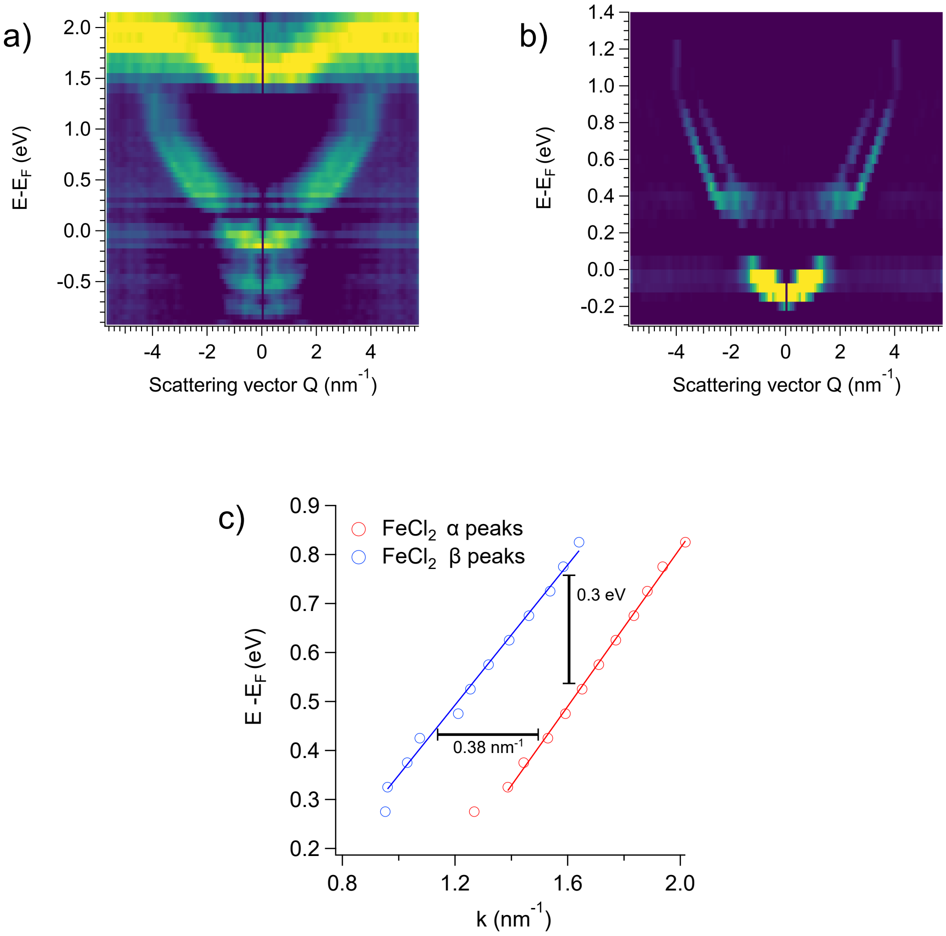

Figure 6.9 – a) **q**-E dispersion of $FeCl_2$ ML in a wide energy range. b) Intensity plot after taking second derivatives of a along momentum **q**. c) Peak positions in second derivative plot for α and β bands extracted from b and converted into k-space.

carry opposite spin-moment and elastic scattering processes preserve spin [107]. This results in only a single scattering vector **q** (see fig. 6.10 b) from inter-band scattering events. However, magnetic impurities can cause spin-flip scattering and thus allow two distinct scattering vectors to be observed in QPI from inter-band and intra-band scattering [114]. As Fe sites on the ML $FeCl_2$ are magnetic, they could promote the spin-flip scattering and thus allow two distinct scattering vector **q**.

The large LDOS around 0.3 eV observed in STS measurements at dark spots might arise from localized electrons around defect sites. Fe and Cl vacancies have been identified in a previous STM study [149] but the correlation between dark spots, like what we observe in our sample, and vacancies had not been established. A theoretical study of defects on $FeCl_2$ ML does

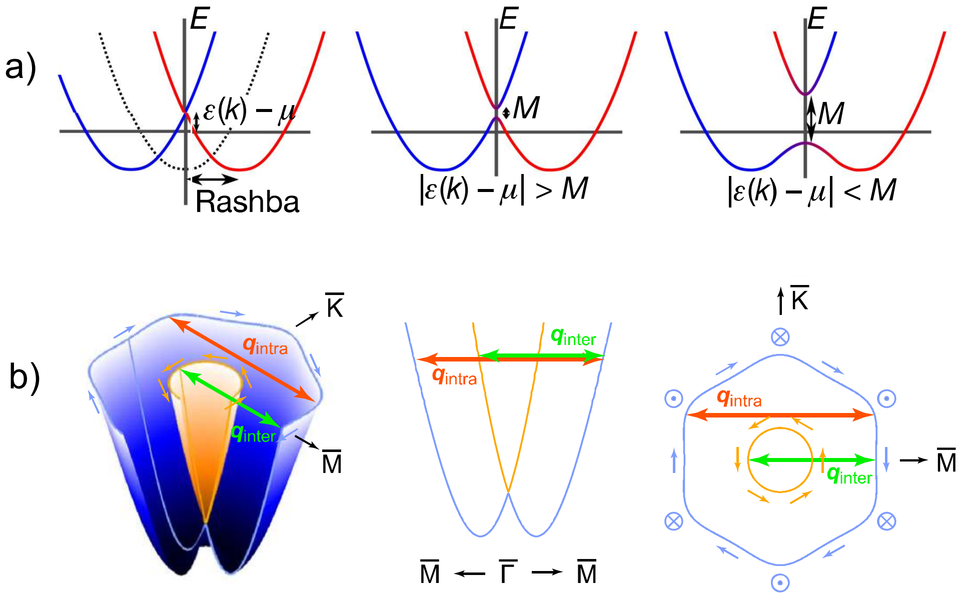
a)
E
$\varepsilon(k) - \mu$
Rashba
E
M
$|\varepsilon(k) - \mu| > M$
E
M
$|\varepsilon(k) - \mu| < M$
b)
$\overline{\text{K}}$
q_{intra}
q_{inter}
$\overline{\text{M}}$
q_{inter}
q_{intra}
$\overline{\text{M}} \leftarrow \overline{\Gamma} \rightarrow \overline{\text{M}}$
$\overline{\text{K}}$
q_{intra}
q_{inter}
$\overline{\text{M}}$

Figure 6.10 – a)Effect of adding spin–orbit interactions and weaker and stronger Zeeman-type magnetization are shown. Adapted from [56]. b) Inter-band and intra-band scattering in Rashba spin-split bands of BiTeI. Adapted from [62].

show that different kinds of defects can change the DOS near the Fermi level [21]. However, a limitation of the study was that it was based on a conducting system without the inclusion of any correlation parameter U. We simulated one possible scenario where the defects are caused by one Fe vacancy per 6×6 unit cell, with a lattice parameter of 2.16 nm, which matches the pseudo-periodicity of dark spots observed by STM. The DOS for the system away from defects and Cl atoms around the Fe defect are shown in fig. 6.11. We indeed observe that the Cl atoms around the defect site contribute to states crossing the Fermi level, while the DOS away from the defect site still preserves the band gap.

The presence of such defects could effectively dope the otherwise insulating system, which can give rise to quantum well states. This effect is also observed in doped Bi$_2$Se$_3$ [60]. We can fit the maxima peak values in the averaged bright spots on FeCl$_2$ ML with a quantum well index n. If those peaks are truly associated with quantum well states due to confinement in z-direction, we should observe a $E \propto n^2$ behaviour. Indeed we can observe this behaviour with n ranging from 10 to 13. However, we also observe a good fit with $E \propto n$ as well ($R^2 = 0.998865$ for E $\sim n$ and $R^2 = 0.995795$ for E$\sim n^2$) (fig. 6.12 b, c). Therefore we cannot definitely assign the origin of these peaks to quantum well states.

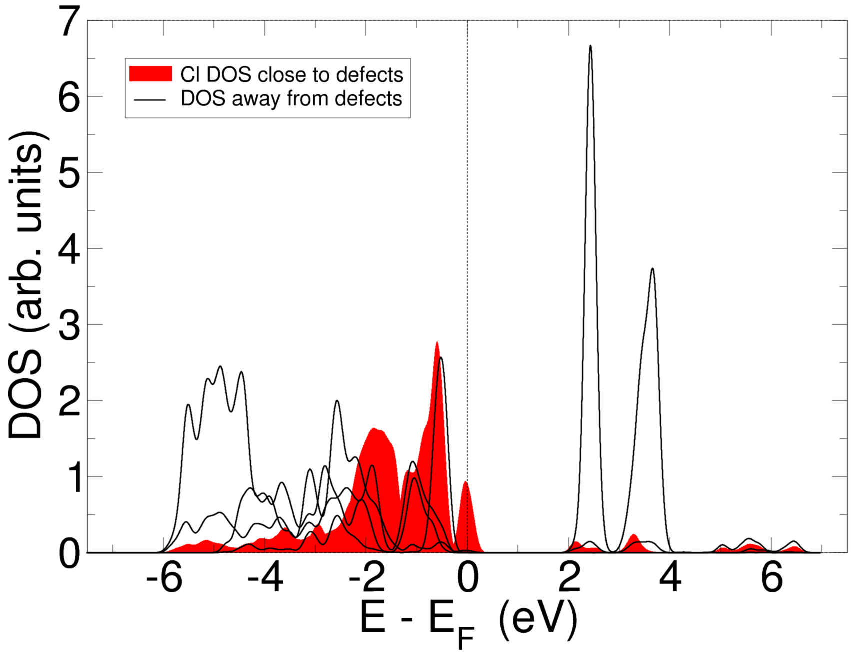

Figure 6.11 – Calculated DOS for 6×6 unit cell with Fe defect. Notice that only the Cl states close to defect sites cross the Fermi level.

The conduction band onset of 1.22 eV observed, has not been documented in the previous experiments where the value of $\sim$ 2 eV was instead used as the conduction band minima [2]. This would mean that the actual band gap of the system is $\sim$ 3 eV rather than the 4.2 eV reported before [2], and closer to the DFT+U calculations (U=3.5 eV).

6.8 . Conclusion and Future outlook

In conclusion, we have observed split surface bands on ML $FeCl_2$/Au(111). The origin of the split bands is theorized to be the shifted Au(111) surface states split apart by exchange interactions by the magnetic overlayer of $FeCl_2$. The energy of this splitting is $\sim$ 200 meV. A similar value of giant Rashba splitting has been reported before for BiTeI [51], where a splitting of $\sim$ 100 meV was observed. However, we are not aware of any experiments showing this large Rashba splitting on the Au(111) surface before.

The potential strong effect of magnetic proximity observed in our system opens the door to a whole host of applications. The ease of preparation of the $FeCl_2$ ML lends itself well to practical applications in spintronics [26, 130],

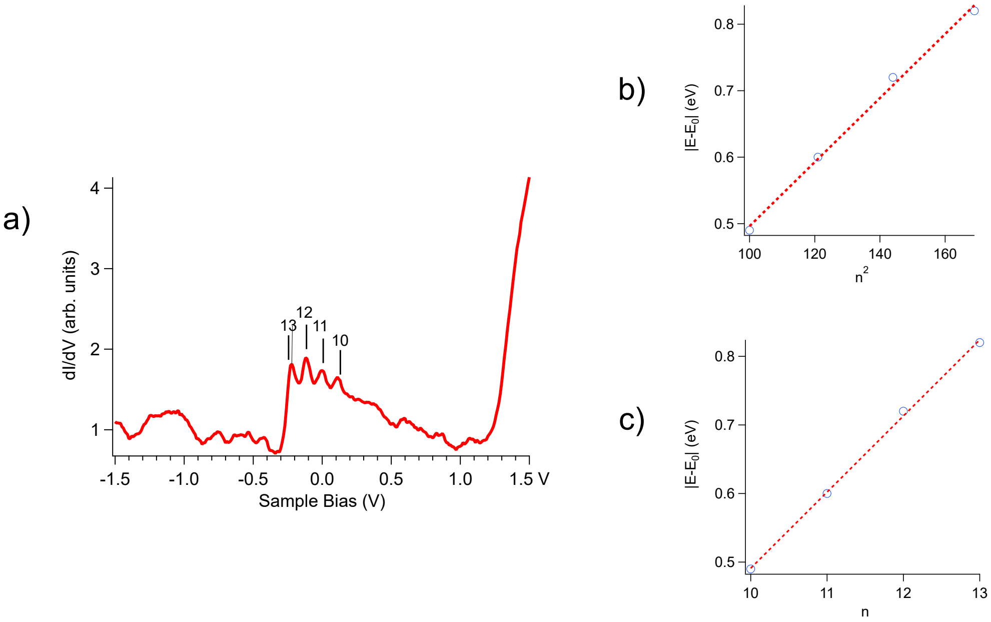

Figure 6.12 – a) Averaged STS from bright spots on $FeCl_2$ in 6.5 b. Peaks are indexed by best fit quantum well states. b) $E \sim n^2$ plot. c) $E \sim n$ plot. E_0 is set to 0.6 eV. Blue dots represent data points and dashed red line is the linear fit.

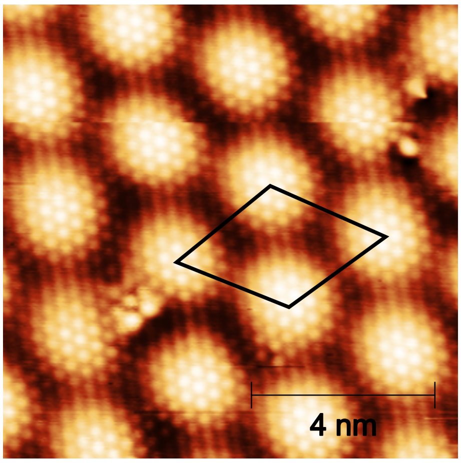

Figure 6.13 – Moiré modulation on ML $FeCl_2/Bi_2Se_3$ heterostructure (V_b = -1 V, I_t = 50 pA). The Moiré cell is drawn with the lattice constant of 2.6 nm.

topological superconductivity as reported in $CrI_3/NbSe_2$ [56], and Eus/Au(111) [136] heterostructures, and a whole lot of devices based on van der Waals heterostructures [34].

Another exciting area of exploration is the observation of Moiré superstructures in heterostructures of van der Waals materials [12]. These Moiré modulations of potential can result in a drastic change in the electronic structure of the heterostructure, as famously shown in the case of twisted bilayer graphene [19]. Inspired by recent theoretical work on Moiré topological materials [143], we have already begun exploring van der Waals heterostructures of transition metal dihalides such as $FeCl_2$ on topological insulators such as Bi_2Se_3 (fig. 6.13). The possible intersection of magnetism, topological states, and Moiré modulation is sure to offer a rich variety of new physics.

A limitation of this study could be the poor **q**-space resolution in QPI measurements. Higher quality measurements would be needed to unambiguously resolve the electronic structure near the Fermi level. We are also not sure of the origin of all the four peaks at the Fermi level as observed by STS. Another open question is the role of defects in the electronic structure of the $FeCl_2$ ML. We see that, indeed, defects do modify the electronic structure near the Fermi level as well as states near the conduction band minima, but the exact nature of these defects is not clear and requires more experimental and theoretical work.

We believe this work lays the foundation for many future theoretical and experimental studies on the emerging field of magnetic transition metal halide-based low-dimensional materials. We are hopefully able to convey the potential richness of physics to be still explored in such systems.

6.9 . Appendix

6.9.1 . Magnetism in two dimensional transition metal dihalides

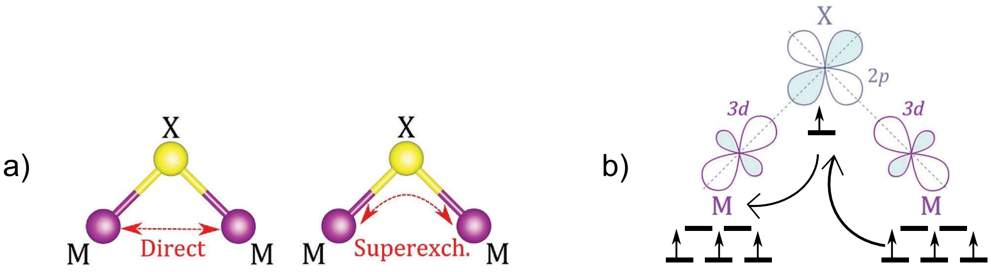

Figure 6.14 – a) Schematic of direct and superechange interaction in a transition metal dihalide MX_2. b) M-X-M superexchange interaction for 90 ° bond angle. Adapted from [67].

Purely two dimensional (2-D) magnetism is theoretically prohibited by Mermin-Wagner theorem [87] which states that continuous symmetries cannot be spontaneously broken in dimension $d \leq 2$. However, we now have large array of van der Waals based materials, which seemingly violate this rule. This has been explained by the observation of electronic anisotropies introduced by SOC, spin exchanges interactions, structural anisotropies and finite size effects [53].

There are competing effects which dictate the type of magnetic order observed in the dihalide. The first is the direct exchange interactions between transition metal (TM), which favors antiferromagnetic order. The other interaction is the superexchange interaction which favours a ferromagnetic order for a 90° M-X-M as in the case of TMDH, according to empirical rules called Goodenough-Kanamori-Anderson (GKA) rules [40, 55] (fig. 6.14). These nature of these interactions depends on the type of TM. From DFT calculations [67], TMDH with Mn favours the direct antiferromagntic interaction while Fe, Co and Ni dihalides favour a ferromagnetic ground state from superexchange interactions.

6.9.2 . DFT calculations

DFT calculations for the ML $FeCl_2$ system were performed with the *QUANTUM ESPRESSO* [36] code, with a plane wave basis, using the polarized Generalized Gradient Approximation (GGA) exchange-correlation functional of Perdew-Burke-Ernzerhof (PBE) from the Standard solid-state pseudopotentials (SSSP) efficiency library [101, 75]. The plane wave kinetic energy cutoff is set to 90 Ry and the charge density kinetic energy cutoff is 1080 Ry. The self-consistent calculations were done with a 10×10×1 k-point grid. A 20×20×1 dense k-point grid was used to calculate the spin-resolved DOS. The lattice parameters used for the calculations were $a = 3.6$ Å for the hexagonal unit cell and a ML thickness of 2.8 Å. A slab model with a vacuum of 13 Å was used to simulate the ML. The calculations were initialized with a small out-of-plane spin moment on all Fe sites to simulate the ferromagnetic ground state.

For the DOS calculation of an Fe defect, a 6×6 periodic unit cell with a single Fe vacancy was used. The self-consistent and the DOS calculations were calculated only at the Γ point.

Bibliography

[1] DA30-L - Scienta Omicron (https://scientaomicron.com/en/Instruments/Electron-Analysers/DA30-L).

[2] Andrea Aguirre, Andrés Pinar Solé, Diego Soler Polo, Carmen González-Orellana, Amitayush Thakur, Jon Ortuzar, Oleksandr Stesovych, Manish Kumar, Marina Peña-Díaz, Andrew Weber, Massimo Tallarida, Ji Dai, Jan Dreiser, Matthias Muntwiler, Celia Rogero, José Ignacio Pascual, Pavel Jelínek, Maxim Ilyn, and Martina Corso. Ferromagnetic Order in 2D Layers of Transition Metal Dichlorides. *Advanced Materials*, 36(28):2402723, 2024. _eprint: https://onlinelibrary.wiley.com/doi/pdf/10.1002/adma.202402723.

[3] Ethan C. Ahn. 2D materials for spintronic devices. *npj 2D Materials and Applications*, 4(1):1–14, June 2020. Publisher: Nature Publishing Group.

[4] Emad K. Al-Shakarchi and Natheer B. Mahmood. Three Techniques Used to Produce BaTiO3 Fine Powder. *Journal of Modern Physics*, 2(11):1420–1428, November 2011. Number: 11 Publisher: Scientific Research Publishing.

[5] Thomas Andreev, Ingo Barke, and Heinz Hövel. Adsorbed rare-gas layers on Au(111): Shift of the Shockley surface state studied with ultraviolet photoelectron spectroscopy and scanning tunneling spectroscopy. *Physical Review B*, 70(20):205426, November 2004.

[6] Vladimir I. Anisimov, Jan Zaanen, and Ole K. Andersen. Band theory and Mott insulators: Hubbard U instead of Stoner I. *Physical Review B*, 44(3):943–954, July 1991. Publisher: American Physical Society.

[7] Neil W. Ashcroft and N. David Mermin. *Solid state physics*. Holt, Rinehart and Winston, New York, 1976.

[8] Stewart E. Barnes, Jun'ichi Ieda, and Sadamichi Maekawa. Rashba Spin-Orbit Anisotropy and the Electric Field Control of Magnetism. *Scientific Reports*, 4(1):4105, February 2014.

[9] J. V. Barth, H. Brune, G. Ertl, and R. J. Behm. Scanning tunneling microscopy observations on the reconstructed Au(111) surface: Atomic structure, long-range superstructure, rotational domains, and surface defects. *Physical Review B*, 42(15):9307–9318, November 1990. Publisher: American Physical Society.

[10] Sophie Beck and Claude Ederer. Tailoring interfacial properties in CaVO3 thin films and heterostructures with SrTiO3 and LaAlO3: A DFT+DMFT study. *Physical Review Materials*, 4(12), December 2020. Publisher: American Physical Society.

[11] Sophie Beck, Gabriele Sclauzero, Uday Chopra, and Claude Ederer. Metal-insulator transition in CaVO3 thin films: Interplay between epitaxial strain, dimensional confinement, and surface effects. *Physical Review B*, 97(7):075107, February 2018. Publisher: American Physical Society.

[12] Sanjay K. Behura, Alexis Miranda, Sasmita Nayak, Kayleigh Johnson, Priyanka Das, and Nihar R. Pradhan. Moiré physics in twisted van der Waals heterostructures of 2D materials. *Emergent Materials*, 4(4):813–826, August 2021.

[13] E.F. Bertaut and J. Dulac. Sur l'isomorphisme d'oxydes ternaires de chrome et de rhodium trivalents. *Journal of Physics and Chemistry of Solids*, 21(1-2):118–119, October 1961.

[14] Gerd Binnig and Heinrich Rohrer. Scanning tunneling microscopy—from birth to adolescence. *Reviews of Modern Physics*, 59(3):615–625, July 1987. Publisher: American Physical Society.

[15] Frank J. Blatt, Peter A. Schroeder, Carl L. Foiles, and Denis Greig. Introduction. In Frank J. Blatt, Peter A. Schroeder, Carl L. Foiles, and Denis Greig, editors, *Thermoelectric Power of Metals*. Springer US, Boston, MA, 1976.

[16] J. H. de Boer and E. J. W. Verwey. Semi-conductors with partially and with completely filled 3d-lattice bands. *Proceedings of the Physical Society*, 49(4S):59, August 1937.

[17] A. S. Botana and M. R. Norman. Electronic structure and magnetism of transition metal dihalides: Bulk to monolayer. *Physical Review Materials*, 3(4):044001, April 2019. Publisher: American Physical Society.

[18] Y. Bychkov and E. Rashba. Properties of a 2D electron gas with lifted spectral degeneracy. 1984.

[19] Yuan Cao, Valla Fatemi, Shiang Fang, Kenji Watanabe, Takashi Taniguchi, Efthimios Kaxiras, and Pablo Jarillo-Herrero. Unconventional superconductivity in magic-angle graphene superlattices. *Nature*, 556(7699):43–50, April 2018.

[20] M. Caputo, J. Jandke, E. Cappelli, S. K. Chaluvadi, E. Bonini Guedes, M. Naamneh, G. Vinai, J. Fujii, P. Torelli, I. Vobornik, A. Goldoni, P. Orgiani, F. Baumberger, M. Radovic, and G. Panaccione. Metal to insulator transition at the surface of V2O3 thin films: An *in-situ* view. *Applied Surface Science*, 574:151608, February 2022.

[21] E. Ceyhan, M. Yagmurcukardes, F. M. Peeters, and H. Sahin. Electronic and magnetic properties of single-layer FeCl 2 with defects. *Physical Review B*, 103(1):014106, January 2021.

[22] C. Julian Chen. *Introduction to Scanning Tunneling Microscopy*. Oxford University PressOxford, 2 edition, September 2007.

[23] M. Cococcioni. The LDA + U Approach : A Simple Hubbard Correction for Correlated Ground States. 2012.

[24] James W. Cooley and John W. Tukey. An algorithm for the machine calculation of complex Fourier series. *Mathematics of Computation*, 19(90):297–301, 1965.

[25] Andrea Damascelli, Zahid Hussain, and Zhi-Xun Shen. Angle-resolved photoemission studies of the cuprate superconductors. *Reviews of Modern Physics*, 75(2):473–541, April 2003.

[26] Supriyo Datta and Biswajit Das. Electronic analog of the electro-optic modulator. *Applied Physics Letters*, 56(7):665–667, February 1990.

[27] S. L. Dudarev, G. A. Botton, S. Y. Savrasov, C. J. Humphreys, and A. P. Sutton. Electron-energy-loss spectra and the structural stability of nickel oxide: An LSDA+U study. *Physical Review B*, 57(3):1505–1509, January 1998.

[28] A. Einstein. Über einen die Erzeugung und Verwandlung des Lichtes betreffenden heuristischen Gesichtspunkt. *Annalen der Physik*, 322(6):132–148, 1905. _eprint: https://onlinelibrary.wiley.com/doi/pdf/10.1002/andp.19053220607.

[29] A. Fahlman, K. Hamrin, J. Hedman, R. Nordberg, C. Nordling, and K. Siegbahn. Electron Spectroscopy and Chemical Binding. *Nature*, 210(5031):4–8, April 1966. Publisher: Nature Publishing Group.

[30] H. Falcón, J. A. Alonso, M. T. Casais, M. J. Martınez-Lope, and J. Sánchez-Benıtez. Neutron diffraction study, magnetism and magnetotransport of stoichiometric CaVO3 perovskite with positive magnetoresistance. *Journal of Solid State Chemistry*, 177(9):3099–3104, September 2004.

[31] R.M. Feenstra, Joseph A. Stroscio, and A.P. Fein. Tunneling spectroscopy of the Si(111)2 × 1 surface. *Surface Science*, 181(1-2):295–306, March 1987.

[32] A. L. Fetter, J. D. Walecka, and Leo P. Kadanoff. *Quantum Theory of Many Particle Systems*. In *Physics Today*, volume 25, pages 54–55, November 1972. ISSN: 0031-9228, 1945-0699 Issue: 11.

[33] J. Friedel. XIV. The distribution of electrons round impurities in monovalent metals. *The London, Edinburgh, and Dublin Philosophical Magazine and Journal of Science*, 43(337):153–189, February 1952.

[34] A. K. Geim and I. V. Grigorieva. Van der Waals heterostructures. *Nature*, 499(7459):419–425, July 2013. Publisher: Nature Publishing Group.

[35] Antoine Georges, Gabriel Kotliar, Werner Krauth, and Marcelo J. Rozenberg. Dynamical mean-field theory of strongly correlated fermion systems and the limit of infinite dimensions. *Reviews of Modern Physics*, 68(1):13–125, January 1996. Publisher: American Physical Society.

[36] Paolo Giannozzi, Stefano Baroni, Nicola Bonini, Matteo Calandra, Roberto Car, Carlo Cavazzoni, Davide Ceresoli, Guido L Chiarotti, Matteo Cococcioni, Ismaila Dabo, Andrea Dal Corso, Stefano de Gironcoli, Stefano Fabris, Guido Fratesi, Ralph Gebauer, Uwe Gerstmann, Christos Gougoussis, Anton Kokalj, Michele Lazzeri, Layla Martin-Samos, Nicola Marzari, Francesco Mauri, Riccardo Mazzarello, Stefano Paolini, Alfredo Pasquarello, Lorenzo Paulatto, Carlo Sbraccia, Sandro Scandolo, Gabriele Sclauzero, Ari P Seitsonen, Alexander Smogunov, Paolo Umari, and Renata M Wentzcovitch. QUANTUM ESPRESSO: a modular and open-source software project for quantum simulations of materials. *Journal of Physics: Condensed Matter*, 21(39):395502, September 2009.

[37] A. M. Glazer. The classification of tilted octahedra in perovskites. *Acta Crystallographica Section B*, 28(11):3384–3392, 1972. _eprint: https://onlinelibrary.wiley.com/doi/pdf/10.1107/S0567740872007976.

[38] M. Golalikhani, Q. Lei, R. U. Chandrasena, L. Kasaei, H. Park, J. Bai, P. Orgiani, J. Ciston, G. E. Sterbinsky, D. A. Arena, P. Shafer, E. Arenholz, B. A. Davidson, A. J. Millis, A. X. Gray, and X. X. Xi. Nature of the metal-insulator transition in few-unit-cell-thick LaNiO3 films. *Nature Communications*, 9(1):2206, June 2018. Publisher: Nature Publishing Group.

[39] Cheng Gong, Lin Li, Zhenglu Li, Huiwen Ji, Alex Stern, Yang Xia, Ting Cao, Wei Bao, Chenzhe Wang, Yuan Wang, Z. Q. Qiu, R. J. Cava, Steven G. Louie, Jing Xia, and Xiang Zhang. Discovery of intrinsic ferromagnetism in two-dimensional van der Waals crystals. *Nature*, 546(7657):265–269, June 2017. Publisher: Nature Publishing Group.

[40] John B. Goodenough. An interpretation of the magnetic properties of the perovskite-type mixed crystals *La*1x*Sr*x*CoO*3. *Journal of Physics and Chemistry of Solids*, 6(2):287–297, August 1958.

[41] John B. Goodenough. Direct Cation- -Cation Interactions in Several Oxides. *Physical Review*, 117(6):1442–1451, March 1960.

[42] David J. Griffiths. Introduction to Electrodynamics, June 2017. ISBN: 9781108333511 Publisher: Cambridge University Press.

[43] G. Grüner. The dynamics of charge-density waves. *Reviews of Modern Physics*, 60(4):1129–1181, October 1988.

[44] Jing Gu, Yong Yan, Jason W. Krizan, Quinn D. Gibson, Zachary M. Detweiler, Robert J. Cava, and Andrew B. Bocarsly. p-Type CuRhO2 as a Self-Healing Photoelectrode for Water Reduction under Visible Light. *Journal of the American Chemical Society*, 136(3):830–833, January 2014.

[45] Qiangqiang Gu, Siyuan Wan, Qingkun Tang, Zengyi Du, Huan Yang, Qiang-Hua Wang, Ruidan Zhong, Jinsheng Wen, G. D. Gu, and Hai-Hu Wen. Directly visualizing the sign change of d-wave superconducting

gap in Bi2Sr2CaCu2O8+ by phase-referenced quasiparticle interference. *Nature Communications*, 10(1):1603, April 2019. Publisher: Nature Publishing Group.

[46] J Henk, M Hoesch, J Osterwalder, A Ernst, and P Bruno. Spin–orbit coupling in the L-gap surface states of Au(111): spin-resolved photoemission experiments and first-principles calculations. *Journal of Physics: Condensed Matter*, 16(43):7581–7597, November 2004.

[47] M. H. Hettler, M. Mukherjee, M. Jarrell, and H. R. Krishnamurthy. Dynamical cluster approximation: Nonlocal dynamics of correlated electron systems. *Physical Review B*, 61(19):12739–12756, May 2000. Publisher: American Physical Society.

[48] P. Hohenberg and W. Kohn. Inhomogeneous Electron Gas. *Physical Review*, 136(3B):B864–B871, November 1964. Publisher: American Physical Society.

[49] Stefan Hüfner. *Photoelectron spectroscopy: principles and applications*. Springer-Verlag, Berlin; New York, 1995.

[50] Masatoshi Imada, Atsushi Fujimori, and Yoshinori Tokura. Metal-insulator transitions. *Reviews of Modern Physics*, 70(4):1039–1263, October 1998. Publisher: American Physical Society.

[51] K. Ishizaka, M. S. Bahramy, H. Murakawa, M. Sakano, T. Shimojima, T. Sonobe, K. Koizumi, S. Shin, H. Miyahara, A. Kimura, K. Miyamoto, T. Okuda, H. Namatame, M. Taniguchi, R. Arita, N. Nagaosa, K. Kobayashi, Y. Murakami, R. Kumai, Y. Kaneko, Y. Onose, and Y. Tokura. Giant Rashba-type spin splitting in bulk BiTeI. *Nature Materials*, 10(7):521–526, July 2011.

[52] Anubhav Jain, Shyue Ping Ong, Geoffroy Hautier, Wei Chen, William Davidson Richards, Stephen Dacek, Shreyas Cholia, Dan Gunter, David Skinner, Gerbrand Ceder, and Kristin A. Persson. Commentary: The Materials Project: A materials genome approach to accelerating materials innovation. *APL Materials*, 1(1):011002, July 2013.

[53] Sarah Jenkins, Levente Rózsa, Unai Atxitia, Richard F. L. Evans, Kostya S. Novoselov, and Elton J. G. Santos. Breaking through the Mermin-Wagner limit in 2D van der Waals magnets. *Nature Communications*, 13(1):6917, November 2022.

[54] William Jones and Norman H. March. *Theoretical solid state physics*. Dover Publications, New York, 1985.

[55] Junjiro Kanamori. Superexchange interaction and symmetry properties of electron orbitals. *Journal of Physics and Chemistry of Solids*, 10(2):87–98, July 1959.

[56] Shawulienu Kezilebieke, Md Nurul Huda, Viliam Vaňo, Markus Aapro, Somesh C. Ganguli, Orlando J. Silveira, Szczepan Głodzik, Adam S. Foster, Teemu Ojanen, and Peter Liljeroth. Topological superconductivity in a van der Waals heterostructure. *Nature*, 588(7838):424–428, December 2020.

[57] Atta Ullah Khan, Rabih Al Rahal Al Orabi, Amir Pakdel, Jean-Baptiste Vaney, Bruno Fontaine, Régis Gautier, Jean-François Halet, Seiji Mitani, and Takao Mori. Sb Doping of Metallic CuCr2S4 as a Route to Highly Improved Thermoelectric Properties. *Chemistry of Materials*, 29(7):2988–2996, April 2017. Publisher: American Chemical Society.

[58] Nabiullah Khan, Mohd Ghayasuddin, Waseem A. Khan, Thabet Abdeljawad, and Kottakkaran Sooppy Nisar. Further extension of Voigt function and its properties. *Advances in Difference Equations*, 2020(1):229, May 2020.

[59] Dohyun Kim, Eui-Cheol Shin, Yongjoon Lee, Young Hee Lee, Mali Zhao, Yong-Hyun Kim, and Heejun Yang. Atomic-scale thermopower in charge density wave states. *Nature Communications*, 13(1):4516, August 2022. Publisher: Nature Publishing Group.

[60] P. D. C. King, R. C. Hatch, M. Bianchi, R. Ovsyannikov, C. Lupulescu, G. Landolt, B. Slomski, J. H. Dil, D. Guan, J. L. Mi, E. D. L. Rienks, J. Fink, A. Lindblad, S. Svensson, S. Bao, G. Balakrishnan, B. B. Iversen, J. Osterwalder, W. Eberhardt, F. Baumberger, and Ph. Hofmann. Large Tunable Rashba Spin Splitting of a Two-Dimensional Electron Gas in Bi 2 Se 3. *Physical Review Letters*, 107(9):096802, August 2011.

[61] W. Kohn and L. J. Sham. Self-Consistent Equations Including Exchange and Correlation Effects. *Physical Review*, 140(4A):A1133–A1138, November 1965. Publisher: American Physical Society.

[62] Y. Kohsaka, T. Machida, K. Iwaya, M. Kanou, T. Hanaguri, and T. Sasagawa. Spin-orbit scattering visualized in quasiparticle interference. *Physical Review B*, 95(11):115307, March 2017.

[63] A. A. Kordyuk, S. V. Borisenko, A. Koitzsch, J. Fink, M. Knupfer, and H. Berger. Bare electron dispersion from experiment: Self-consistent self-energy analysis of photoemission data. *Physical Review B*, 71(21):214513, June 2005. Publisher: American Physical Society.

[64] W. Koshibae, K. Tsutsui, and S. Maekawa. Thermopower in cobalt oxides. *Physical Review B*, 62(11):6869–6872, September 2000.

[65] Andreas Krönlein, Jeannette Kemmer, Pin-Jui Hsu, and Matthias Bode. Quasiparticle interference scattering of spin-polarized Shockley-like surface state electrons: Ni(111). *Physical Review B*, 89(15):155413, April 2014.

[66] Wei Ku, Tom Berlijn, and Chi-Cheng Lee. Unfolding First-Principles Band Structures. *Physical Review Letters*, 104(21):216401, May 2010. Publisher: American Physical Society.

[67] Vadym V. Kulish and Wei Huang. Single-layer metal halides MX2 (X = Cl, Br, I): stability and tunable magnetism from first principles and Monte Carlo simulations. *Journal of Materials Chemistry C*, 5(34):8734–8741, August 2017. Publisher: The Royal Society of Chemistry.

[68] K. Kurita, H. Sakabayashi, and R. Okazaki. Correlation in transport coefficients of hole-doped CuRhO single crystals. *Physical Review B*, 99(11):115103, March 2019.

[69] H. Kuriyama, M. Nohara, T. Sasagawa, K. Takubo, T. Mizokawa, K. Kimura, and H. Takagi. High-temperature thermoelectric properties of Delafossite oxide CuRh1-xMgxO2. *2006 25th International Conference on Thermoelectrics*, pages 97–98, August 2006. Conference Name: 2006 25th International Conference on Thermoelectrics ISBN: 9781424408108 Place: Vienna Publisher: IEEE.

[70] Kazuhiko Kuroki and Ryotaro Arita. “Pudding Mold” Band Drives Large Thermopower in Na_xcoo. *Journal of the Physical Society of Japan*, 76(8):083707, August 2007.

[71] Aaron D. LaLonde, Yanzhong Pei, Heng Wang, and G. Jeffrey Snyder. Lead telluride alloy thermoelectrics. *Materials Today*, 14(11):526–532, November 2011.

[72] P. A. Lee, T. M. Rice, and P. W. Anderson. Fluctuation Effects at a Peierls Transition. *Physical Review Letters*, 31(7):462–465, August 1973.

[73] Patrick A. Lee, Naoto Nagaosa, and Xiao-Gang Wen. Doping a Mott insulator: Physics of high-temperature superconductivity. *Reviews of Modern Physics*, 78(1):17–85, January 2006. Publisher: American Physical Society.

[74] Philipp Leicht, Julia Tesch, Samuel Bouvron, Felix Blumenschein, Philipp Erler, Luca Gragnaniello, and Mikhail Fonin. Rashba splitting of graphene-covered Au(111) revealed by quasiparticle interference mapping. *Physical Review B*, 90(24):241406, December 2014.

[75] Kurt Lejaeghere, Gustav Bihlmayer, Torbjörn Björkman, Peter Blaha, Stefan Blügel, Volker Blum, Damien Caliste, Ivano E. Castelli, Stewart J. Clark, Andrea Dal Corso, Stefano de Gironcoli, Thierry Deutsch, John Kay Dewhurst, Igor Di Marco, Claudia Draxl, Marcin Dułak, Olle Eriksson, José A. Flores-Livas, Kevin F. Garrity, Luigi Genovese, Paolo Giannozzi, Matteo Giantomassi, Stefan Goedecker, Xavier Gonze, Oscar Grånäs, E. K. U. Gross, Andris Gulans, François Gygi, D. R. Hamann, Phil J. Hasnip, N. A. W. Holzwarth, Diana Iuşan, Dominik B. Jochym, François Jollet, Daniel Jones, Georg Kresse, Klaus Koepernik, Emine Küçükbenli,

Yaroslav O. Kvashnin, Inka L. M. Locht, Sven Lubeck, Martijn Marsman, Nicola Marzari, Ulrike Nitzsche, Lars Nordström, Taisuke Ozaki, Lorenzo Paulatto, Chris J. Pickard, Ward Poelmans, Matt I. J. Probert, Keith Refson, Manuel Richter, Gian-Marco Rignanese, Santanu Saha, Matthias Scheffler, Martin Schlipf, Karlheinz Schwarz, Sangeeta Sharma, Francesca Tavazza, Patrik Thunström, Alexandre Tkatchenko, Marc Torrent, David Vanderbilt, Michiel J. van Setten, Veronique Van Speybroeck, John M. Wills, Jonathan R. Yates, Guo-Xu Zhang, and Stefaan Cottenier. Reproducibility in density functional theory calculations of solids. *Science*, 351(6280):aad3000, March 2016.

[76] I. Leonov, V. I. Anisimov, and D. Vollhardt. Metal-insulator transition and lattice instability of paramagnetic V2O3. *Physical Review B*, 91(19):195115, May 2015.

[77] M. E. Lines. Magnetic Properties of CoCl2 and NiCl2. *Physical Review*, 131(2):546–555, July 1963. Publisher: American Physical Society.

[78] Jian Liu, Mehdi Kargarian, Mikhail Kareev, Ben Gray, Phil J. Ryan, Alejandro Cruz, Nadeem Tahir, Yi-De Chuang, Jinghua Guo, James M. Rondinelli, John W. Freeland, Gregory A. Fiete, and Jak Chakhalian. Heterointerface engineered electronic and magnetic phases of NdNiO3 thin films. *Nature Communications*, 4(1):2714, November 2013.

[79] Shuo Liu, Mengzhao Chen, Chenguang Fu, and Tiejun Zhu. The Interplay of Magnetism and Thermoelectricity: A Review. *Advanced Physics Research*, 2(9):2300015, 2023. _eprint: https://onlinelibrary.wiley.com/doi/pdf/10.1002/apxr.202300015.

[80] Z. Q. Liu, D. P. Leusink, X. Wang, W. M. Lü, K. Gopinadhan, A. Annadi, Y. L. Zhao, X. H. Huang, S. W. Zeng, Z. Huang, A. Srivastava, S. Dhar, T. Venkatesan, and Ariando. Metal-Insulator Transition in SrTiO3 Thin Films Induced by Frozen-Out Carriers. *Physical Review Letters*, 107(14):146802, September 2011. Publisher: American Physical Society.

[81] I. Lo Vecchio, J.D. Denlinger, O. Krupin, B.J. Kim, P.A. Metcalf, S. Lupi, J.W. Allen, and A. Lanzara. Fermi Surface of Metallic ${\mathrm{V}}_{2}{\mathrm{O}}_{3}$ from Angle-Resolved Photoemission: Mid-level Filling of ${e}_{g}^{\ensuremath{\pi}}$ Bands. *Physical Review Letters*, 117(16):166401, October 2016.

[82] Georg K.H. Madsen and David J. Singh. BoltzTraP. A code for calculating band-structure dependent quantities. *Computer Physics Communications*, 175(1):67–71, July 2006.

[83] G D Mahan and J O Sofo. The best thermoelectric. *Proceedings of the National Academy of Sciences*, 93(15):7436–7439, July 1996.

[84] Ya. S. Malakhov and G. V. Samsonov. Regularities governing the thermal stability of oxides of the transition metals. *Soviet Powder Metallurgy and Metal Ceramics*, 5(12):981–986, 1966.

[85] Richard M. Martin. *Electronic Structure: Basic Theory and Practical Methods*. Cambridge University Press, 2 edition, August 2020.

[86] Daniel E. McNally, Xingye Lu, Jonathan Pelliciari, Sophie Beck, Marcus Dantz, Muntaser Naamneh, Tian Shang, Marisa Medarde, Christof W. Schneider, Vladimir N. Strocov, Ekaterina V. Pomjakushina, Claude Ederer, Milan Radovic, and Thorsten Schmitt. Electronic localization in CaVO3 films via bandwidth control. *npj Quantum Materials*, 4(1):1–7, February 2019. Publisher: Nature Publishing Group.

[87] N. D. Mermin and H. Wagner. Absence of Ferromagnetism or Antiferromagnetism in One- or Two-Dimensional Isotropic Heisenberg Models. *Physical Review Letters*, 17(22):1133–1136, November 1966.

[88] Sung-Kwan Mo. Angle-resolved photoemission spectroscopy for the study of two-dimensional materials. *Nano Convergence*, 4(1):6, March 2017.

[89] Keiji Morikawa, Fumitoshi Iga, Isao H. Inoue, Seinosuke Onari, and Yoshikazu Nishihara. Magnetic and optical properties of CaVO3-y. *Physica B: Condensed Matter*, 194-196:1205–1206, February 1994.

[90] F. J. Morin. Oxides Which Show a Metal-to-Insulator Transition at the Neel Temperature. *Physical Review Letters*, 3(1):34–36, July 1959.

[91] Simon Moser. An experimentalist's guide to the matrix element in angle resolved photoemission. *Journal of Electron Spectroscopy and Related Phenomena*, 214:29–52, January 2017.

[92] N. F. Mott and R. Peierls. Discussion of the paper by de Boer and Verwey. *Proceedings of the Physical Society*, 49(4S):72, August 1937.

[93] K. S. Novoselov, A. K. Geim, S. V. Morozov, D. Jiang, Y. Zhang, S. V. Dubonos, I. V. Grigorieva, and A. A. Firsov. Electric field effect in atomically thin carbon films. *Science (New York, N.Y.)*, 306(5696):666–669, October 2004.

[94] Sergey V. Ovsyannikov, Yury G. Zainulin, Nadezda I. Kadyrova, Alexander P. Tyutyunnik, Anna S. Semenova, Deepa Kasinathan, Alexander A. Tsirlin, Nobuyoshi Miyajima, and Alexander E. Karkin. New antiferromagnetic perovskite CaCo3V4O12 prepared at high-pressure and high-temperature conditions. *Inorganic Chemistry*, 52(20):11703–11710, October 2013.

[95] Daniela Pacilè, Claudia Cardoso, Giulia Avvisati, Ivana Vobornik, Carlo Mariani, Dario A. Leon, Pietro Bonfà, Daniele Varsano, Andrea Ferretti,

and Maria Grazia Betti. Narrowing of d bands of FeCo layers intercalated under graphene. *Applied Physics Letters*, 118(12):121602, March 2021.

[96] Wenbing Peng, Haolin Wang, Hui Lu, Lei Yin, Yue Wang, Bruno Grandidier, Deren Yang, and Xiaodong Pi. Recent Progress on the Scanning Tunneling Microscopy and Spectroscopy Study of Semiconductor Heterojunctions. *Small*, 17(50):2100655, December 2021.

[97] John P. Perdew. Density functional theory and the band gap problem. *International Journal of Quantum Chemistry*, 28(S19):497–523, 1985.

[98] John P. Perdew, Matthias Ernzerhof, and Kieron Burke. Rationale for mixing exact exchange with density functional approximations. *The Journal of Chemical Physics*, 105(22):9982–9985, December 1996.

[99] L. Petersen and P. Hedegård. A simple tight-binding model of spin–orbit splitting of *sp*-derived surface states. *Surface Science*, 459(1):49–56, July 2000.

[100] L. Petersen, Ph. Hofmann, E. W. Plummer, and F. Besenbacher. Fourier Transform–STM: determining the surface Fermi contour. *Journal of Electron Spectroscopy and Related Phenomena*, 109(1):97–115, August 2000.

[101] Gianluca Prandini, Antimo Marrazzo, Ivano E. Castelli, Nicolas Mounet, and Nicola Marzari. Precision and efficiency in solid-state pseudopotential calculations. *npj Computational Materials*, 4(1):1–13, December 2018.

[102] PubChem. Iron(II) chloride, anhydrous, beads, -10 mesh, 99.99% trace metals basis.

[103] Shriram Ramanathan. Mott Memory and Neuromorphic Devices. *Proceedings of the IEEE*, 103(8):1289–1310, August 2015.

[104] F. Reinert, G. Nicolay, S. Schmidt, D. Ehm, and S. Hüfner. Direct measurements of the L -gap surface states on the (111) face of noble metals by photoelectron spectroscopy. *Physical Review B*, 63(11):115415, March 2001.

[105] A I Romanenko, G E Chebanova, Tingting Chen, Wenbin Su, and Hongchao Wang. Review of the thermoelectric properties of layered oxides and chalcogenides. *Journal of Physics D: Applied Physics*, 55(14):143001, April 2022.

[106] James M. Rondinelli and Nicola A. Spaldin. Structure and Properties of Functional Oxide Thin Films: Insights From Electronic-Structure Calculations. *Advanced Materials*, 23(30):3363–3381, 2011. _eprint: https://onlinelibrary.wiley.com/doi/pdf/10.1002/adma.201101152.

[107] Pedram Roushan, Jungpil Seo, Colin V. Parker, Y. S. Hor, D. Hsieh, Dong Qian, Anthony Richardella, M. Z. Hasan, R. J. Cava, and Ali Yazdani. Topological surface states protected from backscattering by chiral spin tex-

ture. *Nature*, 460(7259):1106–1109, August 2009. Publisher: Nature Publishing Group.

[108] Sindhunil Barman Roy. *Mott Insulators: Physics and applications*. IOP Publishing, July 2019.

[109] W. Schnelle, A. Leithe-Jasper, M. Schmidt, H. Rosner, H. Borrmann, U. Burkhardt, J. A. Mydosh, and Y. Grin. Itinerant iron magnetism in filled skutterudites CaFeSb12 and YbFe4Sb12: Stable divalent state of ytterbium. *Physical Review B*, 72(2):020402, July 2005.

[110] Werner W. Schulz, Philip B. Allen, and Nandini Trivedi. Hall coefficient of cubic metals. *Physical Review B*, 45(19):10886–10890, May 1992.

[111] Julian Schwinger. On the Green's functions of quantized fields. I. *Proceedings of the National Academy of Sciences*, 37(7):452–455, July 1951. Publisher: Proceedings of the National Academy of Sciences.

[112] Gabriele Sclauzero, Krzysztof Dymkowski, and Claude Ederer. Tuning the metal-insulator transition in d1 and d2 perovskites by epitaxial strain: A first-principles-based study. *Physical Review B*, 94(24), December 2016. Publisher: American Physical Society.

[113] M. P. Seah and W. A. Dench. Quantitative electron spectroscopy of surfaces: A standard data base for electron inelastic mean free paths in solids. *Surface and Interface Analysis*, 1(1):2–11, February 1979.

[114] Paolo Sessi, Felix Reis, Thomas Bathon, Konstantin A. Kokh, Oleg E. Tereshchenko, and Matthias Bode. Signatures of Dirac fermion-mediated magnetic order. *Nature Communications*, 5(1):5349, October 2014.

[115] Zewei Shao, Xun Cao, Hongjie Luo, and Ping Jin. Recent progress in the phase-transition mechanism and modulation of vanadium dioxide materials. *NPG Asia Materials*, 10(7):581–605, July 2018.

[116] S. Shibasaki, W. Kobayashi, and I. Terasaki. Transport properties of the delafossite Rh oxide Cu1-xAgxRh1-yMgyO2: Effect of Mg substitution on the resistivity and Hall coefficient. *Physical Review B*, 74(23):235110, December 2006.

[117] D. A. Shirley. High-Resolution X-Ray Photoemission Spectrum of the Valence Bands of Gold. *Physical Review B*, 5(12):4709–4714, June 1972.

[118] John G. Simmons. Generalized Formula for the Electric Tunnel Effect between Similar Electrodes Separated by a Thin Insulating Film. *Journal of Applied Physics*, 34(6):1793–1803, June 1963.

[119] Saumitra Singh, Mohd. Rahil Hasan, Pradakshina Sharma, and Jagriti Narang. Graphene nanomaterials: The wondering material from synthesis to applications. *Sensors International*, 3:100190, January 2022.

[120] J. C. Slater. The Theory of Complex Spectra. *Physical Review*, 34(10):1293–1322, November 1929. Publisher: American Physical Society.

[121] P. T. Sprunger, L. Petersen, E. W. Plummer, E. Lægsgaard, and F. Besenbacher. Giant Friedel Oscillations on the Beryllium(0001) Surface. *Science*, 275(5307):1764–1767, March 1997. Publisher: American Association for the Advancement of Science.

[122] G. R. Stewart. Non-Fermi-liquid behavior in d- and f-electron metals. *Reviews of Modern Physics*, 73(4):797–855, October 2001. Publisher: American Physical Society.

[123] Zeliang Sun, Honghui Wang, Aifeng Wang, Bin Lei, Weizhuang Zhuo, Fanghang Yu, Xiaoyuan Zhou, Jianjun Ying, Ziji Xiang, Tao Wu, and Xianhui Chen. Large Thermopower Enhanced by Spin Entropy in Antiferromagnet EuMnSb $_2$. *Advanced Functional Materials*, 32(33):2202188, August 2022.

[124] Louis Taillefer. Scattering and Pairing in Cuprate Superconductors. *Annual Review of Condensed Matter Physics*, 1(1):51–70, August 2010.

[125] Maximilian Thees, Min-Han Lee, Rosa Luca Bouwmeester, Pedro H. Rezende-Gonçalves, Emma David, Alexandre Zimmers, Franck Fortuna, Emmanouil Frantzeskakis, Nicolas M. Vargas, Yoav Kalcheim, Patrick Le Fèvre, Koji Horiba, Hiroshi Kumigashira, Silke Biermann, Juan Trastoy, Marcelo J. Rozenberg, Ivan K. Schuller, and Andrés F. Santander-Syro. Imaging the itinerant-to-localized transmutation of electrons across the metal-to-insulator transition in V $_2$ O $_3$. *Science Advances*, 7(45):eabj1164, November 2021.

[126] J. Gethyn Timothy. Microchannel plates for photon detection and imaging in space. In Martin C. E. Huber, Anuschka Pauluhn, J. Len Culhane, J. Gethyn Timothy, Klaus Wilhelm, and Alex Zehnder, editors, *Observing Photons in Space: A Guide to Experimental Space Astronomy*, pages 391–421. Springer, New York, NY, 2013.

[127] Sarah A. Tolba, Kareem M. Gameel, Basant A. Ali, Hossam A. Almossalami, and Nageh K. Allam. The DFT+U: Approaches, Accuracy, and Applications. In *Density Functional Calculations - Recent Progresses of Theory and Application*. IntechOpen, May 2018.

[128] S. Tougaard. Practical algorithm for background subtraction. *Surface Science*, 216(3):343–360, June 1989.

[129] Fabien Tran, Peter Blaha, Karlheinz Schwarz, and Pavel Novák. Hybrid exchange-correlation energy functionals for strongly correlated electrons: Applications to transition-metal monoxides. *Physical Review B*, 74(15):155108, October 2006.

[130] Evgeny Y. Tsymbal. Electric toggling of magnets. *Nature Materials*, 11(1):12–13, January 2012.

[131] Hidetomo Usui, Ryotaro Arita, and Kazuhiko Kuroki. First-principles study on the origin of large thermopower in hole-doped LaRhO and CuRhO. *Journal of Physics: Condensed Matter*, 21(6):064223, January 2009. Publisher: IOP Publishing.

[132] Hidetomo Usui, Kazuhiko Kuroki, Seiya Nakano, Kazutaka Kudo, and Minoru Nohara. Pudding-Mold-Type Band as an Origin of the Large Seebeck Coefficient Coexisting with Metallic Conductivity in Carrier-Doped FeAs and PtSe. *Journal of Electronic Materials*, 43(6):1656–1661, June 2014.

[133] János Végh. The Shirley background revised. *Journal of Electron Spectroscopy and Related Phenomena*, 151(3):159–164, May 2006.

[134] Yayu Wang, Nyrissa S. Rogado, R. J. Cava, and N. P. Ong. Spin entropy as the likely source of enhanced thermopower in NaxCo2O4. *Nature*, 423(6938):425–428, May 2003.

[135] Zhiliang Wang, Rijia Lin, Yuning Huo, Hexing Li, and Lianzhou Wang. Formation, Detection, and Function of Oxygen Vacancy in Metal Oxides for Solar Energy Conversion. *Advanced Functional Materials*, 32(7):2109503, 2022. _eprint: https://onlinelibrary.wiley.com/doi/pdf/10.1002/adfm.202109503.

[136] Peng Wei, Sujit Manna, Marius Eich, Patrick Lee, and Jagadeesh Moodera. Superconductivity in the Surface State of Noble Metal Gold and its Fermi Level Tuning by EuS Dielectric. *Physical Review Letters*, 122(24):247002, June 2019.

[137] M. K. Wilkinson, J. W. Cable, E. O. Wollan, and W. C. Koehler. Neutron Diffraction Investigations of the MagneticOrdering in FeBr2, CoBr2, FeCl2, and CoCl2. *Physical Review*, 113(2):497–507, January 1959. Publisher: American Physical Society.

[138] W. D. Wise, M. C. Boyer, Kamalesh Chatterjee, Takeshi Kondo, T. Takeuchi, H. Ikuta, Yayu Wang, and E. W. Hudson. Charge-density-wave origin of cuprate checkerboard visualized by scanning tunnelling microscopy. *Nature Physics*, 4(9):696–699, September 2008. Publisher: Nature Publishing Group.

[139] Ian T. Witting, Thomas C. Chasapis, Francesco Ricci, Matthew Peters, Nicholas A. Heinz, Geoffroy Hautier, and G. Jeffrey Snyder. The Thermoelectric Properties of Bismuth Telluride. *Advanced Electronic Materials*, 5(6):1800904, June 2019.

[140] D. P. Woodruff, W. A. Royer, and N. V. Smith. Empty surface states, image states, and band edge on Au(111). *Physical Review B*, 34(2):764–767, July 1986.

[141] R. Patrick Xian, Vincent Stimper, Marios Zacharias, Maciej Dendzik, Shuo Dong, Samuel Beaulieu, Bernhard Schölkopf, Martin Wolf, Laurenz Rettig, Christian Carbogno, Stefan Bauer, and Ralph Ernstorfer. A machine learning route between band mapping and band structure. *Nature Computational Science*, 3(1):101–114, January 2023. Publisher: Nature Publishing Group.

[142] Ying-Ming Xie, K. T. Law, and Patrick A. Lee. Topological superconductivity in EuS/Au/superconductor heterostructures. *Physical Review Research*, 3(4):043086, October 2021. Publisher: American Physical Society.

[143] Kaijie Yang, Zian Xu, Yanjie Feng, Frank Schindler, Yuanfeng Xu, Zhen Bi, B. Andrei Bernevig, Peizhe Tang, and Chao-Xing Liu. Topological minibands and interaction driven quantum anomalous Hall state in topological insulator based moiré heterostructures. *Nature Communications*, 15(1):2670, March 2024.

[144] T. Yoshida, M. Kobayashi, K. Yoshimatsu, H. Kumigashira, and A. Fujimori. Correlated electronic states of SrVO3 revealed by angle-resolved photoemission spectroscopy. *Journal of Electron Spectroscopy and Related Phenomena*, 208:11–16, April 2016.

[145] K. Yoshimatsu, T. Okabe, H. Kumigashira, S. Okamoto, S. Aizaki, A. Fujimori, and M. Oshima. Dimensional-crossover-driven metal-insulator transition in SrVO3 ultrathin films. *Physical Review Letters*, 104(14), April 2010.

[146] Claudio Zeni, Robert Pinsler, Daniel Zügner, Andrew Fowler, Matthew Horton, Xiang Fu, Sasha Shysheya, Jonathan Crabbé, Lixin Sun, Jake Smith, Bichlien Nguyen, Hannes Schulz, Sarah Lewis, Chin-Wei Huang, Ziheng Lu, Yichi Zhou, Han Yang, Hongxia Hao, Jielan Li, Ryota Tomioka, and Tian Xie. MatterGen: a generative model for inorganic materials design, January 2024. arXiv:2312.03687 [cond-mat].

[147] Lei Zhang, Yuanjun Zhou, Lu Guo, Weiwei Zhao, Anna Barnes, Hai-Tian Zhang, Craig Eaton, Yuanxia Zheng, Matthew Brahlek, Hamna F. Haneef, Nikolas J. Podraza, Moses H. W. Chan, Venkatraman Gopalan, Karin M. Rabe, and Roman Engel-Herbert. Correlated metals as transparent conductors. *Nature Materials*, 15(2):204–210, February 2016.

[148] J. Zhou and J. B. Goodenough. Heterogeneous electronic structure in CaVO3. *Physical Review. B, Condensed Matter*, 54(19):13393–13397, November 1996.

[149] Xuhan Zhou, Bartosz Brzostowski, Artur Durajski, Meizhuang Liu, Jin Xiang, Tianran Jiang, Zhiqiang Wang, Shenwei Chen, Peigen Li, Zhihao Zhong, Andrzej Drzewiński, Marcin Jarosik, Radosław Szczęśniak, Tianshu Lai, Donghui Guo, and Dingyong Zhong. Atomically Thin 1T-FeCl $_2$

Grown by Molecular-Beam Epitaxy. *The Journal of Physical Chemistry C*, 124(17):9416–9423, April 2020.

List of Tables

5.1 Extracted absolute values of v$_F$ from linear fits in the range of 0.14 eV below E$_F$ 53
5.2 XPS fit parameters for V 2p and O 1s peaks for the 90 u.c, 45 u.c. and 15 u.c. samples 54

6.1 Surface state band parameters extracted from ARPES and QPI 75

List of Figures

2.1 a) Schematic of band formation going from an isolated atom to a solid. Left : electronic energy levels for an isolated atom, while right shows formations of bands with broad energy states as atoms come close together. Adapted from [7]. b) Band structure of a 1-D atomic chain in the tight-binding model. c) Band structure of a 1-D atomic chain modified by a staggered potential. 4

2.2 a) Cartoon representation of a half-filled Hubbard model. Left depicts the case of weak Hubbard interaction term U compared to hopping t, and right depicts the case of strong correlations. Electrons are indicated by the red balls. b) Schematic phase diagram of a cuprate superconductor as a function of hole doping p and temperature T. From [124]. 7

2.3 Schematic of band dispersion : a) for a free electron and with Rashba SOC ; b) in-plane spin-momentum texture in a Rashba-split band. Arrows indicate electron spin direction. 9

2.4 From [85]. Schematic illustration of the self-consistent procedure for solving the Kohn-Sham equations. 11

2.5 Density of states (DOS) calculated by LDA and LDA+U for (a) MnO and (b) FeO. Notice the opening of the band gap in LDA+U. Adapted from [129]. 13

3.1 a) Cartoon representation of Einstein's photoelectric effect. b) Schematic of the three-step model of photoemission, adapted from [49]. 18

3.2 Representation of the excitation of an electron in a material with binding energy E_B to some kinetic energy E_{kin} by a photon with energy $h\nu$. From [49]. 19

3.3 a) Geometry of the ARPES setup. θ and ϕ angles define the angle of emitted photoelectrons. $A_{\parallel}$ and $A_{\perp}$ are the parallel and perpendicular components of **A**, respectively, with respect to the mirror plane. b) Top-down view of the sample with the symmetry of the d$_{xy}$ orbital with respect to the mirror plane (M.P.). c) Momentum space schematic of the Fermi surface of $SrVO_3$. The blue circle corresponds to the contribution of the d$_{xy}$ orbital and would change intensity depending on the light polarization direction in b. 21

3.4 a) Schematic of a single-band non-interacting system. b) Schematic of an interacting Fermi liquid system. Bottom right : Photoelectron spectrum of gaseous hydrogen (black) and ARPES spectrum of solid hydrogen (red). Adapted from [25]. 22

3.5 Compilation of inelastic mean free path of various materials. Blue bar indicates typical operating energy in ARPES experiments. Adapted from [113]. 23

3.6 a) Map of synchrotron SOLEIL with the location of various beamlines and insertion devices indicated. b) Schematic of a beamline ARPES setup with an analyzer sensitive to both energy and angle information simultaneously. Adapted from [25]. 26

3.7 a) A typical kinetic energy–angle dispersion raw data acquired by ARPES. The horizontal and vertical lines represent the MDC and EDC slices shown on the right. b) The same data normalized along the EDC slices. c) The raw data processed to show second derivative intensity peaks along the angular direction. 28

3.8 Scanning tunneling microscope in a nutshell. From [22] 29

3.9 a) Constant current and b) constant height operating modes of STM/STS. c) Schematic of STS measurements. The sample is polarized with respect to the tip which is grounded. Adapted from [96] 30

3.10 dI/dV images and their FT for the Au(111) surface at a) -200 meV, b) 50 meV, and c) 400 meV. Adapted from [114]. d) **q**-E dispersion extracted from the Au(111) surface. (See Chapter 6) 32

4.1 Schematic for a metallic and pudding mold-type band. v$_A$ and v$_B$ represent the band velocities above and below the Fermi level in the highlighted red region of width 2k$_B$T. 36

4.2 Schematic representation of possible states in Co^{3+} and Co^{4+} ions in the material NaCo$_2$O$_4$. The number in the box represents the total possible degenerate states corresponding to the configuration represented. From [64]. 38

4.3 a) Conventional hexagonal unit cell of CuRhO$_2$. Red, blue and grey atoms represent O, Cu and Rh respectively. b) Primitive Brillouin zone of CuRhO$_2$. High symmetry points and the path connecting them are indicated. 39

4.4 Constant energy maps at a) 0eV, b) -0.1eV, c) -0.3eV, and d)-0.4eV relative to Fermi level. Data was taken at s-polarization and 182 eV photon energy. The Brillouin zone is overlaid in red in a. . . 40

4.5 a) In-plane band cut at 542 eV photon energy overlaid with calculated bands at $k_z = \Gamma$ in red. b) In-plane band cut at 590 eV photon energy overlaid with calculated bands at $k_z = Z$ in red. c) Out of plane Fermi surface along $k_z - k_x$ axis, spanning the Γ11 (538 eV photon energy) and Z11 (590 eV photon energy) high symmetry points. The black dotted lines are positions of high symmetry points along k_z. d) Second derivative along energy of the energy-momentum dispersion along k_z at normal emission. Solid red lines are the calculated bands and dotted red lines is the experimental fit. In panels c and d, the data was obtained using photons in the range of $500 - 620$eV. Γ11 is calculated to lie at 538 eV by fitting with the k_z measurement and using an inner potential 3.15 of 23.5 eV in the three step model approximation [49]. 41

4.6 Left : Orbital project bands of CRMO (with the Fermi level set shifted to -0.06 eV from the top of the valence band) with orbital weights indicated by the size of colored circles. Right : Orbital project density of states (DOS). Inlaid : Closer view of the DOS near the Fermi level which shows that the density of Rh t$_{2g}$ orbitals and Cu d$_{z^2}$ orbitals is similar at the Fermi level. 42

4.7 The S$_{xx}$ and S$_{zz}$ components of the calculated Seebeck coefficient S vs temperature T for the undoped sample and the 10% doped sample. Experimental data from [69] and [68] are compared to the calculations of doped Seebeck coefficient. 43

5.1 Crystal lattice for a perfect perovskite structure along the a) in-plane and b) out-of-plane directions. Crystal lattice for CaVO$_3$ along the c) in-plane and d) out-of-plane directions. The unit cell is represented by black lines. Green, silver, and red spheres represent Ca, V, and O, respectively. The V-O octahedra are represented by the silver polygons. e) Θ and Φ represent O-O-O and V-O-V angles used to characterize tilts. Adapted from [11]. f) Schematic showing tensile strain direction due to lattice mismatch between SrTiO$_3$ and CaVO$_3$. 49

5.2 a) Fermi surface of SrVO$_3$, an example of a perfect pervoskite crystal. b) Fermi surface of CaVO$_3$. c) In-plane Fermi surface of SrVO$_3$ at k$_z$=0 plane. Schematic d$_{xy}$, d$_{xz}$ and d$_{yz}$ are represented by dotted lines. d) Fermi surface of CaVO$_3$ along k$_{<100>}$ - k$_{<010>}$ plane at k$_{<001>}$=0. e) Fermi surface of CaVO$_3$ along k$_{<100>}$ - k$_{<001>}$ plane at k$_{<010>}$=0. Black solid line represents the actual BZ boundaries of CaVO$_3$ while black dotted line represents the Fermi surface boundaries of the unfolded 1×1×1 BZ. Band dispersion of CaVO$_3$ calculated along f) k$_{<100>}$ passing through Γ and g) k$_{<001>}$ passing through Γ. Red lines represent the DFT calculated bands and the intensity of unfolded bands to 1×1×1 periodicity is represented in black. X', Y' and Z' are the corresponding high symmetry points in the 1×1×1 BZ. h) Band dispersion along k$_x$ through Γ for SrVO$_3$. 58

5.3 a) Out-of-plane constant energy surface of the 90 u.c. film along k$_{<001>}$ - k$_{<100>}$ at Fermi level and -0.35 eV from Fermi level. b) Band dispersion along k$_{<001>}$ at k$_{<100>}$ $= 0$. All measurements are done with s-polarized light. 59

5.4 a) Fermi surface of the 90 u.c. sample along k$_{<100>}$ - k$_{<010>}$ plane d) Fermi surface of the 45 u.c. sample along k$_{<100>}$ - k$_{<010>}$ plane. d) Band dispersion along cuts A and B indicated in the Fermi surface plots. All measurements are done with s-polarized light at $h\nu$ = 82 eV. 59

5.5 Fermi surface on the k$_{<100>}$ - k$_{<010>}$ plane for a) 30 u.c. sample and b) 20 u.c. sample. c) In-plane Fermi surface of the 45° rotated 30 u.c. sample. Lines 1 and 2 are used to estimate the BZ size. Fermi surfaces were taken at $h\nu$= 82 eV with s-polarized light. 60

5.6 Band dispersion along k$_{<100>}$ at k$_{<010>}$ = 0 for a) 30 u.c. sample and d) 20 u.c. sample. Peak positions from lorrentzian fits of MDC are overlaid with red points. Extracted Lorentzian peaks and broadening (full width at half maxima (FWHM)) represented by error bars for b) 30 u.c. sample and e) 20 u.c. sample. Associated FHWM as a function of energy for extracted bands for c) 30 u.c. sample and f) 20 u.c. sample. Yellow translucent regions indicate region of sudden increase in broadening of Lorentzian peaks. Band dispersions were taken at 82 eVt. Band dispersion along k$_{<100>}$ at k$_{<010>}$ for the 90 u.c. sample at g) 88 eV (bulk Γ) and h) 77 eV ($\Gamma - 0.35BZ$). All measurements were done with s-polarized light. 61

5.7 Extracted Lorentzian peaks and linear fits for the 90 u.c., 45 u.c., 30 u.c. and 25 u.c. sample dispersion at 82 eV. The peaks from different samples are shifted along k$_{<100>}$ for better visualization. 62

5.8 a) Dispersion along k$_{<100>}$ at k$_{<010>}$ = 0 for the 90 u.c. and 15 u.c. samples along with the momentum integrated EDC. b) Integrated EDCs of the 90 u.c, 45 u.c. and 15 u.c. samples in the energy region of the Hubbard band and the quasiparticle peak near Fermi level. All measurements were taken with s-polarized photons at $h\nu$ = 82 eV. 62

5.9 XPS BE measurements for a) 90 u.c., b) 45 u.c. and c) 15 u.c. sample with Voigt peaks fitted to O1s and V 2p$_{3/2}$ peaks. Green dotted line indicates the Shirley type background which is subtracted before fitting procedure. d) XPS BE measurements in the range of 505 eV to 540 eV for the 90 u.c., 45 u.c. and 15 u.c. samples. Inset shows Ca 2s peak used to calibrate binding energy of the insulating 15 u.c. sample. 63

5.10 Band structure calculations for a)1×1 unit cell of a nearest neighbour 1-band tight binding model b) 4×4 SC and c) 16×16 SC. The BZ is seen to be shrinking for larger SCs. d) DOS plot for the system. From [66]. 63

6.1 a) Side and b) top view of FeCl$_2$ unit cell. c) Trigonal distortion (TD) of the FeCl$_2$ octahedra represented by elongation and contraction along the A and B axes, respectively. d) Schematic of energy levels of the occupied Fe 3d t$_{2g}$ states in the presence of TD and SOC. Adapted from [17]. 66

6.2 a) LEED pattern for 0.5 ML FeCl$_2$/Au(111) at 71 eV and 137 eV. Hexagonal spots from Au(111) and FeCl$_2$ are drawn. b), c) Topographical images in a 0.5 μm × 0.5 μm region for the 0.5 ML FeCl$_2$/Au(111) (V$_b$ = 1.6 V, I$_t$ = 10 pA). Numbered line profiles are shown in the inset. d) A 10 nm × 10 nm topographical image of the FeCl$_2$ ML with the surface modulation shown in the inset (V$_b$ = 3 mev, I$_t$ = 300 pA). e) Small scale topographical image of the FeCl$_2$ ML with the unit cell drawn on (V$_b$ = 3 mev, I$_t$ = 300 pA). . . 68

6.3 ARPES measurements at 30K with $C+$ polarized photons with photon energy of a) 14 eV, b) 17 eV, c) 21 eV, d) 24 eV, e) 27 eV, and f) 30 eV. Dotted red line is overlaid on FeCl$_2$ valence band maxima. g) Angle-integrated EDCs of the ARPES measurements at different energies. Transparent red region indicates the position of FeCl$_2$ valence band. 69

6.4 a) 2-D Brillouin zone (BZ) of the ML $FeCl_2$ unit cell. b) Ferromagnetic band structure in the absence of SOC and Hubbard U. c) Band structure with SOC and U included. d) Orbital and spin-projected DOS of the $FeCl_2$ ML. 70

6.5 a) Topographical image and b) dI/dV map of 1 ML $FeCl_2$ (V_b = 1.5 V, I_t = 50 pA) . Red and blue dots represent spots for STS point spectra at the $FeCl_2$ layer and Au(111) surface respectively. c) STS at bright spots in dI/dV map at 1.5 eV. d) STS at dark spots in dI/dV map at 1.5 eV. e) STS at points on Au(111) surface. f) Averaged STS profiles for bright, dark and Au spots from c,d and e. 72

6.6 a) Topographical image showing the $FeCl_2$ ML island (V_B = -0.45 e V, I_t = 50 pA) STM dI/dV map at 75 meV acquired in the same region as (a) . c) QPI maps obtained by Fourier transform of the dI/dV maps at 25 meV, 200 meV and 475 meV for the isolated $FeCl_2$ ML. Red and yellow dashed lines are guides for the observed scattering vector **q**. Dispersion relation between **q** and energy E obtained by radial integration of QPI maps for d) $FeCl_2$ ML in a small energy range around E_F, e) $FeCl_2$ ML in a wider energy range and f) Au(111) surface. MDC cuts for **q**-E dispersion in g) d and h) e at different energies. 73

6.7 a) Extracted peaks for Au SS and $FeCl_2$ α and β bands from QPI dispersion. b) STM extracted peaks overlaid on ARPES data for 0.5 ML $FeCl_2$/ Au(111). The data was obtained at temperature T= 16 K and photon energy hν = 17 eV. c) EDC obtained by integrating the ARPES dispersion in a region of 0.05 Å $^{-1}$ around $k_{\|} = 0$. 74

6.8 Topographical image at a) V_B = -0.15 eV (I_t = 50 pA) and b) V_B = 0.075 eV ((I_t = 50 pA). c) Small scale atomic resolution topographical image. The numbered line segments are plotted between nearest neighbour defects and are used to calculate average defect distance (V_b = 3 meV, I_t = 500 pA. d) Scattering wave vector **q** obtained by Fourier transform of topographical image in the same region as a) and b) for different energies. e) MDC cuts for d at different energies. Blue region indicates peaks associated with defects in topography. 76

6.9 a) **q**-E dispersion of $FeCl_2$ ML in a wide energy range. b) Intensity plot after taking second derivatives of a along momentum **q**. c) Peak positions in second derivative plot for α and β bands extracted from b and converted into k-space. 77

6.10 a)Effect of adding spin–orbit interactions and weaker and stronger Zeeman-type magnetization are shown. Adapted from [56]. b) Inter-band and intra-band scattering in Rashba spin-split bands of BiTeI. Adapted from [62]. 78

6.11 Calculated DOS for 6×6 unit cell with Fe defect. Notice that only the Cl states close to defect sites cross the Fermi level. 79

6.12 a) Averaged STS from bright spots on FeCl_2 in 6.5 b. Peaks are indexed by best fit quantum well states. b) $E \sim n^2$ plot. c) $E \sim n$ plot. E_0 is set to 0.6 eV. Blue dots represent data points and dashed red line is the linear fit. 80

6.13 Moiré modulation on ML FeCl_2/Bi_2Se_3 heterostructure (V_b = -1 V, I_t = 50 pA). The Moiré cell is drawn with the lattice constant of 2.6 nm. 80

6.14 a) Schematic of direct and superechange interaction in a transition metal dihalide MX_2. b) M-X-M superexchange interaction for 90 ° bond angle. Adapted from [67]. 81

7.1 a) Schematic for a metallic and pudding mold type band. v_A and v_B represent the band velocities above and below the Fermi level in the highlighted red region of width $2k_BT$. b) In-plane band cut at 542 eV ($k_z = \Gamma$) and at 590 eV photon energy ($k_z = Z$), overlaid with calculated bands in red. c) Primitive Brillouin zone of CuRhO_2. High symmetry points and the path connecting them are indicated. d) The S_{xx} and S_{zz} components of the calculated Seebeck coefficient vs temperature level for the undoped sample and the 10% doped sample. Experimental data from [69] and [68] are compared to the calculations of doped Seebeck coefficient. 113

7.2 a) Fermi surface on the $k_{<100>}$ - $k_{<010>}$ plane for the 30 u.c. sample. b) Integrated EDCs of the 90 u.c, 45 u.c. and 15 u.c. samples in the energy region of the Hubbard band and the quasiparticle peak near Fermi level. All measurements were taken with s-polarized photons at $h\nu$ = 82 eV. c) XPS BE measurements in the range of 505 eV to 540 eV for the 90 u.c., 45 u.c. and 15 u.c. samples. Inset shows Ca 2s peak used to calibrate binding energy of the insulating 15 u.c. sample. d) Extracted Lorentzian peaks and linear fits for the 90 u.c., 45 u.c., 30 u.c. and 25 u.c. sample dispersion at 82 eV. The peaks from different samples are shifted along $k_{<100>}$ for better visualization. 114

7.3 a) QPI maps obtained by Fourier transform of the dI/dV maps at 25 meV, 200 meV and 475 meV for the isolated FeCl$_2$ ML. Red and yellow dashed lines are guides for the observed scattering vector **q**. Dispersion relation between **q** and energy E obtained by radial integration of QPI maps for b) FeCl$_2$ ML in a small energy range around E$_F$, c) FeCl$_2$ ML in a wider energy range. d) Extracted peaks for Au SS and FeCl$_2$ α and β bands from QPI dispersion. e) Peak positions in second derivative plot for α and β bands extracted from c and converted into k-space. f) dI/dV map of 1 ML FeCl$_2$ (V$_b$ = 1.5 V, I = 50 pA). Red and blue dots represent spots for STS point spectra at the FeCl$_2$ layer and Au(111) surface respectively. g) Averaged STS profiles for bright, dark and Au spots from f. 117

8.1 a) Schéma pour une bande métallique et de type pudding mold. v$_A$ et v$_B$ représentent les vitesses des bandes au-dessus et en dessous du niveau de Fermi dans la région rouge mise en évidence de largeur 2kBT. b) Coupe de bande dans le plan à 542 eV ($k_z = \Gamma$) et à 590 eV d'énergie photonique ($k_z = Z$), superposée avec les bandes calculées en rouge. c) Zone de Brillouin primitive de CuRhO2. Les points de haute symétrie et le chemin les reliant sont indiqués. d) Les composantes S$_{xx}$ et S$_{zz}$ du coefficient Seebeck calculé en fonction de la température pour l'échantillon non dopé et l'échantillon dopé à 10$\%$. Les données expérimentales de [69] et [68] sont comparées aux calculs du coefficient Seebeck dopé. 124

8.2 a) Surface de Fermi dans le plan k$_{<100>}$ - k$_{<010>}$ pour l'échantillon de 30 u.c. b) EDCs intégrées des échantillons de 90 u.c., 45 u.c. et 15 u.c. dans la région d'énergie de la bande de Hubbard et du pic de quasi-particule près du niveau de Fermi. Toutes les mesures ont été prises avec des photons s-polarisés à $h\nu$ = 82 eV. c) Mesures XPS de l'énergie de liaison dans la gamme de 505 eV à 540 eV pour les échantillons de 90 u.c., 45 u.c. et 15 u.c. L'encart montre le pic Ca 2s utilisé pour calibrer l'énergie de liaison de l'échantillon isolant de 15 u.c. d) Pics lorentziens extraits et ajustements linéaires pour la dispersion des échantillons de 90 u.c., 45 u.c., 30 u.c. et 25 u.c. à 82 eV. Les pics des différents échantillons sont décalés le long de k$_{<100>}$ pour une meilleure visualisation. 125

8.3 a) Cartes QPI obtenues par transformée de Fourier des cartes dI/dV à 25 meV, 200 meV et 475 meV pour la monocouche isolée de FeCl_2. Les lignes pointillées rouges et jaunes sont des guides pour le vecteur de diffusion **q** observé. Relation de dispersion entre **q** et l'énergie E obtenue par intégration radiale des cartes QPI pour b) la monocouche de FeCl_2 dans une petite plage d'énergie autour de E_F, c) la monocouche de FeCl_2 dans une plage d'énergie plus large. d) Pics extraits pour l'état de surface Au SS et les bandes α et β du FeCl_2 à partir de la dispersion QPI. e) Positions des pics dans le graphique de la seconde dérivée pour les bandes α et β extraites de c et converties en espace k. f) Carte dI/dV d'une monocouche de FeCl_2 (V_b = 1,5 V, I = 50 pA). Les points rouges et bleus représentent les emplacements pour les spectres ponctuels STS à la couche FeCl_2 et à la surface Au(111) respectivement. g) Profils STS moyennés pour les zones claires, sombres et Au de f. 126

9.1 a) Esquema para una banda metálica y de tipo "pudding mold". v_A y v_B representan las velocidades de banda por encima y por debajo del nivel de Fermi en la región roja resaltada de ancho $2k_BT$. b) Corte de la banda en el plano a 542 eV ($k_z = \Gamma$) y a 590 eV de energía de fotón ($k_z = Z$), superpuesto con las bandas calculadas en rojo. c) Zona de Brillouin primitiva de CuRhO_2. Se indican los puntos de alta simetría y el camino que los conecta. d) Las componentes S_{xx} y S_{zz} del coeficiente Seebeck calculado en función del nivel de temperatura para la muestra no dopada y la muestra dopada al 10%. Los datos experimentales de [69] y [68] se comparan con los cálculos del coeficiente Seebeck dopado. 129

9.2 a) Superficie de Fermi en el plano $k_{<100>}$ - $k_{<010>}$ para la muestra de 30 u.c. b) EDCs integrados de las muestras de 90 u.c., 45 u.c. y 15 u.c. en la región de energía de la banda de Hubbard y el pico de cuasipartículas cerca del nivel de Fermi. Todas las mediciones se realizaron con fotones polarizados en s a $h\nu$ = 82 eV. c) Mediciones XPS BE en el rango de 505 eV a 540 eV para las muestras de 90 u.c., 45 u.c. y 15 u.c. El recuadro muestra el pico Ca 2s utilizado para calibrar la energía de enlace de la muestra aislante de 15 u.c. d) Picos lorentzianos extraídos y ajustes lineales para la dispersión de las muestras de 90 u.c., 45 u.c., 30 u.c. y 25 u.c. a 82 eV. Los picos de diferentes muestras se desplazan a lo largo de $k_{<100>}$ para una mejor visualización. . 130

9.3 a) Mapas de QPI obtenidos por transformada de Fourier de los mapas de dI/dV a 25 meV, 200 meV y 475 meV para la monocapa aislada de $FeCl_2$. Las líneas discontinuas rojas y amarillas son guías para el vector de dispersión q observado. Relación de dispersión entre q y la energía E obtenida mediante la integración radial de los mapas QPI para b) la monocapa de $FeCl_2$ en un rango pequeño de energía alrededor de E_F, c) la monocapa de $FeCl_2$ en un rango de energía más amplio. d) Picos extraídos para el estado superficial de Au SS y las bandas α y β de $FeCl_2$ a partir de la dispersión QPI. e) Posiciones de los picos en el gráfico de segunda derivada para las bandas α y β extraídas de c y convertidas en el espacio k. f) Mapa de dI/dV de una monocapa de $FeCl_2$ (V_b = 1.5 V, I = 50 pA). Los puntos rojos y azules representan los puntos de espectros STS en la capa $FeCl_2$ y en la superficie de Au(111), respectivamente. g) Perfiles STS promediados para las zonas claras, oscuras y de Au de f. 133

7 - Summary

7.1 . Introduction

Understanding the relationship between the atomic structure, functional properties, and electronic structure of materials is a fundamental challenge in condensed matter physics. Many of the most intriguing phenomena in materials science, such as superconductivity, magnetism, and thermoelectric effects, arise from subtle interactions between these three domains. Despite significant progress, the intricate ways in which the atomic arrangement and electronic correlations give rise to unique functional behaviors remain an open question, particularly in strongly correlated materials.

This thesis is driven by the need to deepen our understanding of how the atomic and electronic structure of materials governs their physical properties. Mg doped metallic thermoeletric CuRhO$_2$, thin films of correlated metal CaVO$_3$, and the magnetic 2-D van der Waals insulator FeCl$_2$ on Au(111) have been selected as case studies for their rich electronic behavior and potential applications in thermoelectrics, quantum devices, and spintronics. Each of these materials exhibits complex interactions between their atomic configurations and electronic structure, providing ideal platforms to explore how subtle modifications—such as doping, dimensionality reduction, or external stimuli—can drastically alter their functional properties.

7.2 . Theoretical and experimental background

The theoretical framework of this thesis is centered on understanding the formation of electronic bands and the impact of electron correlations in strongly correlated materials. Using the tight-binding model, we describe how atomic orbitals in a crystal lattice overlap to form energy bands. The introduction of electron-electron interactions through the Hubbard model allows us to explore how these correlations can lead to phenomena such as metal-insulator transitions and enhanced thermoelectric properties. To accurately model these effects in real materials, Density Functional Theory (DFT) is employed, with the DFT+U extension accounting for the strong electron-electron interactions typical of localized d and f orbitals. This theoretical approach enables a more precise description of electronic structure in correlated systems, where conventional band theory falls short.

Experimentally, Angle-Resolved Photoemission Spectroscopy (ARPES) is used to probe the electronic band structure and Fermi surface of these materials, providing direct measurements of how correlations and structural modifications influence their electronic behavior. Scanning Tunneling Microscopy (STM) and Scanning Tunneling Spectroscopy (STS) are utilized to obtain atomic-scale resolution of surface topography and local density of states (LDOS), which are essential for studying localized electronic states, especially in low-dimensional systems like 2D metal dihalides. Quasi-Particle Interference (QPI) complements these techniques by capturing momentum-resolved information about surface states through the scattering of quasiparticles, providing additional insights into the electronic structure above the Fermi level that are not accessible through ARPES alone.

7.3 . Thermoelectricity in Mg doped CuRhO$_2$

In this chapter, we investigate the electronic structure of Mg doped CuRhO$_2$, a delafossite oxide. CuRhO$_2$ is an insulating material with a high Seebeck coefficient S. Doping the material with Mg, makes it metallic while still preserving the high S value. This behavior is unexpected as metals tend to have poor thermoelectric coefficient owing to equal mobilities of electrons and hole near the Fermi level. The thermoelectric performance of a material is characterized by the thermoelectric figure of merit $ZT = S^2\sigma T/\kappa$, where S is the Seebeck coefficient, σ is the electrical conductivity, T is the temperature, and κ is the thermal conductivity. A high Seebeck coefficient along with good electrical conductivity and low thermal conductivity are therefore critical. Doped CuRhO$_2$ which shows metallic behavior along with a high Seebeck coefficient is the perfect candidate material for potential applications in thermoelectric devices.

The "pudding-mold" band structure, with a flat dispersion just above (below) the Fermi level and a highly dispersing band just below (above) the Fermi level, plays a central role in the observed thermoelectric performance of CuRhO$_2$, as suggested by theoretical calculations. Using Angle-Resolved Photoemission Spectroscopy (ARPES), we map the band structure and observe this "pudding-mold" type band structure in metallic 10$\%$ Mg doped CuRhO$_2$. Density Functional Theory (DFT) calculations of insulating CuRhO$_2$ were performed. With a small rigid shift of -0.06 of the Fermi level, the calculated bands show an excellent match with the ARPES band structure of the doped sample. These shifted bands were then used to calculate the thermoelectric Seebeck coefficient. The calculated values of Seebeck coefficient S $\sim 256\mu$V/K doped samples at 1000 K are found to be in close agreement with the experiments.

The combination of experimental and theoretical insights leads to a comprehensive understanding of how Mg doping tunes the electronic structure of CuRhO$_2$ to enhance its thermoelectric performance. The findings of this chapter have broader implications for designing and exploring other oxide-based thermoelectric materials with this "pudding-mold" type band for thermoelec-

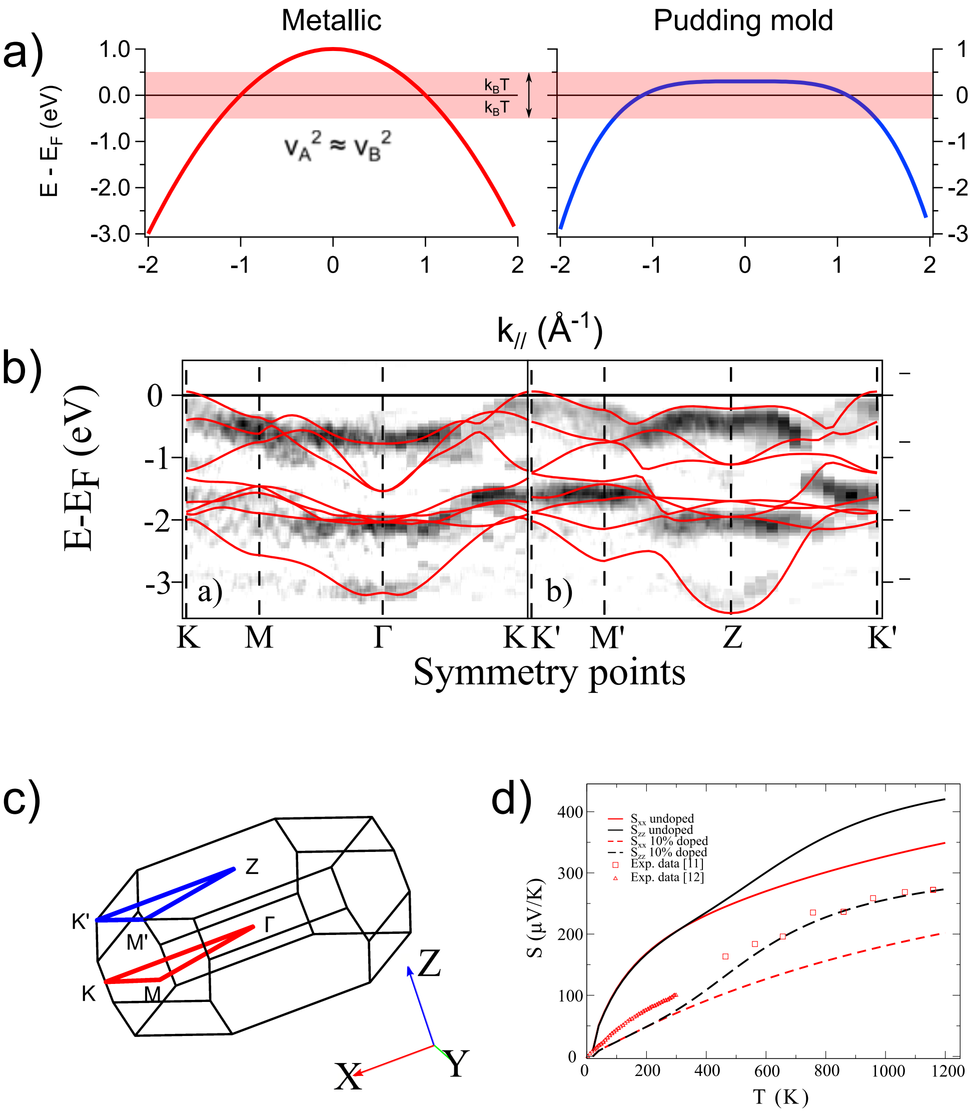

Figure 7.1 – a) Schematic for a metallic and pudding mold type band. v$_A$ and v$_B$ represent the band velocities above and below the Fermi level in the highlighted red region of width 2k$_B$T. b) In-plane band cut at 542 eV ($k_z = \Gamma$) and at 590 eV photon energy ($k_z = Z$), overlaid with calculated bands in red. c) Primitive Brillouin zone of CuRhO$_2$. High symmetry points and the path connecting them are indicated. d) The S$_{xx}$ and S$_{zz}$ components of the calculated Seebeck coefficient vs temperature level for the undoped sample and the 10% doped sample. Experimental data from [69] and [68] are compared to the calculations of doped Seebeck coefficient.

tric applications.

7.4 . Metal-Insulator Transition in thin films of CaVO$_3$

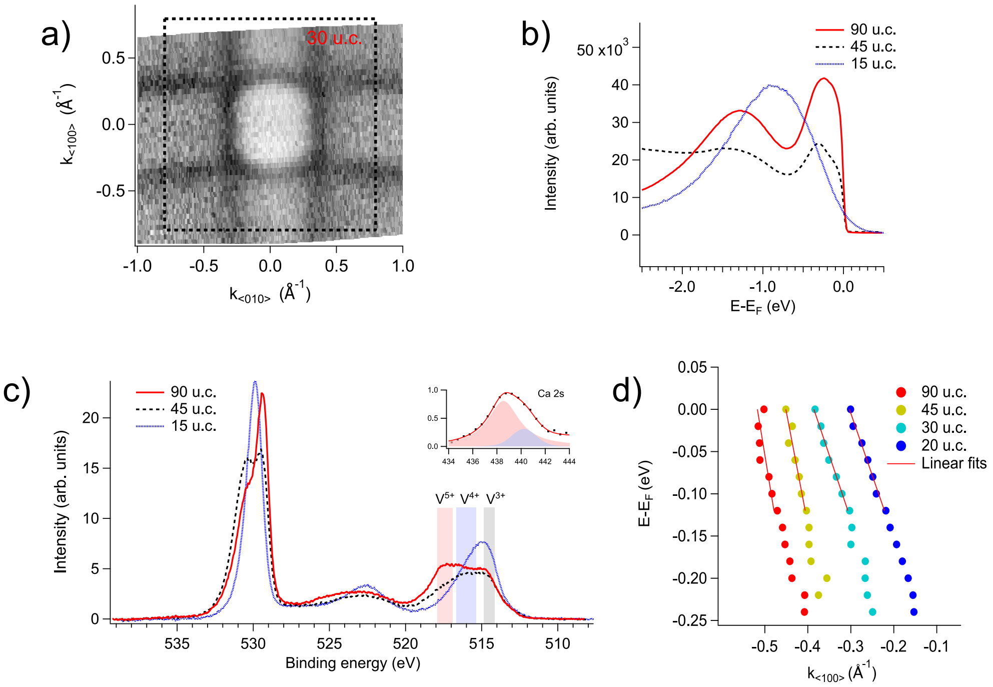

Figure 7.2 – a) Fermi surface on the k$_{<100>}$ - k$_{<010>}$ plane for the 30 u.c. sample. b) Integrated EDCs of the 90 u.c, 45 u.c. and 15 u.c. samples in the energy region of the Hubbard band and the quasiparticle peak near Fermi level. All measurements were taken with s-polarized photons at $h\nu$ = 82 eV. c) XPS BE measurements in the range of 505 eV to 540 eV for the 90 u.c., 45 u.c. and 15 u.c. samples. Inset shows Ca 2s peak used to calibrate binding energy of the insulating 15 u.c. sample. d) Extracted Lorentzian peaks and linear fits for the 90 u.c., 45 u.c., 30 u.c. and 25 u.c. sample dispersion at 82 eV. The peaks from different samples are shifted along k$_{<100>}$ for better visualization.

This chapter presents a detailed investigation of the electronic structure of thin films of CaVO$_3$, focusing on how film thickness influences its metal-insulator transition (MIT). CaVO$_3$ is a strongly correlated material where electron-electron interactions play a dominant role in determining its electronic properties. The study explores how the interactions of thin films of CaVO$_3$ grown on SrTiO$_3$ susbtrate, evolve as a function of film thickness and it's impact on the material's electronic structure.

Using high-resolution Angle-Resolved Photoemission Spectroscopy (ARPES), we examine CaVO$_3$ films of various thicknesses, ranging from bulk-like thickness (90 unit cells (u.c.)) to ultrathin films (down to 15 unit u.c.). The ARPES measurements reveal clear changes in Fermi level. As the film width decreases, from 90 u.c. down to 20 u.c., the in-plane Fermi surface expands in momentum space and becomes isotropic in k_x and k_y directions, which indicates a shrinking of in-plane lattice vectors to match the underlying substrate SrTiO$_3$ lattice. SrTiO$_3$ has an inplane lattice constant $a = 3.9$ Å compared to bulk

$CaVO_3$ lattice constant of $a = 3.77$ Å which results in a tensile epitaxial strain near the film substrate interface.

We also observe that as the film thickness decreases, the bandwidth of the conduction bands slightly narrows, indicating a reduction in bandwidth of the conduction band. The electronic structure of these films retains it's metallic characteristics, with a broad band near the Fermi surface. However, as the thickness is reduced from 20 u.c. to 15 u.c., there is a sudden emergence of a bandgap and a clear transition to an insulating state.

Core-level X-ray photoelectron spectroscopy (XPS) further supports the ARPES findings, providing evidence of changes in the chemical environment and electronic structure with decreasing thickness. There is a large shift in V oxidation state from V^{4+} to V^{3+} and a strong decrease in V-O covalency which seems to be driven by the increased octahedral tilt due to the epitaxial strain.

These findings corroborate existing experimental data and have broad implications for the design and control of electronic properties in oxide thin films, where the film thickness can be used as a tuning parameter to engineer material behavior.

7.5 . Quantum states of 2-D metal dihalide $FeCl_2$ on Au(111)

This study investigates the electronic structure of monolayer (ML) $FeCl_2$ grown on an Au(111) substrate. $FeCl_2$, a two-dimensional transition metal dihalide, exhibits inherent ferromagnetism and semiconducting properties, making it a promising candidate for spintronic applications.

Using low-temperature scanning tunnelling microscopy (LT-STM), we observed that the $FeCl_2$ ML forms a Cl-Fe-Cl trilayer with a slight lattice expansion to approximately 3.65 Å. Pseudo-periodic surface modulations suggest distortions in the underlying Fe and Cl layers.

Angle-resolved photoemission spectroscopy (ARPES) measurements revealed a flat valence band at around -2.7 eV, attributed to $FeCl_2$. Density functional theory (DFT) calculations—including Hubbard U and spin-orbit coupling (SOC)—confirm an insulating ferromagnetic ground state with a band gap of approximately 3 eV and a magnetic moment of $3.56\,\mu_B$ per Fe atom.

Scanning tunnelling spectroscopy (STS) indicated that the local density of states (LDOS) varies spatially across the ML. Bright spots in di/dV maps at 1.5 eV sample bias, showed multiple peaks near the Fermi level and an increase in LDOS at 1.22 eV, suggesting the onset of the conduction band and implying a smaller band gap than previously reported.

Quasiparticle interference (QPI) measurements uncovered two dispersing bands near the Fermi level, designated as $FeCl_2$ α and β bands, with band bottoms at -0.23 eV and -0.05 eV, respectively. These bands exhibit effective masses similar to the Au(111) surface state. The α band is interpreted as a shifted Au(111) surface state due to interface effects, while the origin of the β band may involve significant magnetic exchange interactions causing an energy splitting of about 200 meV.

Defect states may also influence the electronic properties. STS measurements at certain sites showed localized LDOS peaks around 0.3 eV. DFT simulations suggest that Fe vacancies could introduce states crossing the Fermi level, effectively doping the system and potentially leading to quantum well states.

In conclusion, $FeCl_2$ monolayers on Au(111) exhibit complex electronic interactions, including split surface bands possibly resulting from magnetic proximity effects. These findings open avenues for spintronic applications and further exploration of van der Waals heterostructures. Future work will aim to resolve the electronic structure near the Fermi level with greater precision and to clarify the role of defects in the ML's electronic properties.

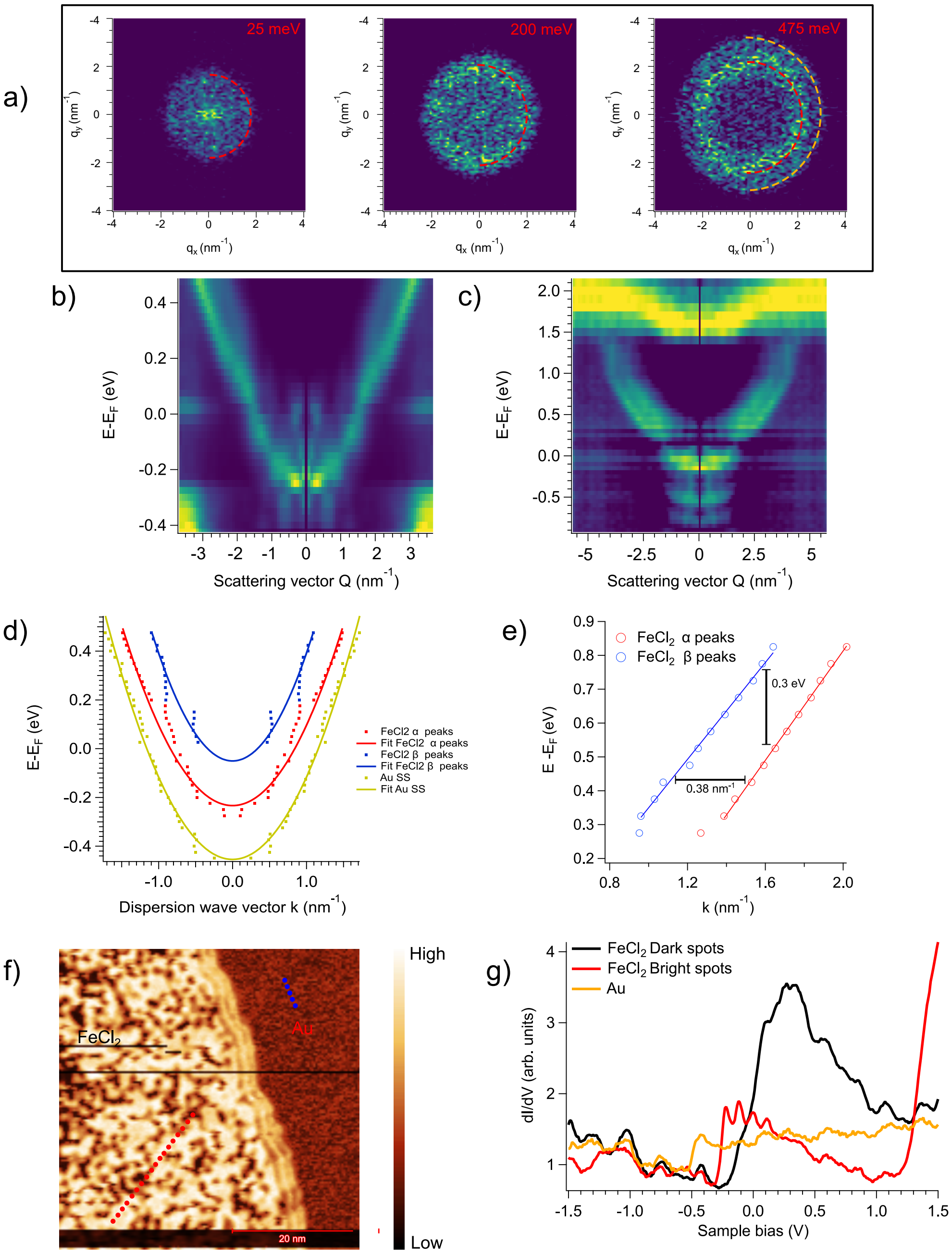

Figure 7.3 – a) QPI maps obtained by Fourier transform of the dI/dV maps at 25 meV, 200 meV and 475 meV for the isolated $FeCl_2$ ML. Red and yellow dashed lines are guides for the observed scattering vector **q**. Dispersion relation between **q** and energy E obtained by radial integration of QPI maps for b) $FeCl_2$ ML in a small energy range around E_F, c) $FeCl_2$ ML in a wider energy range. d) Extracted peaks for Au SS and $FeCl_2$ α and β bands from QPI dispersion. e) Peak positions in second derivative plot for α and β bands extracted from c and converted into k-space. f) dI/dV map of 1 ML $FeCl_2$ (V_b = 1.5 V, I = 50 pA). Red and blue dots represent spots for STS point spectra at the $FeCl_2$ layer and Au(111) surface respectively. g) Averaged STS profiles for bright, dark and Au spots from f.

8 - Synthèse en Français

8.1 . Introduction

Comprendre la relation entre la structure atomique, les propriétés fonctionnelles et la structure électronique des matériaux est un défi fondamental en physique de la matière condensée. De nombreux phénomènes parmi les plus intrigants en science des matériaux, tels que la supraconductivité, le magnétisme et les effets thermoélectriques, résultent d'interactions subtiles entre ces trois domaines. Malgré des progrès significatifs, les manières complexes dont l'agencement atomique et les corrélations électroniques donnent lieu à des comportements fonctionnels uniques restent une question ouverte, en particulier dans les matériaux fortement corrélés.

Cette thèse est motivée par la nécessité d'approfondir notre compréhension de la façon dont la structure atomique et électronique des matériaux gouverne leurs propriétés physiques. Le $CuRhO_2$ thermoélectrique métallique dopé au Mg, les films minces du métal corrélé $CaVO_3$ et l'isolant magnétique bidimensionnel de van der Waals $FeCl_2$ sur Au(111) ont été sélectionnés comme études de cas pour leur comportement électronique riche et leurs applications potentielles en thermoélectricité, dispositifs quantiques et spintronique. Chacun de ces matériaux présente des interactions complexes entre leurs configurations atomiques et leur structure électronique, fournissant des plateformes idéales pour explorer comment des modifications subtiles—telles que le dopage, la réduction de la dimensionalité ou les stimuli externes—peuvent modifier drastiquement leurs propriétés fonctionnelles.

8.2 . Contexte théorique et expérimental

Le cadre théorique de cette thèse est centré sur la compréhension de la formation des bandes électroniques et de l'impact des corrélations électroniques dans les matériaux fortement corrélés. En utilisant le modèle des liaisons fortes, nous décrivons comment les orbitales atomiques dans un réseau cristallin se recouvrent pour former des bandes d'énergie. L'introduction des interactions électron-électron via le modèle de Hubbard nous permet d'explorer comment ces corrélations peuvent conduire à des phénomènes tels que les transitions métal-isolant et les propriétés thermoélectriques améliorées. Pour modéliser avec précision ces effets dans les matériaux réels, la théorie de la fonctionnelle de la densité (DFT) est utilisée, avec l'extension DFT+U prenant en compte les fortes interactions électron-électron typiques des orbitales d et f localisées. Cette approche théorique permet une description plus précise de la structure électronique dans les systèmes corrélés, là où la théorie des bandes conventionnelle est insuffisante.

Expérimentalement, la spectroscopie de photoémission résolue en angle (ARPES) est utilisée pour sonder la structure des bandes électroniques et la surface de Fermi de ces matériaux, fournissant des mesures directes de la manière dont les corrélations et les modifications structurelles influencent leur comportement électronique. La microscopie à effet tunnel (STM) et la spectroscopie à effet tunnel (STS) sont utilisées pour obtenir une résolution à l'échelle atomique de la topographie de surface et de la densité locale d'états (LDOS), ce qui est essentiel pour étudier les états électroniques localisés, en particulier dans les systèmes de basse dimensionnalité comme les dihalogénures métalliques 2D. L'interférence de quasi-particules (QPI) complète ces techniques en capturant des informations résolues en moment sur les états de surface via la diffusion des quasi-particules, fournissant des informations supplémentaires sur la structure électronique au-dessus du niveau de Fermi qui ne sont pas accessibles par ARPES seule.

8.3 . Thermoélectricité dans $CuRhO_2$ dopé au Mg

Dans ce chapitre, nous étudions la structure électronique du $CuRhO_2$ dopé au Mg, un oxyde de type delafossite. $CuRhO_2$ est un matériau isolant avec un coefficient Seebeck S élevé. Le dopage du matériau avec du Mg le rend métallique tout en préservant la valeur élevée de S. Ce comportement est inattendu car les métaux ont tendance à avoir un faible coefficient thermoélectrique en raison des mobilités égales des électrons et des trous près du niveau de Fermi. La performance thermoélectrique d'un matériau est caractérisée par le facteur de mérite thermoélectrique $ZT = S^2\sigma T/\kappa$, où S est le coefficient Seebeck, σ est la conductivité électrique, T est la température, et κ est la conductivité thermique. Un coefficient Seebeck élevé associé à une bonne conductivité électrique et une faible conductivité thermique sont donc essentiels. Le $CuRhO_2$ dopé, qui présente un comportement métallique avec un coefficient Seebeck élevé, est donc un matériau candidat parfait pour des applications potentielles dans les dispositifs thermoélectriques.

La structure de bande de type "pudding-mold", avec une dispersion plate juste au-dessus (en dessous) du niveau de Fermi et une bande fortement dispersive juste en dessous (au-dessus) du niveau de Fermi, joue un rôle central dans la performance thermoélectrique observée de $CuRhO_2$, comme suggéré par les calculs théoriques. En utilisant la ARPES, nous cartographions la structure de bande et observons cette structure de bande de type "pudding-mold" dans le $CuRhO_2$ métallique dopé à 10% de Mg. Des calculs de la théorie de la fonctionnelle de la densité (DFT) du $CuRhO_2$ isolant ont été effectués. Avec un petit décalage rigide de -0,06 du niveau de Fermi, les bandes calculées montrent une excellente correspondance avec la structure de bande ARPES de l'échantillon dopé. Ces bandes décalées ont ensuite été utilisées pour calculer le coefficient Seebeck thermoélectrique. Les valeurs calculées du coefficient Seebeck S $\sim 256\mu$V/K pour les échantillons dopés à 1000 K sont en accord étroit avec les expériences.

La combinaison des perspectives expérimentales et théoriques conduit à une compréhension complète de la façon dont le dopage au Mg ajuste la structure électronique du $\mathrm{CuRhO_2}$ pour améliorer sa performance thermoélectrique. Les résultats de ce chapitre ont des implications plus larges pour la conception et l'exploration d'autres matériaux thermoélectriques à base d'oxydes avec cette bande de type "pudding-mold" pour des applications thermoélectriques. Voir la fig. 8.1 pour un résumé graphique.

8.4 . Transition métal-isolant dans les films minces de $\mathrm{CaVO_3}$

Ce chapitre présente une étude détaillée de la structure électronique des films minces de $\mathrm{CaVO_3}$, en se concentrant sur la façon dont l'épaisseur du film influence sa transition métal-isolant (MIT). $\mathrm{CaVO_3}$ est un matériau fortement corrélé où les interactions électron-électron jouent un rôle dominant dans la détermination de ses propriétés électroniques. L'étude explore comment les interactions des films minces de $\mathrm{CaVO_3}$ cultivés sur un substrat $\mathrm{SrTiO_3}$ évoluent en fonction de l'épaisseur du film et de son impact sur la structure électronique du matériau.

En utilisant la ARPES, nous examinons des films de $\mathrm{CaVO_3}$ de différentes épaisseurs, allant de l'épaisseur semblable au massif (90 unités de cellules (u.c.)) à des films ultraminces (jusqu'à 15 u.c.). Les mesures ARPES révèlent des changements clairs au niveau de Fermi. À mesure que l'épaisseur du film diminue de 90 u.c. à 20 u.c., la surface de Fermi dans le plan s'étend dans l'espace des moments et devient isotrope dans les directions k_x et k_y, ce qui indique un rétrécissement des vecteurs de réseau dans le plan pour correspondre au réseau du substrat sous-jacent $\mathrm{SrTiO_3}$. $\mathrm{SrTiO_3}$ a une constante de réseau dans le plan $a = 3,9$ Å comparée à la constante de réseau du $\mathrm{CaVO_3}$ massif de $a = 3,77$ Å, ce qui entraîne une contrainte épitaxiale en traction près de l'interface film-substrat.

Nous observons également qu'à mesure que l'épaisseur du film diminue, la largeur de bande des bandes de conduction se rétrécit légèrement, indiquant une réduction de la largeur de bande de la bande de conduction. La structure électronique de ces films conserve ses caractéristiques métalliques, avec une large bande près de la surface de Fermi. Cependant, lorsque l'épaisseur est réduite de 20 u.c. à 15 u.c., il y a une apparition soudaine d'un gap de bande et une transition claire vers un état isolant.

La spectroscopie de photoélectrons à rayons X (XPS) des niveaux de cœur soutient en outre les résultats de l'ARPES, fournissant des preuves de changements dans l'environnement chimique et la structure électronique avec l'épaisseur décroissante. Il y a un grand changement dans l'état d'oxydation du V de V^{4+} à V^{3+} et une forte diminution de la covalence V-O qui semble être provoquée par l'augmentation de l'inclinaison octaédrique due à la contrainte épitaxiale.

Ces résultats corroborent les données expérimentales existantes et ont de larges implications pour la conception et le contrôle des propriétés électroniques dans les films minces d'oxydes, où l'épaisseur du film peut être utilisée comme paramètre de réglage pour concevoir le comportement des matériaux. Voir la fig. 8.2 pour un résumé graphique.

8.5 . États quantiques du dihalogénure métallique 2D FeCl$_2$ sur Au(111)

Cette étude examine la structure électronique de la monocouche (ML) FeCl$_2$ cultivée sur un substrat Au(111). FeCl$_2$, un dihalogénure de métal de transition bidimensionnel, présente un ferromagnétisme inhérent et des propriétés semi-conductrices, ce qui en fait un candidat prometteur pour les applications spintroniques.

En utilisant la microscopie à effet tunnel à basse température (LT-STM), nous avons observé que la monocouche FeCl$_2$ forme une trilame Cl-Fe-Cl avec une légère expansion du réseau à environ 3,65 Å. Des modulations de surface pseudo-périodiques suggèrent des distorsions dans les couches sous-jacentes de Fe et de Cl.

Les mesures de ARPES ont révélé une bande de valence plate autour de 2,7 eV attribuée au FeCl$_2$. Les calculs de la théorie de la fonctionnelle de la densité (DFT)—y compris le Hubbard U et le couplage spin-orbite (SOC)—confirment un état fondamental ferromagnétique isolant avec un gap de bande d'environ 3 eV et un moment magnétique de 3,56 μB par atome de Fe.

La spectroscopie à effet tunnel (STS) a indiqué que la densité locale d'états (LDOS) varie spatialement à travers la monocouche. Les zones claires des cartes dI/dV à un biais d'échantillon de 1,5 eV ont montré plusieurs pics proches du niveau de Fermi et une augmentation du LDOS à 1,22 eV, suggérant le début de la bande de conduction et impliquant un gap de bande plus petit que celui précédemment rapporté.

Les mesures d'interférence de quasi-particules (QPI) ont mis en évidence deux bandes dispersives près du niveau de Fermi, désignées comme les bandes α et β du FeCl$_2$, avec des fonds de bande à -0,23 eV -0,05eV, respectivement. Ces bandes présentent des masses effectives similaires à l'état de surface Au(111). La bande α est interprétée comme un état de surface Au(111) décalé en raison des effets d'interface, tandis que l'origine de la bande β peut impliquer des interactions d'échange magnétiques significatives causant un dédoublement énergétique d'environ 200 meV.

Les états de défaut peuvent également influencer les propriétés électroniques. Les mesures STS à certains sites ont montré des pics LDOS localisés autour de 0,3eV. Les simulations DFT suggèrent que les lacunes de Fe pourraient introduire des états traversant le niveau de Fermi, dopant effectivement le système et conduisant potentiellement à des états de puits quantiques.

En conclusion, les monocouches de $FeCl_2$ sur Au(111) présentent des interactions électroniques complexes, y compris des bandes de surface dédoublées résultant possiblement d'effets de proximité magnétique. Ces résultats ouvrent des voies pour des applications spintroniques et une exploration plus approfondie des hétérostructures de van der Waals. Les travaux futurs viseront à résoudre la structure électronique près du niveau de Fermi avec une plus grande précision et à clarifier le rôle des défauts dans les propriétés électroniques de la monocouche. Voir la fig. 8.3 pour un résumé graphique.

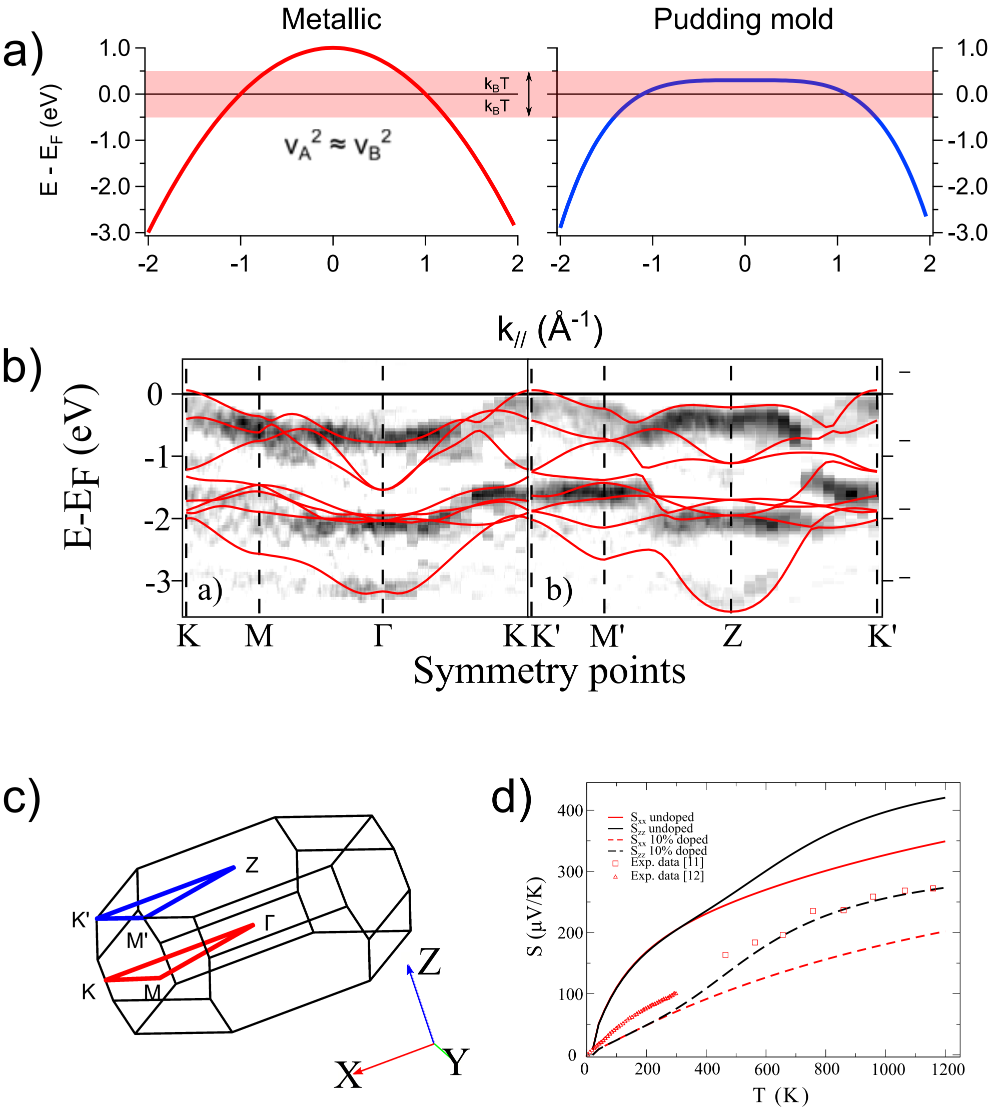

Figure 8.1 – a) Schéma pour une bande métallique et de type pudding mold. v$_A$ et v$_B$ représentent les vitesses des bandes au-dessus et en dessous du niveau de Fermi dans la région rouge mise en évidence de largeur 2kBT. b) Coupe de bande dans le plan à 542 eV ($k_z = \Gamma$) et à 590 eV d'énergie photonique ($k_z = Z$), superposée avec les bandes calculées en rouge. c) Zone de Brillouin primitive de CuRhO2. Les points de haute symétrie et le chemin les reliant sont indiqués. d) Les composantes S$_{xx}$ et S$_{zz}$ du coefficient Seebeck calculé en fonction de la température pour l'échantillon non dopé et l'échantillon dopé à 10%. Les données expérimentales de [69] et [68] sont comparées aux calculs du coefficient Seebeck dopé.

)

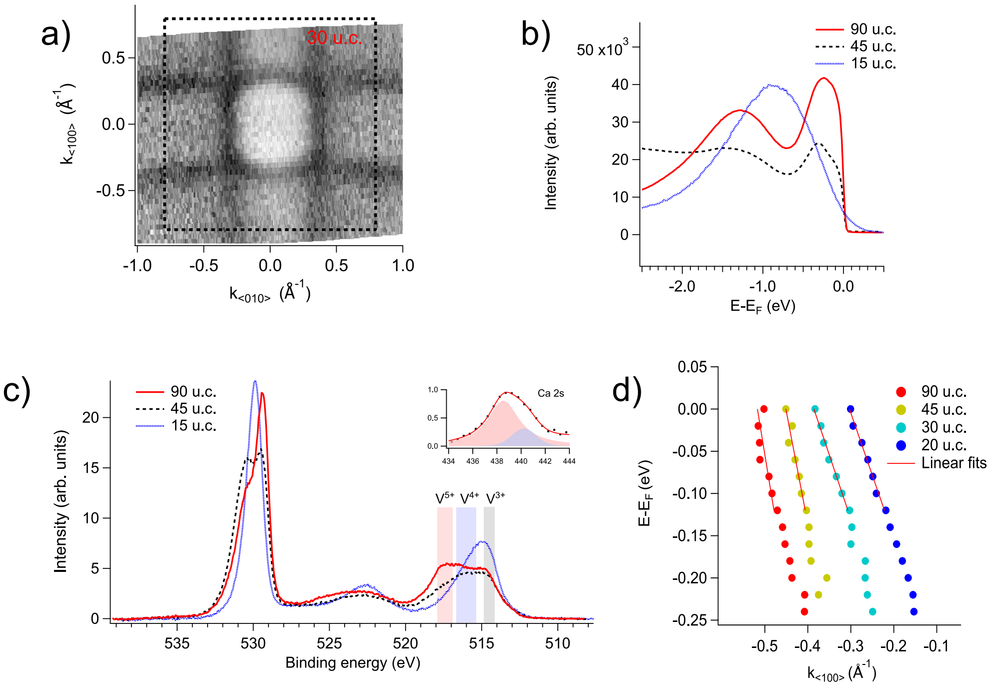

Figure 8.2 – a) Surface de Fermi dans le plan k$_{\langle 100\rangle}$ - k$_{\langle 010\rangle}$ pour l'échantillon de 30 u.c. b) EDCs intégrées des échantillons de 90 u.c., 45 u.c. et 15 u.c. dans la région d'énergie de la bande de Hubbard et du pic de quasi-particule près du niveau de Fermi. Toutes les mesures ont été prises avec des photons s-polarisés à $h\nu$ = 82 eV. c) Mesures XPS de l'énergie de liaison dans la gamme de 505 eV à 540 eV pour les échantillons de 90 u.c., 45 u.c. et 15 u.c. L'encart montre le pic Ca 2s utilisé pour calibrer l'énergie de liaison de l'échantillon isolant de 15 u.c. d) Pics lorentziens extraits et ajustements linéaires pour la dispersion des échantillons de 90 u.c., 45 u.c., 30 u.c. et 25 u.c. à 82 eV. Les pics des différents échantillons sont décalés le long de k$_{\langle 100\rangle}$ pour une meilleure visualisation.

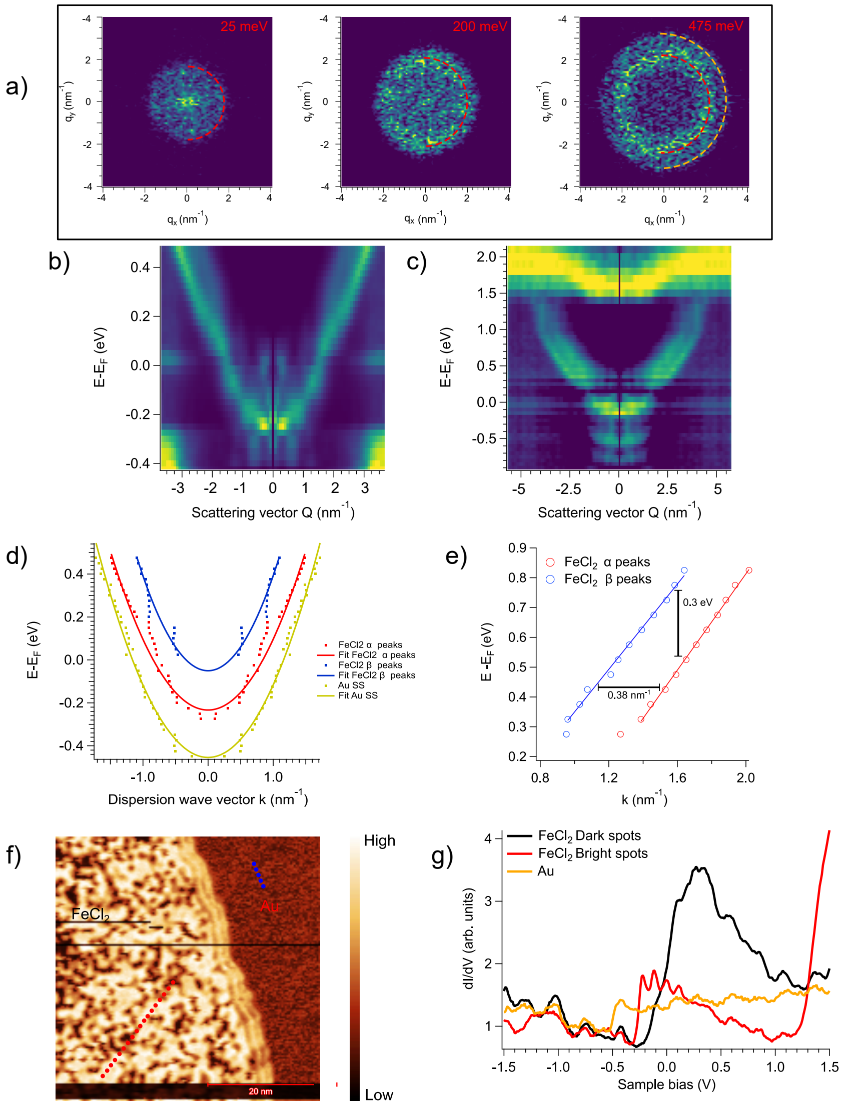

Figure 8.3 – a) Cartes QPI obtenues par transformée de Fourier des cartes dI/dV à 25 meV, 200 meV et 475 meV pour la monocouche isolée de FeCl$_2$. Les lignes pointillées rouges et jaunes sont des guides pour le vecteur de diffusion **q** observé. Relation de dispersion entre **q** et l'énergie E obtenue par intégration radiale des cartes QPI pour b) la monocouche de FeCl$_2$ dans une petite plage d'énergie autour de E$_F$, c) la monocouche de FeCl$_2$ dans une plage d'énergie plus large. d) Pics extraits pour l'état de surface Au SS et les bandes α et β du FeCl$_2$ à partir de la dispersion QPI. e) Positions des pics dans le graphique de la seconde dérivée pour les bandes α et β extraites de c et converties en espace k. f) Carte dI/dV d'une monocouche de FeCl$_2$ (V$_b$ = 1,5 V, I = 50 pA). Les points rouges et bleus représentent les emplacements pour les spectres ponctuels STS à la couche FeCl$_2$ et à la surface Au(111) respectivement. g) Profils STS moyennés pour les zones claires, sombres et Au de f.

9 - Resumen en español

9.1 . Introducción

Comprender la relación entre la estructura atómica, las propiedades funcionales y la estructura electrónica de los materiales es un desafío fundamental en la física de la materia condensada. Muchos de los fenómenos más intrigantes en la ciencia de los materiales, como la superconductividad, el magnetismo y los efectos termoeléctricos, surgen de interacciones sutiles entre estos tres dominios. A pesar de los avances significativos, las complejas formas en las que la disposición atómica y las correlaciones electrónicas dan lugar a comportamientos funcionales únicos siguen siendo una cuestión abierta, especialmente en los materiales fuertemente correlacionados.

Esta tesis está motivada por la necesidad de profundizar nuestra comprensión de cómo la estructura atómica y electrónica de los materiales gobierna sus propiedades físicas. $CuRhO_2$ dopado con Mg para aplicaciones termoeléctricas, películas delgadas del metal correlacionado $CaVO_3$, y el aislante magnético bidimensional van der Waals $FeCl_2$ en Au(111) han sido seleccionados como estudios de caso por su rico comportamiento electrónico y su potencial en aplicaciones termoeléctricas, dispositivos cuánticos y espintrónica. Cada uno de estos materiales presenta interacciones complejas entre sus configuraciones atómicas y estructura electrónica, proporcionando plataformas ideales para explorar cómo modificaciones sutiles—como el dopaje, la reducción de la dimensionalidad o los estímulos externos—pueden alterar drásticamente sus propiedades funcionales.

9.2 . Fundamentos teóricos y experimentales

El marco teórico de esta tesis se centra en la comprensión de la formación de bandas electrónicas y el impacto de las correlaciones electrónicas en materiales fuertemente correlacionados. Utilizando el modelo de enlaces fuertes, describimos cómo los orbitales atómicos en una red cristalina se superponen para formar bandas de energía. La introducción de interacciones electrón-electrón a través del modelo de Hubbard nos permite explorar cómo estas correlaciones pueden llevar a fenómenos como transiciones metal-aislante y propiedades termoeléctricas mejoradas. Para modelar con precisión estos efectos en materiales reales, se emplea la Teoría del Funcional de la Densidad (DFT), con la extensión DFT+U para tener en cuenta las fuertes interacciones electrón-electrón típicas de los orbitales localizados d y f. Este enfoque teórico permite una descripción más precisa de la estructura electrónica en sistemas correlacionados, donde la teoría de bandas convencional resulta insuficiente.

Experimentalmente, la espectroscopía de fotoemisión resuelta en ángulo (ARPES) se utiliza para sondear la estructura de bandas electrónicas y la superficie de Fermi de estos materiales, proporcionando mediciones directas de cómo las correlaciones y modificaciones estructurales influyen en su comportamiento electrónico. La microscopía de efecto túnel (STM) y la espectroscopía de efecto túnel (STS) se utilizan para obtener una resolución a escala atómica de la topografía de la superficie y la densidad local de estados (LDOS), lo cual es esencial para estudiar los estados electrónicos localizados, especialmente en sistemas de baja dimensionalidad como los dihaluros metálicos 2D. La interferencia de cuasi-partículas (QPI) complementa estas técnicas al capturar información resuelta en momento sobre los estados de superficie a través de la dispersión de cuasi-partículas, proporcionando información adicional sobre la estructura electrónica por encima del nivel de Fermi que no es accesible únicamente a través de ARPES.

9.3 . Termoelectricidad en CuRhO$_2$ dopado con Mg

En este capítulo, investigamos la estructura electrónica del CuRhO$_2$ dopado con Mg, un óxido de tipo delafosita. CuRhO$_2$ es un material aislante con un coeficiente Seebeck S alto. El dopaje del material con Mg lo convierte en metálico mientras sigue conservando el valor alto de S. Este comportamiento es inesperado, ya que los metales tienden a tener un coeficiente termoeléctrico bajo debido a las movilidades iguales de electrones y huecos cerca del nivel de Fermi. El rendimiento termoeléctrico de un material se caracteriza por la figura de mérito termoeléctrica $ZT = S^2\sigma T/\kappa$, donde S es el coeficiente Seebeck, σ es la conductividad eléctrica, T es la temperatura, y κ es la conductividad térmica. Un coeficiente Seebeck alto junto con una buena conductividad eléctrica y una baja conductividad térmica son, por lo tanto, críticos. El CuRhO$_2$ dopado que muestra un comportamiento metálico junto con un coeficiente Seebeck alto es un material candidato perfecto para aplicaciones potenciales en dispositivos termoeléctricos.

La estructura de banda de tipo "pudding-mold", con una dispersión plana justo por encima (debajo) del nivel de Fermi y una banda altamente dispersiva justo debajo (por encima) del nivel de Fermi, juega un papel central en el rendimiento termoeléctrico observado de CuRhO$_2$, como sugieren los cálculos teóricos. Utilizando la ARPES, cartografiamos la estructura de bandas y observamos esta estructura de bandas de tipo "pudding-mold" en CuRhO$_2$ metálico dopado con 10$\%$ de Mg. Se realizaron cálculos de la Teoría del Funcional de la Densidad (DFT) del CuRhO$_2$ aislante. Con un pequeño desplazamiento rígido de -0.06 del nivel de Fermi, las bandas calculadas muestran una excelente coincidencia con la estructura de bandas ARPES de la muestra do-

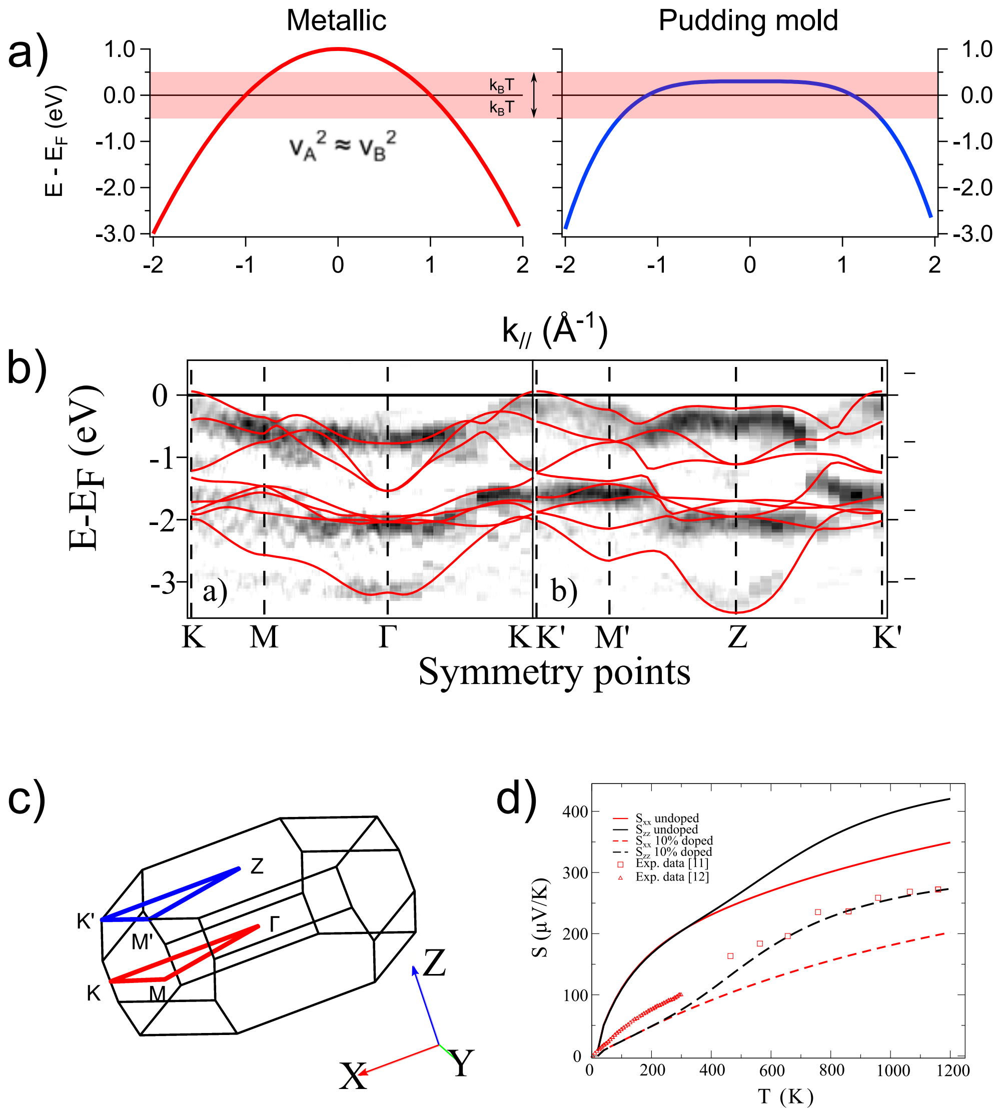

Figure 9.1 – a) Esquema para una banda metálica y de tipo "pudding mold". v$_A$ y v$_B$ representan las velocidades de banda por encima y por debajo del nivel de Fermi en la región roja resaltada de ancho 2k$_B$T. b) Corte de la banda en el plano a 542 eV ($k_z = \Gamma$) y a 590 eV de energía de fotón ($k_z = Z$), superpuesto con las bandas calculadas en rojo. c) Zona de Brillouin primitiva de CuRhO$_2$. Se indican los puntos de alta simetría y el camino que los conecta. d) Las componentes S$_{xx}$ y S$_{zz}$ del coeficiente Seebeck calculado en función del nivel de temperatura para la muestra no dopada y la muestra dopada al 10%. Los datos experimentales de [69] y [68] se comparan con los cálculos del coeficiente Seebeck dopado.

pada. Estas bandas desplazadas se utilizaron luego para calcular el coeficiente termoeléctrico de Seebeck. Los valores calculados del coeficiente Seebeck S

$\sim 256\mu$V/K para las muestras dopadas a 1000 K están en estrecho acuerdo con los experimentos.

La combinación de conocimientos experimentales y teóricos lleva a una comprensión integral de cómo el dopaje con Mg ajusta la estructura electrónica de CuRhO$_2$ para mejorar su rendimiento termoeléctrico. Los hallazgos de este capítulo tienen implicaciones más amplias para el diseño y la exploración de otros materiales termoeléctricos basados en óxidos con esta banda de tipo "pudding-mold" para aplicaciones termoeléctricas. Consulte la fig. 9.1 para ver un resumen gráfico.

9.4 . Transición metal-aislante en películas delgadas de CaVO$_3$

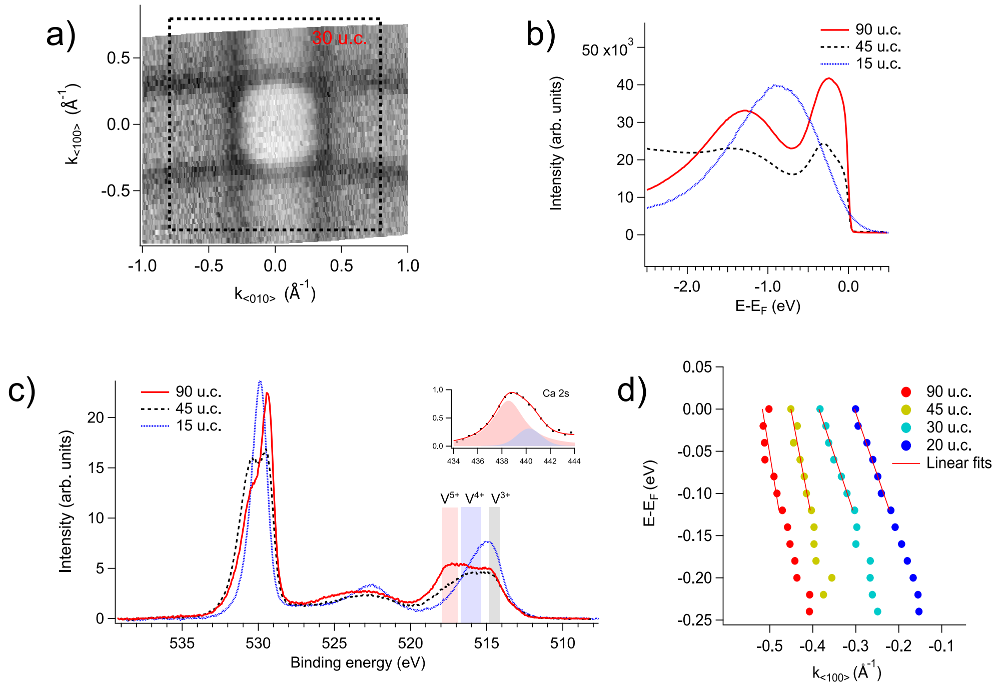

Figure 9.2 – a) Superficie de Fermi en el plano k$_{<100>}$ - k$_{<010>}$ para la muestra de 30 u.c. b) EDCs integrados de las muestras de 90 u.c., 45 u.c. y 15 u.c. en la región de energía de la banda de Hubbard y el pico de cuasipartículas cerca del nivel de Fermi. Todas las mediciones se realizaron con fotones polarizados en s a $h\nu$ = 82 eV. c) Mediciones XPS BE en el rango de 505 eV a 540 eV para las muestras de 90 u.c., 45 u.c. y 15 u.c. El recuadro muestra el pico Ca 2s utilizado para calibrar la energía de enlace de la muestra aislante de 15 u.c. d) Picos lorentzianos extraídos y ajustes lineales para la dispersión de las muestras de 90 u.c., 45 u.c., 30 u.c. y 25 u.c. a 82 eV. Los picos de diferentes muestras se desplazan a lo largo de k$_{<100>}$ para una mejor visualización.

Este capítulo presenta una investigación detallada de la estructura electrónica de películas delgadas de $CaVO_3$, centrándose en cómo el grosor de la película influye en su transición metal-aislante (MIT). $CaVO_3$ es un material fuertemente correlacionado donde las interacciones electrón-electrón juegan un papel dominante en la determinación de sus propiedades electrónicas. El estudio explora cómo las interacciones de las películas delgadas de $CaVO_3$ crecidas sobre sustratos de $SrTiO_3$ evolucionan en función del grosor de la película y su impacto en la estructura electrónica del material.

Utilizando la ARPES, examinamos películas de $CaVO_3$ de varios grosores, que van desde el grosor de tipo masivo (90 celdas unidad (u.c.)) hasta películas ultradelgadas (hasta 15 u.c.). Las mediciones de ARPES revelan cambios claros en el nivel de Fermi. A medida que el grosor de la película disminuye de 90 u.c. a 20 u.c., la superficie de Fermi en el plano se expande en el espacio de momentos y se vuelve isotrópica en las direcciones k_x y k_y, lo que indica una contracción de los vectores de red en el plano para coincidir con la red del sustrato subyacente $SrTiO_3$. $SrTiO_3$ tiene una constante de red en el plano $a = 3.9$ Å en comparación con la constante de red de $CaVO_3$ masivo de $a = 3.77$ Å , lo que resulta en una tensión epitaxial de tracción cerca de la interfaz película-sustrato.

También observamos que a medida que el grosor de la película disminuye, el ancho de banda de las bandas de conducción se reduce ligeramente, lo que indica una reducción en el ancho de banda de la banda de conducción. La estructura electrónica de estas películas conserva sus características metálicas, con una banda amplia cerca de la superficie de Fermi. Sin embargo, cuando el grosor se reduce de 20 u.c. a 15 u.c., se produce una aparición repentina de una brecha de banda y una transición clara a un estado aislante.

La espectroscopía de fotoelectrones de rayos X (XPS) a nivel de núcleo respalda además los hallazgos de ARPES, proporcionando evidencia de cambios en el entorno químico y la estructura electrónica con la disminución del grosor. Hay un gran cambio en el estado de oxidación del V de V^{4+} a V^{3+} y una fuerte disminución en la covalencia V-O, que parece ser impulsada por la mayor inclinación octaédrica debido a la tensión epitaxial.

Estos hallazgos corroboran los datos experimentales existentes y tienen amplias implicaciones para el diseño y control de las propiedades electrónicas en películas delgadas de óxidos, donde el grosor de la película puede utilizarse como un parámetro de ajuste para diseñar el comportamiento del material. Consulte la fig. 9.2 para ver un resumen gráfico.

9.5 . Estados cuánticos del dihaluro metálico 2D $FeCl_2$ en Au(111)

Este estudio investiga la estructura electrónica de una monocapa (ML) de $FeCl_2$ crecida sobre un sustrato Au(111). $FeCl_2$, un dihaluro de metal de transición bidimensional, exhibe ferromagnetismo inherente y propiedades semiconductoras, lo que lo convierte en un candidato prometedor para aplicaciones espintrónicas.

Utilizando microscopía de efecto túnel a baja temperatura (LT-STM), observamos que la monocapa de $FeCl_2$ forma una capa triple Cl-Fe-Cl con una ligera expansión de la red a aproximadamente 3.65 Å. Las modulaciones superficiales pseudoperiódicas sugieren distorsiones en las capas subyacentes de Fe y Cl.

Las mediciones de ARPES revelaron una banda de valencia plana alrededor de -2.7 eV, atribuida a $FeCl_2$. Los cálculos de la teoría del funcional de la densidad (DFT), incluyendo el Hubbard U y el acoplamiento espín-órbita (SOC), confirman un estado fundamental ferromagnético aislante con una brecha de banda de aproximadamente 3 eV y un momento magnético de $3.56\,\mu_B$ por átomo de Fe.

La espectroscopía de efecto túnel (STS) indicó que la densidad local de estados (LDOS) varía espacialmente a través de la monocapa. Las áreas brillantes de los mapas dI/dV con un sesgo de muestra de 1,5 eV mostraron varios picos cerca del nivel de Fermi y un aumento en LDOS a 1,22 eV, lo que sugiere el inicio de la banda de conducción e implica una brecha de banda más pequeña que la reportada anteriormente.

Las mediciones de interferencia de cuasi-partículas (QPI) descubrieron dos bandas dispersivas cerca del nivel de Fermi, designadas como las bandas α y β de $FeCl_2$, con los fondos de banda a -0.23 eV y -0.05 eV, respectivamente. Estas bandas muestran masas efectivas similares al estado superficial de Au(111). Se interpreta que la banda α es un estado superficial de Au(111) desplazado debido a efectos de interfaz, mientras que el origen de la banda β puede implicar interacciones de intercambio magnético significativas que causan una división energética de aproximadamente 200 meV.

Los estados de defecto también pueden influir en las propiedades electrónicas. Las mediciones de STS en ciertos sitios mostraron picos LDOS localizados alrededor de 0.3 eV. Las simulaciones DFT sugieren que las vacantes de Fe podrían introducir estados que cruzan el nivel de Fermi, dopando efectivamente el sistema y conduciendo potencialmente a estados de pozo cuántico.

En conclusión, las monocapas de $FeCl_2$ en Au(111) muestran interacciones electrónicas complejas, incluidas bandas superficiales divididas posiblemente resultantes de efectos de proximidad magnética. Estos hallazgos abren caminos para aplicaciones espintrónicas y una mayor exploración de las heteroestructuras de van der Waals. El trabajo futuro buscará resolver la estructura electrónica cerca del nivel de Fermi con mayor precisión y aclarar el papel de los defectos en las propiedades electrónicas de la monocapa. Consulte la fig. 9.3 para ver un resumen gráfico.

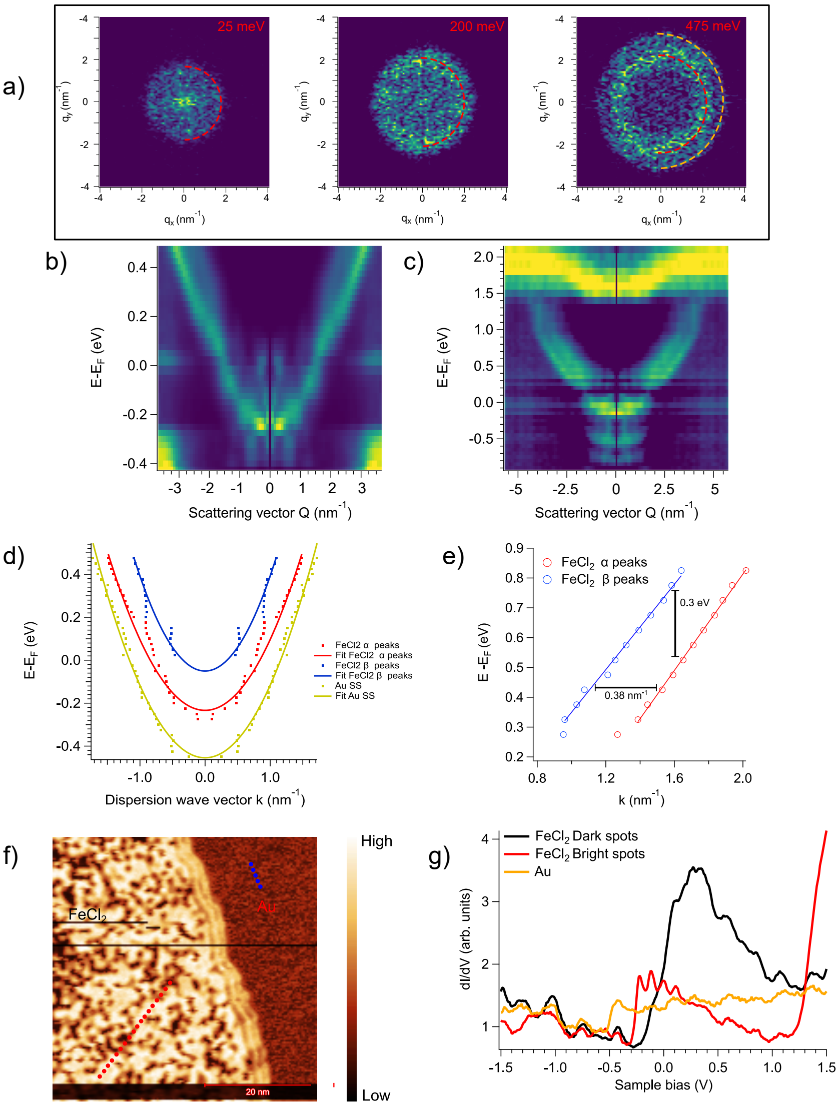

Figure 9.3 – a) Mapas de QPI obtenidos por transformada de Fourier de los mapas de dI/dV a 25 meV, 200 meV y 475 meV para la monocapa aislada de $FeCl_2$. Las líneas discontinuas rojas y amarillas son guías para el vector de dispersión q observado. Relación de dispersión entre q y la energía E obtenida mediante la integración radial de los mapas QPI para b) la monocapa de $FeCl_2$ en un rango pequeño de energía alrededor de E_F, c) la monocapa de $FeCl_2$ en un rango de energía más amplio. d) Picos extraídos para el estado superficial de Au SS y las bandas α y β de $FeCl_2$ a partir de la dispersión QPI. e) Posiciones de los picos en el gráfico de segunda derivada para las bandas α y β extraídas de c y convertidas en el espacio k. f) Mapa de dI/dV de una monocapa de $FeCl_2$ (V_b = 1.5 V, I = 50 pA). Los puntos rojos y azules representan los puntos de espectros STS en la capa $FeCl_2$ y en la superficie de Au(111), respectivamente. g) Perfiles STS promediados para las zonas claras, oscuras y de Au de f.